TÉCNICO LISBOA

Optimization and Evaluation of Solar Powered Electric Rickshaw

José Carlos Furtado da Veiga

Thesis to obtain the Master of Science Degree in

Engineering Physics

Supervisor(s): Prof. Dr. Horácio João Matos Fernandes
Prof. Dr. Paulo José da Costa Branco

Examination Committee

Chairperson: Prof. João Alberto dos Santos Mendanha Dias
Supervisor: Prof. Horácio João Matos Fernandes
Member of the Committee: Prof. João Filipe Pereira Fernandes

October 2022

I declare that this document is an original work of my own authorship and that it fulfills all the requirements of the Code of Conduct and Good Practices of the Universidade de Lisboa

To my parents, especially my late father.

Agradecimentos

Durante a realização desta tese, contei com o apoio de muitas pessoas e instituições. Manifesto, assim, a minha profunda gratidão a estas pessoas que, directa ou indirectamente, contribuíram para a concretização deste trabalho e consequentemente a realização de mais um sonho.

Ao professor Doutor Horácio Fernandes e professor Doutor Paulo Branco, meus orientadores, que acompanharam durante toda a realização desta tese que estiveram sempre disponíveis para esclarecer dúvidas e discutir este trabalho e dar sugestões para o melhoramento do mesmo.

À Fundação para Ciência e Tecnologia (FCT) pelo financiamento deste projeto de investigação com referência - TEDO-1018P.05430.1.

Seguidamente, gostaria de agradecer ao *ColorTrip* pela disponibilização do *Tuk-Tuk* e do material usado para a aquisição de dados, em especial um obrigado ao José Pedro por toda ajuda na parte de aquisição das rotas. Um agradecimento especial ao colega, João Ornelas pelo companheirismo e entre ajuda demonstrada ao longo da realização desta tese e ao David Neto pela ajuda em análise de dados. Da mesma forma, agradeço a todo o pessoal do Laboratório de Energia e Sistemas pela disponibilização do material usado para a montagem dos painéis solares no *Tuk-Tuk*.

Em seguida, gostaria de agradecer a equipa do Núcleo de Desenvolvimento Académico (NDA-GATu) pelo acompanhamento deste o primeiro dia que entrei nesta universidade e pelo suporte que foram importantes para cada ano melhorar o meu rendimento académico.

Por último, mas não menos importante agradeço a minha família pelo amor incondicional durante toda a vida, por disponibilizar as ferramentas certas para me tornar a pessoa que sou hoje. Um agradecimento a todos os meus amigos e colegas que tive a oportunidade de conhecer ao longo desta trajetória de vida que me ajudaram a trilhar o caminho que escolhi.

A todos vocês um muito Obrigado,

José Veiga.

Resumo

Os veículos elétricos são considerados uma opção mais viavél no combate da emissão dos gases de efeito de estufa no sector de transporte. No entanto, um dos problemas que impedem a adoção global dos veículos elétricos é a autonomia limitada, o que leva ao fenómeno de ansiedade de alcance. A produção fotovoltaica integrada em veículos elétricos é uma possível alternativa para este problema. Ao incorporar a tecnologia fotovoltaica no teto do veículo, as baterias do mesmo pode ser carregado durante a condução ou mesmo quando o veículo está em estacionamento. Por outro lado, o emprego desta tecnologia permite subdimensionar as baterias, originando numa poupança directa no investimento capital do veículo e nos custos de operação.

O foco desta tese é, pois, otimizar o processo de carregamento de um riquexó usando os modulos fotovoltaicos a bordo com base num histórico diário de percursos, quantificando a viabilidade tecno-económica quanto a existência de mercado para estes veículos. Com o sistema proposto, foi possivel observar, num dia típico ensolarado em meia estação, um aporte em média dum suplemento de 35% da energia elétrica consumida pelo veículo. A análise econômica do sistema proposto previu um ROI de 185% ao longo da vida útil do veículo de 6 anos.

Note-se que, devido ao cariz sazonal do veículo em que é esperado um maior consumo em dias de sol devido às suas características turísticas, estas poupanças podem ser levadas praticamente ao limite duma redução similar á capacidade energética das baterias.

Palavras-chave: sistemas fotovoltaicos, veículo elétrico, mobilidade urbana, energia solar, carregamento elétrico.

Abstract

Electric vehicles are considered a viable solution to combat greenhouse gas emissions in the transport sector. However, one of the problems holding back the global adoption of electric vehicles is the limited range, leading to range anxiety. Integrated photovoltaic production in electric vehicles is a possible alternative to this problem. By incorporating photovoltaic technology into the vehicle's roof, the vehicle's battery storage system can be charged while driving or even when the vehicle is parked. On the other hand, this technology makes it possible to undersize batteries, resulting in direct savings in the capital investment in the vehicle and operating costs.

The main focus of the present thesis is to optimize the process of charging electric rickshaw batteries with onboard photovoltaics modules based on the daily history of journeys, quantifying the techno-economic feasibility regarding the existence of a market for these vehicles. With the proposed system, it was possible to observe, on a typical sunny day in mid-season, an average supply of a supplement of 35% of the energy consumed by the vehicle. Furthermore, the economic analysis predicted an ROI of 185% throughout the vehicle's lifetime of 6 years.

It should be noted that, due to the seasonal nature of the vehicle, where greater consumption is expected on sunny days due to its tourist characteristics, these savings can be taken practically to the limit of a similar reduction in the energy capacity of the batteries.

Keywords: photovoltaic systems, electric vehicle, urban mobility, solar energy, electric charging.

Contents

List of Tables

List of Figures

Nomenclature

Greek symbols

α	Slope of the road [rad]
α_s	Solar altitude angle [°]
β	Tilt angle [°], linear regression coefficients
β_T	Temperature coefficient [$^\circ C^{-1}$]
Δ	Brightness parameter [$-$]
δ	Declination of Earth [°]
ϵ_i	Translational mass of rotating components [kg]
η	Efficiency [$-$]
γ_s	Azimuth Angle [°]
λ	Longitude [°]
ρ_g	Albedo [$-$]
ω	Angular frequency of rotation of the motor [rad/s], hour angle [°]
ϕ	Latitude [°]
ϕ_m	Average latitude [°]
ρ	Air density [$\mathrm{kg/m^3}$]
ρ_m	Optical air mass
θ	Incidence angle [°]
θ_z	Zenith angle [°]

Roman symbols

Δs_{tot}	Total distance traveled by the vehicle [m]
Δs_{xy}	Horizontal distance traveled by the vehicle [m]

a Vehicle acceleration [m/s^2]

A_f Vehicle frontal area [m^2]

C_d Aerodynamic drag coefficient [$-$]

C_{batt} Battery capacity [Wh]

C_{ele} Cost of electricity [$/kWh$]

C_{rate} Battery C rating [h^{-1}]

d_r Interest rate [$\%$]

$E_{EV,non-solar}$ Energy consumption of the vehicle without solar panels [$kWh/100\ km$]

E_{solar} Output energy of the solar panels measured [kWh]

E_{wheel} Energy at the wheels [Wh]

EoT Equation of time [min.]

F_g Gravitational Force [N]

f_r Rolling resistance coefficient [$-$]

F_{ad} Aerodynamic Force [N]

F_{rr} Rolling Friction [N]

F_{te} Traction Force [N]

g Acceleration of gravity [m/s^2]

G_h Total solar irradiance on the horizontal surface [W/m^2]

G_T Total solar irradiance on the tilted surface [W/m^2]

$G_{h,b}$ Beam irradiance on the horizontal surface [W/m^2]

$G_{h,d}$ Diffuse irradiance on the horizontal surface [W/m^2]

h Height of the vehicle [m]

I_{mpp} Maximum power point current [A]

i_r Inflation rate [$\%$]

I_{sh} Short circuit current [A]

k_T Clearness index

L_{st} Meridian for the local times zones [$^\circ$]

LST Local solar time [h]

LT Local time [h]

m Vehicle mass [kg]

P_{grid} Energy from the grid [W]

P_{max} Peak power[W]

P_{wheel} Power at the wheels [W]

R_b Ratio of the beam irradiance on the tilted surface to that on the horizontal surface [-]

r_w Radius of the wheel of the vehicle [m]

R_{earth} Earth Radius [km]

ROI Return on Investment [$\%$]

T Torque acting on the motor [$N \cdot m$]

T_{amb} Ambient air temperature [$^{\circ}C$]

T_{mod} Temperature of the solar modules [$^{\circ}C$]

T_{NOCT} Nominal operating cell temperature [$^{\circ}C$]

v Vehicle velocity [m/s]

v_w Wind velocity [m/s]

V_{mpp} Maximum power point voltage [V]

V_{oc} Open circuit voltage [V]

P_{solar} Output power of the solar panels measured [W]

A_{ac} Active area of solar module [m^2]

$F_{1,2}$ Brightness coefficients [$-$]

Subscripts

n Normal component

x, y, z Cartesian components

amb Ambient

avg Averaged

T Tilted surface of solar panels

Chapter 1

Introduction

1.1 Motivation

The transport sector has always played a pivotal role in the social-economic development of any country, still, despite significant advancements in all technological areas. This sector is responsible for nearly a quarter of energy-related greenhouse gas (GHG) emissions in the European Union (EU). In particular, road transport alone accounts for three-quarters of these emissions [1], and there is considerable dependence on fossil fuels. According to data provided by the Energy Information Administration (EIA), it is possible to infer that this trend is likely to continue being so until 2050 if no action is taken. Thus, it is of utmost importance to take immediate action to achieve carbon neutrality, to keeping the global average temperature rise well below the 2-degree mark, and to continue efforts to reach 1.5 degrees by that time, as targeted in Paris Agreement [2].

As a response to this problem, the transport *White Paper* proposed by the EU has developed a long-term roadmap for the transportation sector, promoting a decrease of 60% of GHG compared to preindustrial situations (1990) by 2050; an increasing share of the energy consumption produced by renewable energy at 32% to increase energy efficiency at 32.5% [1]. To achieve these ambitious goals, all conventional Internal Combustion Engine Vehicles (ICEVs) need to be replaced with more environmentally friendly Electric Vehicles (EVs). EVs are a more attractive alternative to address the problems of dependence on fossil fuels, the release of high levels of carbon dioxide (CO_2) emissions, and other harmful air pollutant emissions associated with road transport, such as NO_x and CO. Furthermore, EVs are much less noisy compared to ICEVs [3].

With regard to electricity generation, the emissions of EVs are largely dependent on the mix of energy used to produce the electricity they consume. In this regard, the full environmental benefits of EVs can only be achieved when they are powered by electricity systems with great share of renewable energy sources. To sustain this dependence, a recent study has reported that in 2019, 52% of the energy used for electric vehicles came from non-renewable electricity production [4].

Considering electric vehicles as a widespread replacement for conventional internal combustion engine vehicles, it is important to go into deeper detail at several different characteristics of this technology as well as what is going on from the market perspective. Therefore, in the following sections, a brief dis-

cussion of this novelty potential technology is given, as well as its main barriers preventing its adoption.

1.1.1 Electric Vehicles as a Solution

The idea of using electrical energy to propel vehicles is not new and was introduced more than a century ago. However, it was only in the 1990s that this technology began to gain room, mainly because of the scarcity of oil and the pressing problem of climate change. As a response, several auto manufacturers turned part of their efforts to improve this technology. Currently, it is possible to find on the market some variants of electric vehicles, which are grouped according to their characteristics and sources of energy [5].

- **Battery Electric Vehicle (BEV)** - this vehicle relies only and only on the energy stored in the batteries that can be recharged when connected to the power grid or other renewable source of energies. Like all EVs, a BEV can recover some quantum of energy and stores it back into the batteries through a process known as regenerative braking.
- **Hybrid Electric Vehicle (HEV)** - is a vehicle that uses two different sources to move the vehicle, generally an internal combustion engine and an electric motor that uses energy stored in a battery. The battery is charged by the internal combustion engines and from regenerative braking.
- **Plug-in Hybrid Electric Vehicle (PHEV)** which is an evolution of HEV, with added capability to be charged through the power grid, thus the name 'plug-in'.

Out of EV types, BEV is seen as a promising technology and is expected to play an indispensable role as a main mode of transportation shortly. Taken this situation, the focus of this dissertation is only on the battery powered electric vehicles. In fact, the vehicle used is an electric three-wheeler vehicle that belongs to the L5e category [1] in the European regulations [6], which will be studied afterward.

1.1.2 Market Outlook

The electric vehicles market have shown a significant increase in recent years. In 2021, global sales of electric vehicles surpassed the six million market after exceeding the three million mark in 2020, which represents an annual growth of more than double between 2020 and 2021 [7]. It is estimated that 6.5 million electric cars were sold in 2021, and 2.3 million were sold in Europe, of which 71% were BEV. Overall, the global market of electric vehicle was obviously affected by the ongoing COVID-19 pandemic. In the early stage of the pandemic, the automotive industry saw EV sales decline by 31% compared to previous years, but in the second half of 2020, this effect was offset by stronger measures and reached 16% at the end of the year [4]. Norway is the global leader in terms of EVs market shares, whilst China has the highest Volume of EVs sales, followed by Europe and United States as can be seen in Figure 1.1. In particular, Portugal is one of the countries with the highest EV shares and sales in Europe, with PEVs accounting for 8.8% in 2020, thanks to financial and political incentives such as tariffs, tax breaks, etc.

[1] L5e = Motorized try-cycle

Regarding the future projection of electric vehicles, a recent study released by Delloite in 2020 on the state of the EV market predicted for the next ten years. They showed that about 11.2 million of electric vehicles will be sold by 2025, and this number is expected to increase to 31.1 million by 2030. Furthermore, they also predict that electric vehicles sales will match the values before the COVID-19 pandemic until 2024 [8].

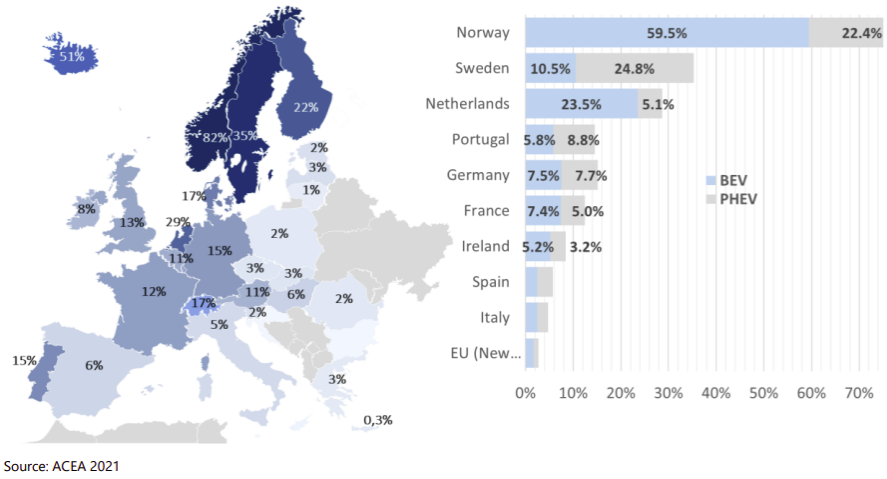

Figure 1.1: National EVs sales in Europe in 2020. This figure shows that is possible to reach 60% of BEV sales shares in 2030 if current market development are projected into the future. Source [7].

While the electric vehicle market is growing exponentially, the role of powered light vehicles in this sector has done indeed more so, this includes both two- and three-wheelers vehicles. In 2020, more than 350 million of these vehicles were already on the road. Due to their compact size and lightweight, these vehicles are expected to play a significant role in the total electrification of the transport sector. These vehicles are often used in urban areas that travel short distances at low speeds, carrying fairly small battery packs [4]. Since they generally do not require a license to drive, they are much easier to operate and handle mainly in urban areas, making the transition towards electric mobility more possible.

1.1.3 Barriers to Adoption of Electric Vehicles

However, despite the significant improvements shown in recent decades, there is still a lot of room for progress in this field. On the customer side, there are several barriers that still face the widespread adoption of electric vehicles. Several studies have already been conducted and point out to many **barriers** that need to be overcome to ensure the global diffusion of electric vehicles. According to these studies, these barriers are classified into 3 main categories. The social barrier, technical and economic barrier. Furthermore, a recent study by Delloite in 2018 stated that the four main obstacles that still hinder the widespread adoption of electric vehicles were: The cost of the vehicle, the insufficient range, the long charging times, and the need for a charging infrastructure [9].

In fact, these barriers are essentially linked; the bigger the battery capacity, the more it generally costs. Additionally, the larger the vehicle's range, the longer it generally takes to charge the batteries. The limited driving range along with the vehicle cost represent one of the main obstacles for the global

acceptance of electric vehicles, leading to a phenomenon called **range anxiety**.

Range anxiety is associated with fear or incapacity of the driver to be unable to reach the desired destination due to the limited range of the vehicle and due to the small battery capacity. Due to this, range anxiety is more evident in vehicles with lower battery packs, such as the one used in this work. Therefore, it is necessary to create solutions to solve this problem to allow electric mobility to occur.

1.1.4 Integrating Photovoltaic Energy Into Electric Vehicles

In an attempt to respond to the problems encountered in electric vehicles while reducing the use of fossil fuels to reduce environmental degradation, the world has been turning its attention to renewable energies. Among these, the widespread use of photovoltaic energy, which is a free, sustainable, renewable, and clean source, has grown exponentially and is considered the third largest renewable energy in terms of capacity and energy generation [10]. To sustain this growth, from an economic perspective, such developments are due to a significant drop of about 82$\%$ in the global average price of photovoltaic module over the last decade [11].

Solar photovoltaic (PV) technology can provide energy to electric vehicles through several ways. The most obvious way is to incorporate the solar photovoltaic panels directly onto the vehicle's roof, so that an additional energy can be generated, thus enabling the vehicle's battery to be charged while driving or even when the vehicle is parked. On the other hand, this approach opens up the possibility for the batteries to be undersized, resulting in direct savings in capital investment in the vehicle and operating costs. This method is often called vehicle integrated photovoltaic (VIPV) or on-board PV application [12, 13].

Another way of providing clean forms of energy to electric vehicles is through what is called the off-board method; contrary to the on-board method, solar PV panels are installed on a dedicated charging station or even on the roof of a building. However, this method is less complex to design because there is more space available for installation but requires additional infrastructure, such as battery storage, inverter, etc.

The goal of the present dissertation is to study the real potential benefits of on-board photovoltaic energy in a power light vehicle based on real-world data by providing an auxiliary charging of energy that does not need any extra energy storage systems but at the same time may reduce the energy consumed in the batteries while reducing the environmental degradation discussed previously, thus contributing to electric mobility.

1.2 Objectives

This work was developed within the framework of *Helianto Project* [14], which is a sustainable mobility project that encompasses several departments and scientific areas of the Instituto Superior Tecnico (IST) such as the Departments of Mechanical, Physics, and Electrical Engineering. The objective of Helianto project is to create technological solutions for electric vehicles with the great potential for industrialization.

Following the Helianto project goals, the objective of this thesis is the optimization of the process of charging electric vehicle batteries using on-board photovoltaic energy. The interest of this study is to quantify whether the proposed system can actually yields real improvements in the vehicle's performance. In contrast to a considerable sample of previous work found in the literature, the approach of this work is based on the daily history of journeys collected from an electric rickshaw, which will be studied in chapter 2.

To this end, the solar rickshaw was constructed first. This involved the construction of supporting equipment to accommodate the solar panels onto the vehicle's roof.

Then, a data acquisition system was developed in order to collect and acquire important variables from the set of different sensors located in the rickshaw. The data concerning the solar power output was collected from the Energy Meter (PZEM). The information regarding the battery pack was collected from the Battery Management System (BMS) and last, the information concerning the vehicle position was collected from a GPS receiver.

The data collected on vehicle usage will be analyzed and used to quantify the real potential benefits of the proposed system from an economic, and technological point of view. As said, this proposed system makes it possible to undersize the battery pack of the vehicle, so at the end of this master's thesis a new battery pack technology is expected to be proposed.

1.3 Thesis Outline

In the present chapter, the motivation and context problem studied in this work is given, followed by the objectives that this work aims to achieve and the approach adopted. The remainder of this dissertation is divided into seven chapters and the contribution of each one is briefly described as follows:

In chapter 2, a comprehensive literature review looking at various aspects of the rickshaw, namely: (a) its state of market and current projections for future adoption, and (b) a detailed review of the main technologies used. The goal of this chapter is to provide readers with information on the current state-of-the-art of this type of vehicle and its potential in the market, with a particular emphasis on solar technology. Chapters 3 and 4 are related to the theoretical background of this work. It starts by discussing the longitudinal vehicle dynamic model used to estimate the energy consumption for a given trip, followed by the theoretical concept regarding solar energy in chapter 4. Several models used to estimate the irradiance on a tilted surface are also described. Chapter 5 is related to the experimental part of the work. Firstly, how the solar panels are put into rickshaw's roof were explained. The data acquisition system used to collect data during vehicle movement is then described. In Chapter 6, the collected data was analyzed in order to mislead any imperfections that the data may have and to correct and prepare it for modeling. In chapter 7 the data collected during trips is used to analyzed the proposed low-cost solar rickshaw concept in terms of economic benefits and lastly, in chapter 8, the conclusions and the main contributions is present as well as possible considerations for future work.

Chapter 2

State of the Art

The main goal of this chapter is to present a literature review on the state-of-the-art electric rickshaw and how it relates to the present work. To do this, this chapter is divided into 3 sections. It starts with a general overview of the history of rickshaws and how they have evolved over time, followed by a description of their market status. In the second section, there is a general description of the key technological components that make up this vehicle. Section 2.2, presents a review of the previous work done using solar energy for charging electric rickshaws and how they are related to the work done in this master thesis.

2.1 Development of the Rickshaw

The Tuk-Tuk is a three-wheeler means of urban transport known by the most varied names, among which the most famous is the rickshaw. The word rickshaw comes from the Japanese word *jin riki sha* where *'jin'* - human , *'rick'* - power, and *'shaw'* - vehicle, which literally means human-powered vehicle, and this popular name is derived from the sound they produce when operating on the road [15]. Over the past century, the rickshaw has undergone many transformations, from hand-pulled to motor-assisted or electric rickshaws.

The original version of the rickshaws were used in tropical developing countries as they are not completely enclosed and relatively inexpensive to own and operate; however, the earliest known rickshaw is believed that was first developed in Japan and Italy in the late of 19th century (i.e., around 1870 [16]) and one of the oldest mode of transport of modern era [17]. Since then, the concept spread to every corner of the world such as China, India, Singapore, the French-Indo-China colonies, South Africa and for a brief time in America and Australia [16].

As said, currently there are different models of rickshaws, the original concept of this vehicle was a wheeled cart pulled by a man. Because of their easy-to-use in urban areas, it was rapidly utilized as a means of transport, its popularity suffered a big crash with invention of motorized public transport; though, during the 20th century this humble and ancient form of transport was finally reborn thanks to the improvements in the technology, including new versions of motors and pedals.

During World War II, electric motorized rickshaws emerged as taxi services to combat the scarce

supply of oil. They are widely used in different parts of Asia, Africa and South America; they operate as taxi services and tourist vehicles, as well as private and cargo transport. They come in many different designs with two, three, four wheels and each country has created its own nickname for his vehicles. These vehicles are commonly known in China as trishaw and auto-rickshaw in India, Tuk-Tuk in Egypt and Thailand, pedicabs in UK, USA and Philippines, babaji in Tanzania and Cambodia, tik tik in Madagascar, baby taxi in Bangladesd and ecologico in Mexico, just to name a few [16, 18]. These rickshaws are capable of carrying the driver and up to 4 people or payload up to 250 kg at a maximum speed of 12-25 km/h and expected to reach a distance of 40 km [16]. Figure 2.1 shows some examples of the rickshaws used for taxis and cargo services in developing and developed countries.

Figure 2.1: Examples of rickshaw diversities (a) Babaji known in Tanzania, (b) Tik Tik" in Madagascar and (c) Baby Taxi in Bangladesh. Adapted from [18].

In all of these countries their decoration is already an art form. In recent years, these vehicles have been arriving in Europe, especially in Lisbon. They are seen to making tours in the city center and are considered as the main mode of transportation by tourists to explore the city quickly and comfortably, contributing to the touristic ecosystem of the city [19].

2.1.1 Market Outlook

The electric rickshaw plays a crucial role in social and economic development in many countries due to their several advantages over conventional rickshaws, such as being very quieter, faster, and cleaner because they are powered by an electric motor instead of a diesel and petrol generator and also are cheaper to maintain.

Following a new recent report published by Allied Market Research, titled, *'Three-Wheeler Market by Fuel type and Vehicle Type: Global Opportunity Analysis and Industry Forecast, 2021-2028'*, it is possible to infer that the global rickshaw market size is evaluated at €7.94 billion in 2020, and is expected to reach €14.66 billion by 2028, representing an annual growth of 10.7% between 2020 and 2028 [20]. In Figure 2.2 it is represented the global electric rickshaw market size projected for the next seven years. It can be seen that, at present, the market for this three-wheeler is led by countries in the Asia-Pacific region (APAC) and will continue to do so at least until the forecast period, followed by Europe, the Middle East & Follow Africa, South America. Among Asian countries, India and Bangladesh have the highest number of electric rickshaws. It is estimated that there are more than 2.5 million of these vehicles, making it one of the most contributors to the Indian's economy; it is estimated that 6% of Indian's GDP (Gross Domestic Product) is due to these rickshaws [21].

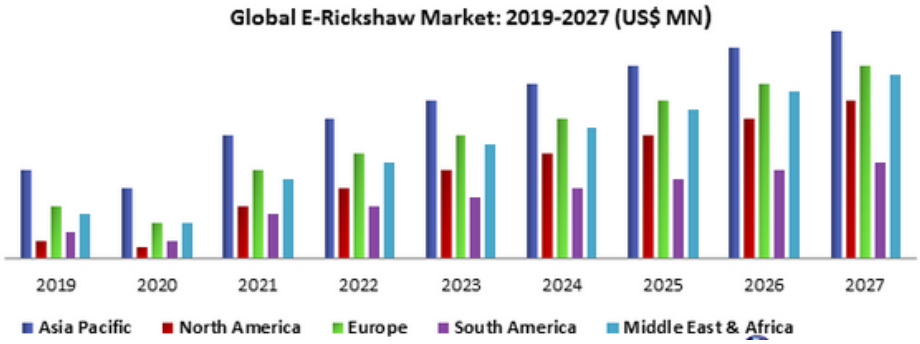

Figure 2.2: Global electric rickshaw market projection [20].

Following India, China has the second and most prominent market share of electric rickshaws in terms of production and sales, mainly due to rapid growth in urbanization and population. Europe is the second largest leader in terms of share, mainly due to concerns over environmental conditions, forcing them to adopt the electrification of vehicles in this region. Many electric rickshaws manufacturers are widely investing in innovating technologically advanced solutions. For example, the Tuk-Tuk factory company is an electric rickshaw company whose objective is to manufacture vehicles of the L category capable of experiencing speeds of up to 50 km/h. Usually, these rickshaws are equipped with an electric motor and an internal combustion engine [22].

2.1.2 Technological readiness of the components of Rickshaw

Batteries

It is argued that the batteries are one of the most important components of an electric vehicle. Based on this technology, the electric rickshaw is mostly equipped with lead-acid or lithium-ion batteries, as shown in figure 2.5(a). Of the two, the electric rickshaw powered by lead acid batteries had the highest volume sales in 2017, but due to the continuously lowering price of the lithium-ion batteries, it is expected that electric rickshaws powered by this type of technology will significantly grow in the coming decades. In addition to their decreasing price, these batteries have shown higher energy densities compared to the lead-acid ones, meaning that the battery size can be practically made smaller than other while maintaining at the same capacity. The average charging time required for a complete charge of lead acid batteries is around 10 h, whereas lithium ion batteries take approximately 4-6 h [22]. In addition, the majority of the rickshaws found in the market are classified as being rickshaws with battery capacity of less than 101 Ah and rickshaws with battery capacity more than 101 Ah.

Figure 2.5(b) shows the range of the specific power as a function of the specific energy for different types of battery technology, from which it can be seen that they differ a lot from one to another. The lead acid battery presents an specific energy in the range of 20 to 40 Wh/kg whilst lithium-ion batteries has a specific energy typically between 60 and 200 Wh/kg, which makes it suitable for vehicle with higher battery capacity.

Among the different variety of lithium-ion batteries that already exist in the market, $LiFePO_4$ is the most used because it is thermally and chemically stable. Despite having a lower specific energy

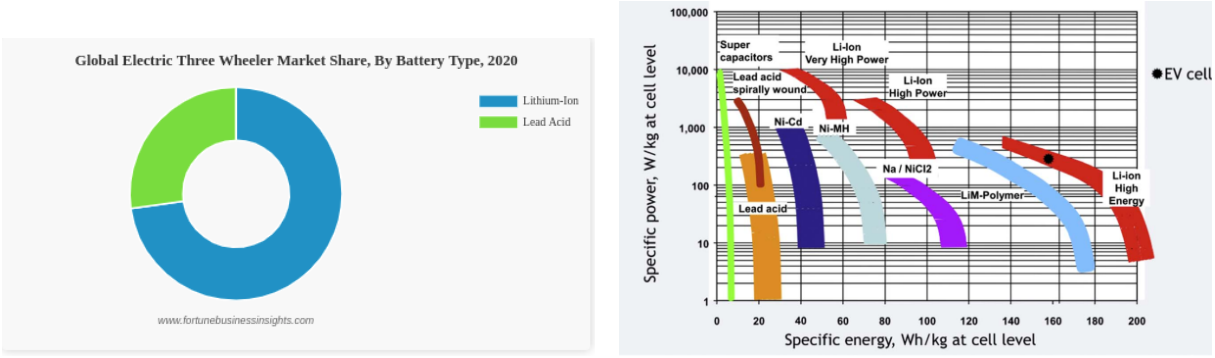

(a) (b)

Figure 2.3: (a) Global three-wheeler market share by battery type [23]. (b) Specific energy and power of the main battery technologies [22].

compared to its standard $LiNiMnCoO_2$, they are also safer and have a long cycle life (more than 2000 cycles) [22].

Electric Motors

As said above, the electric rickshaw uses an electric motor instead of an internal combustion engine for propulsion. The advantages of using an electric motor over an internal combustion engine are many; first, the conversion efficiency of electrical energy to mechanical energy is very high and usually lies between 70% and 90% [23]. Another benefit is that it is possible to use electric motor to act as a generator and recover some energy and store it in the batteries during regenerative braking mode.

Based on the motor power and design, the global electric rickshaw market is typically segmented into motors with power less than 1000 W, 1000 W - 1500 W, and motors with power greater than 1500 W. Those with motor power in the range of 1000 W - 1500 W have been dominating the market share due to their operational cost, making it a leading category in the market. However, due to the rapid growth of new technologies and the growing demand for high-speed electric rickshaws, some rickshaws with higher power ($\sim$ 5 kW) have begun to arrive on the market and are expected to double their volume in the coming years. Most of the lower power electric rickshaws found in the literature are equipped with DC motors because they are less expensive than AC motors and can be operated and handled safely with a minimum of friction losses [21]. However, for rickshaws with higher power needs, induction motors are considered the best solutions. In Table 2.1 it is shown the characterization of rickshaws by battery capacity and motor capacity as well as common type of technologies used.

As discussed in sub-section 1.1.4, one of the main barriers to global acceptance of electric vehicles and, in particular, electric rickshaws, are the higher costs of batteries and the limited range. So the adoption of the solar photovoltaic energy appears as a good option. In the following section, we give the relevant work available in the literature on previous studies using on-board photovoltaic systems to charge vehicle batteries. Most of the studies found in the literature are based on simulations models used to access the performance, but there is a considerable amount of works focused on experimental data, which is the approach used in this work.

Table 2.1: Electric rickshaw market segment.

	Subsegments
End User	Passenger carriers
	Load carriers
Motor Power (W)	< 1000
	$1000 - 1500$
	> 1500
Motor Type	Brushless DC motor
	AC Induction motor
Battery Capacity (Ah)	< 101
	> 101
Battery Technology	Lead Acid
	Lithium-ion

2.2 Solar Powered Vehicles

Solar-powered vehicles are vehicles powered either entirely or partially by solar energy. Photovoltaic cells that constitute each module convert sun's energy into electrical energy that can be used to charge batteries or power other auxiliary functions. At present, solar vehicles are not yet sold as practical and day-to-day means of transportation, but are primarily demonstration vehicles and experimental engineering projects, often sponsored by government agencies. The most notable is the World Solar Challenge (WSC) race in Australia, which refers to competitive races of electric vehicles with the main goal of promoting research on solar-powered cars. In this competition, several universities participate in the races in order to give their students experience in designing high technology cars. Figure 2.4 shows the first commercialized car of the solar family, called *Stella Lux* which was designed and build in 2013 by students of University of Eindhoven [24]. According to these investigators, this vehicle is capable of covering 780 kilometers with a single charge during winter at a top speed of 125 km/h. It weighs 388 kg, and a set of 381 monocrystalline silicon cells is combined, which makes up a peak power of 1.5 kW. The result of such a high range in this vehicle is that even on a cloudy day, the energy generated by the solar panels is maximized by making use of a non-reflective surface made up of tiny prisms layered over the solar panels array. In this way, the prisms bend the diffracted light so that it arrives perpendicular to the solar cells, thereby increasing power out of the solar panels under all conditions. This technique has demonstrated a maximum efficiency conversion of 24$\%$, which is higher compared to the maximum possible efficiency of a typical monocrystalline silicon cells [24].

Several studies have found where photovoltaics integrated into passenger electric vehicles have been deployed or are in development. One example are the case Lightyear one and Sono Motors in Netherlands and Germany, respectively [25, 26], both have integrated monocrystalline silicon solar cells onto the body vehicles. According to these companies, these cars would provide more than 30 km of daily range on a typical sunny summer day in temperate climates, and also a daily range of at least 10 km on a sunny winter day.

With regard to electric rickshaw, on-board photovoltaic has been investigated for this type of vehicle; Mulhall et al. [17] proposed the design of a solar-assisted electric rickshaw for Indian conditions. They simulated the performance of the solar rickshaw with the two monocrystalline solar panels with an ef-

Figure 2.4: Photo of the Stella solar vehicle [20].

(a) Lightyear

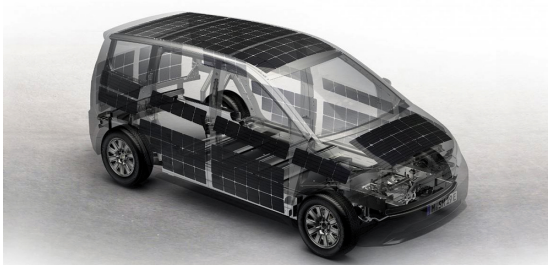

(b) Sono Motors

Figure 2.5: Photovoltaic Electric Vehicle concepts. Lightyear One (picture: Lightyear) (a), Sion solar car (picture: Sono Motors GmbH)(b).

ficiency conversion of 20.1% rated at 327 W and showed that the solar panels could lead to a range extension of 44 km/day. Reddy et al. [27] presented the design and development of the solar powered electric auto rickshaw in India. They simulate and measured the performance of the system. The results reveal an optimal charging rate of 2 kWh/day with an average solar irradiance of 325 W/m^2 on a typical sunny day. However, there are no previous studies on the optimization and evaluation of the system-level benefits of the solar rickshaw for Portugal conditions.

There are also a lot of challenges to be overcome before the solar-powered vehicles can become a reality. First, there is the integration of an MPPT (Maximum Power Point Tracking) controller in order to increase the power extract out of the solar photovoltaic panels array for charging the batteries. In addition, the MPPT controller need to be designed in such a way that it can quickly respond to the shading problems which can occur when the vehicle is driven on the road. Since there is a lot of progress to be made in order to overcome these challenges, it is fundamental to first evaluate the benefits of the solar electric rickshaw to determine the competitiveness of this vehicle in the market compared to the conventional electric rickshaw.

Chapter 3

Vehicle Modeling

The model of an EV is very complex as it contains various components with different levels of complexity, e.g., power electronics, transmission, motor, battery, etc., and each component needs to be properly modeled to prevent wrong results in energy consumption. As a result, to predict the energy consumption of an EV, an accurate and reliable energy prediction model is needed. A considerable amount of research has been done in order to estimate the energy consumption spent on a vehicle trip, and a major part of the modeling is classified into two groups: physical modeling and statistical modeling. Physical modeling, as its name suggests, consists of understanding the physics behind vehicle dynamics and powertrain operation, and statistical modeling, on the other hand, relies on the exploration of the statistical principles between the inputs and energy outputs with certain statistical models.

In this chapter, the theoretical basis for the energy consumption of a trip is introduced. The model described here was used throughout chapter 5. The first section aims to describe the proposed system architecture, that is, the very energy harvested by the solar panels to the energy that must be used for the vehicle to move forward, which will be the bedrock for understanding the VIPV in chapter 4. The second subsection describes the physical model used to estimate the energy consumption of the vehicle on a trip, its physical meaning, and the choice of the typical parameters considered for the model.

3.1 System Architecture

As mentioned above, the energy consumption of any EV requires knowledge of each component of the vehicle. The full treatment of vehicle dynamics is beyond the scope of this work, as it would make up a Master Thesis on its own. Because of that, only the longitudinal dynamics of the vehicle will be addressed here. In Figure 3.1, a simplified version of the solar panels-to-wheel and wheel-to-battery energy flow in a typical BEV is shown.

Abstractly speaking , the energy flow model may be divided into two categories: the charging and driving process. In the former process, the necessary energy to charge the battery pack is typically taken from the grid supply when the vehicle is at a charging station or directly from the solar panels once there is sunshine. And in the driving process, the energy stored in the batteries is used to spend during the vehicle movement. The main function of the battery here is to act as a reservoir of energy that stores

the necessary energy to be used during the trip and also to be charged by the solar power while driving or even on the vehicle is parked. The batteries are connected to the inverter, which provides energy to the electric motor. The electric motor, on the other hand, is responsible for converting the electric energy into mechanical energy that, in turn, is transmitted to the wheels through the drive shaft, which is used to overcome the acting forces on the vehicle. From Figure 3.1, it is possible to see that the battery also provides energy to the auxiliary loads, which are external systems that interact with the vehicle, such as lighting systems, information systems, etc., but are not fundamental for the vehicle model. Since their contribution to the vehicle consumption is small compared to the other systems, the auxiliary power systems were promptly disregarded.

An important note with BEV is that the vehicle can effectively recover and store some energy back into the batteries during regenerative braking. In this case, the motor act as a generator, and the energy flows from the wheel to the battery as represented in Figure 3.1.

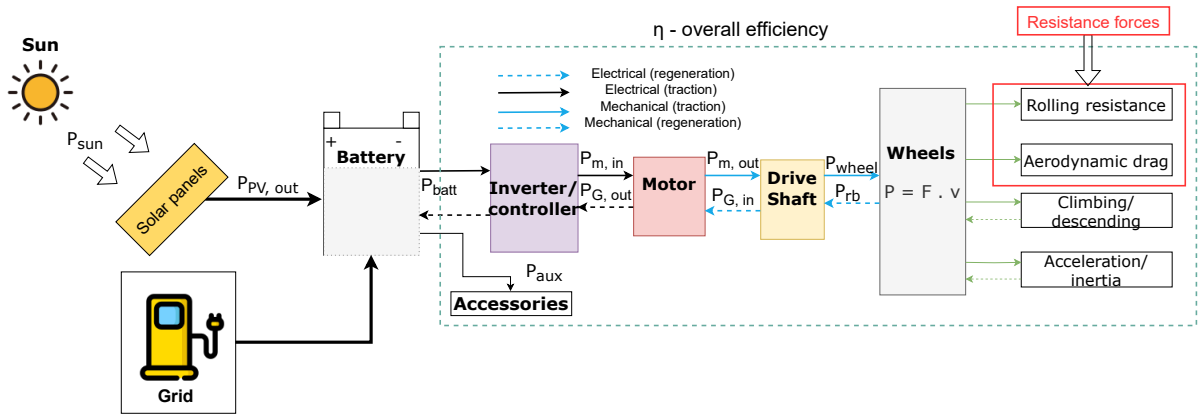

Figure 3.1: Schematic representation of the sun-to-wheel and wheel-to-battery energy flows of the BEV while driving — $P_{PV,out}$: *PV output power*; P_{bat}: *battery power*; P_{aux}: *auxiliary power usage*; $P_{M,in}$: *motor input power*; $P_{M,out}$: *motor output power*; $P_{G,in}$: *generator input power*, $P_{G,out}$: *generator output power*, P_{wheel} : *power required at wheels*, P_{rb}: *regenerative braking power*. η: represents the joint efficiency of the components in the power-train. Black lines: electrical power, blue: mechanical power, green: acting forces. Dashed lines represent flows related to regenerative braking.

It is of relevance to note that in each step of energy conversion, there are losses that need to be properly modeled, that is, the energy reaching one component is not the same as it was in its beginning. One of the components that affects the vehicle's energy consumption the most is the motor. The electric motor changes its efficiency depending on its torque and angular velocity. A widely used approach to determining motor efficiency is to use efficiency maps as lookup tables and find the efficiency for each torque and velocity pair [28]. The efficiency η_{tot} of the motor can be quantified using the following equation, where P_{wheel} is the input power seen on the wheels provided by the motor and P_{meas} is the output power measured at the battery terminal provided by the BMS. This efficiency represents the joint efficiency of all the components in the power train, as shown in the Figure 3.1.

$$\eta_{tot}(\omega, T_l) = \frac{P_{wheel}}{P_{meas}} \tag{3.1}$$

The following figure shows an example of the efficiency map of the rickshaw motor under study. The

peak power of the motor is rated for 7 kW, peak torque of 21.56 N.m, and a maximum angular velocity of 3100 RPM.

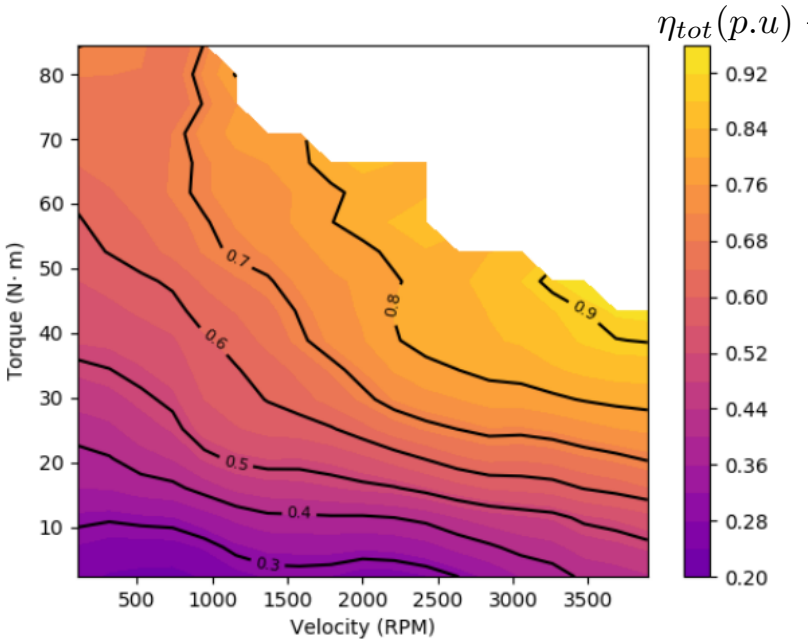

Figure 3.2: Example of an efficiency map of the electric rickshaw motor estimated using look-up tables from the previous work [28].

3.1.1 Longitudinal Dynamics Model

The most common physical model used to estimate the mechanical power seen at the wheels is the longitudinal vehicle model. It is a very simple approach that relies on the approximation that all forces act exactly at the center of mass of the vehicle, having been used successfully in several studies for vehicle simulations [28, 29].

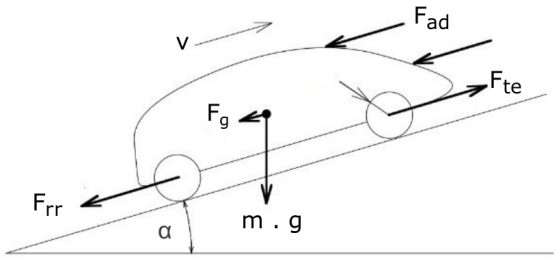

Figure 3.3: Relevant forces acting on an electric vehicle moving on an inclined road considered for the typical longitudinal dynamics modeling. (F_{te} - *traction force*, F_{ad} - *aerodynamic drag force*, F_{rr} - *rolling resistance force* , F_g - *gravitational force*. Figure adapted from [30].

To better understand this model, one should start by studying Figure 3.3, which summarizes all the necessary forces that act on vehicle movement. These forces are the aerodynamic drag force F_{ad}, the rolling resistance force F_{rr}, and the gravitational force F_g, and to overcome all these forces, a traction force is used F_{te}. Using these assumptions and applying Newton's second law of motion, it is possible

to obtain the main equation that governs this model, which is expressed in equation 3.2 below.

$$m(1+\epsilon_i)\frac{d}{dt}v(t) = F_{te}(t) - \{F_{ad}(t) + F_{rr}(t) + F_g(t)\} \tag{3.2}$$

where m is the vehicle mass and $(1+\epsilon_i)$ is a factor that represents the influence of the inertia of rotating components, such as motor, wheels, gearbox, etc. It depends on the speed at which the vehicle drives, but in this work it is assumed to be constant and equal to 1.05 [30].

Aerodynamic Friction Losses

Aerodynamic forces are one of the most important factors affecting vehicle performance and energy consumption. These forces originate due to the force exerted by the air along the axial movement of the vehicle. During the vehicle motion, several types of forces are generated, but the most important one is drag friction as it is the one that affects the energy consumption the most.

The drag force is heavily dependent on the shape of the vehicle and the surface material. As it varies from vehicle to vehicle, it is commonly determined using Computational Fluid Dynamics (CFD) simulations and using wind-tunnel experiments [30].

As stated previously, the drag force acts to oppose the movement of the vehicle, creating a higher pressure in the vehicle's front and a lower one in its rear. The difference in pressure originates the drag force. A simpler formula commonly used in vehicle simulations is to approximate that the drag force depends upon the vehicle velocity v, frontal area A_f, that is, the projected area that one sees when looking directly at the vehicle front and the aerodynamic drag coefficient C_d, as expressed in equation 3.3.

$$F_{ad}(v) = \frac{1}{2}\rho A_f C_d (v_{eff})^2 \tag{3.3}$$

where v_{eff} is the effective wind velocity, which is the difference between the vehicle velocity and the direction of the wind velocity. From equation 3.3, it can be seen that the drag force is directly proportional to the square of the velocity. This means that the resistance due to drag force increases parabolically as velocity increases. From now on, we cannot compute this force yet, because we need to estimate all its parameters first. The coefficient of drag can be considered constant for a turbulent Reynolds number ($Re > 3000$). Re is a factor that quantifies the degree of fluctuation of a fluid. For the air at a temperature of $20°$C, a pressure of 100 kPa, and a density of air [1] $\rho = 1.2256\ kg/m^3$, we find that $Re \approx 10^6$, meaning that the drag coefficient can be considered constant all the vehicle movement and one should simply approximate the drag force as given in equation 3.3.

For simplicity reasons, we did not consider the effect of wind velocity because its contribution on average is negligible compared to the vehicle's velocity and thus ($v_{eff} \sim v$). Taking all these simplifications, the aerodynamic drag force can be rewritten as expressed in equation 3.4, where v is simply the vehicle speed, the one measured by the GPS receiver.

[1] Density of air at sea level at $15°$.

$$F_{ad}(v) = \frac{1}{2}\rho \cdot A_f \cdot C_d \cdot v^2 \tag{3.4}$$

Rolling Friction Losses

Another major vehicle resistance that affects its consumption is the resistance to tire roll. This force occurs due to contact between the tires and the driving surface. At low speeds, the rolling resistance is the main dissipative force, while the other resistance forces act under certain conditions of motion, the rolling resistance force arises as soon as the vehicle starts moving. In this movement, several mechanisms may cause the loss of energy in the tires. The energy loss due to tire deformation, that is, the amount of energy lost when tires meet the pavement behaves like a hysteresis process, which states that the characteristic of a deformable material is such that the energy of deformation is greater than the energy of recovery and this energy loss is dissipated as heat. Another mechanism is the loss due to friction between the tire and the pavement, which depends on the type of pavement that shows higher values in sand than in asphalt [30].

Considering the vehicle as a whole, the total rolling resistance force acting in the opposite direction in the tire motion is given by equation 3.5 below. When the vehicle moves on a non-horizontal road, the weight W should be replaced by the component that is normal to the road surface:

$$F_{rr}(v, p, ...) = f_r(v, p, ...) \cdot W = f_r(v, p, ...) \cdot m \cdot g \cdot \cos\alpha \tag{3.5}$$

where $f_r(v, p, ...)$ is the coefficient of rolling resistance, g is the acceleration due to gravity, and α is the road slope given in radians.

As seen in the equation above, the rolling resistance coefficient, $f_r(v, p, ...)$ is a function of the vehicle velocity, but is also a function of tire material, tire temperature, tire inflation pressure, etc. [30]. Several studies have been conducted to gather information for calculating the rolling resistance coefficient as a function of velocity. Most of these studies assumed that rolling resistance coefficients vary linearly with velocity on concrete roads. This approximation gives a satisfactory estimate for low and median velocities (up to 120 km), which is more than suitable for the case of the vehicle under study. Having said this, the expression for the rolling resistance coefficient is given by the equation 3.6 below, where f_{r0} is the constant rolling coefficient and Q is a constant defined as being equal to 160 km/h to account for the small velocity dependence of the rolling resistance [30]. The final equation for the rolling resistance force is given by:

$$F_{rr} = f_{r0} \cdot m \cdot g \cdot \cos\alpha \cdot \left(1 + \frac{v}{Q}\right) \tag{3.6}$$

Gravitational Force

This force has a major effect on vehicle energy consumption when traveling on non-horizontal roads. When a vehicle either goes down or up a slope, its weight produces a component that is directed downward, as can be seen in the figure 3.3. This component is either positive when climbing a slope or

negative when descending a downslope. The gravitational force that the vehicle has to overcome when moving forward is

$$F_g(\alpha) = m \cdot g \cdot \sin\alpha \tag{3.7}$$

where α is the road slope with respect to the horizontal that the vehicle makes, g is the gravitational acceleration constant and m is the total mass of the vehicle already seen in previous equations.

3.1.2 Trip Energy Consumption Estimation

To find the energy spend on a trip, we need to integrate the traction force over the length traveled by the vehicle. The result of such an integration can be seen in the equation below. It is interesting to note that this energy corresponds to the variation of energy in the batteries and also corresponds to the energy that is provided to the motor to move forward. As a result, energy is converted into various forms of energy, some of which are stored in the vehicle system and others are lost, clearly seen in the equation 3.9.

$$E_{wheel} = \int_{s_i}^{s_f} F_{te} \cdot ds = m(1+\epsilon_i) \int_{s_i}^{s_f} \frac{dv}{dt} \cdot ds + \int_{s_i}^{s_f} (F_g + F_{ad} + F_{rr}) \cdot ds \tag{3.8}$$

$$\begin{aligned} E_{wheel} = & \underbrace{\frac{1}{2} m \cdot (1+\epsilon_i) \cdot \left[v^2(s_f) - v^2(s_i)\right]}_{\text{Kinetic Energy Variation}} + \underbrace{m \cdot g \cdot [h(s_f) - h(s_i)]}_{\text{Potential Gravitational Energy Variation}} \\ & \underbrace{+ f_{r0} \cdot m \cdot g \left(\Delta s + \int_{s_i}^{s_f} v \cdot ds\right) + \frac{1}{2} \rho \cdot A_f \cdot C_d \cdot \int_{s_i}^{s_f} v^2 \cdot ds}_{\text{Energy Losses = Rolling + Aerodynamic Frictions Energy Dissipation}} \end{aligned} \tag{3.9}$$

Using the traction force F_{te} we can also estimate the instantaneous power provided at the wheels and given by equation 3.10.

$$P_{wheel} = F_{te} \cdot v \tag{3.10}$$

Power Requirements

Up to this point, only a set of equations has been formulated that can be used to determine the desired energy consumption of a trip. However, this estimation is dependent on the several vehicle parameters. Therefore, it is interesting to estimate the different forces acting on vehicle movement using the parameters tabulated in Table 3.1, how much would they contribute to energy consumption for certain conditions of vehicle movement.

In Figure 3.4(a), the variation of the acting forces is plotted as a function of the vehicle velocity. The graph was made considering that the vehicle is moving on a horizontal plane, where the slope is zero. From this graph we can observe that about 2.0 kW is needed to overcome the aerodynamic drag and

Table 3.1: Suggested longitudinal model vehicle parameters for the **rickshaw Limo GT** vehicle.

Constant	Description	Value/Reference
ρ	Air density	1.225 kg/m^3
f_{r0}	Rolling resistance	0.012 [29]
m	Mass of vehicle	903 kg (Sec. 5.3)
$1+\epsilon_i$	Fictitious mass	1.05 kg [30]
C_dA_f	Drag area	1.75 m^2 [29]

the rolling resistance frictions. It is also worth noting that aerodynamic drag friction does not have a significant effect on vehicle energy consumption and is mostly insignificant for lower velocities (up to 15 km/h). This is to expected because the velocity of this vehicle is relatively small ($v_{max} = 43.2$ km/h). Meanwhile, rolling resistance friction cannot be ignored, as it depends on the type of road, tires, etc., causing its contribution to be present in all ranges of velocity values.

The contribution of gravitational force is also investigated, as can be seen in Figure 3.4(b) for various cases of road slopes. Looking at the figure, it becomes clear that gravitational force is the biggest contributing factor for energy consumption. For example, for the vehicle driving on a flat plane, the total required power is within the range expected from the figure 3.4(a), while for an inclination of 5%, which corresponds to 2.86 degrees, about 8.8 kW is needed to overcome the acting forces in the vehicle, etc. This is to be expected because the instantaneous power provided at the wheels increases with the increasing velocity, as can be noted in equation 3.10.

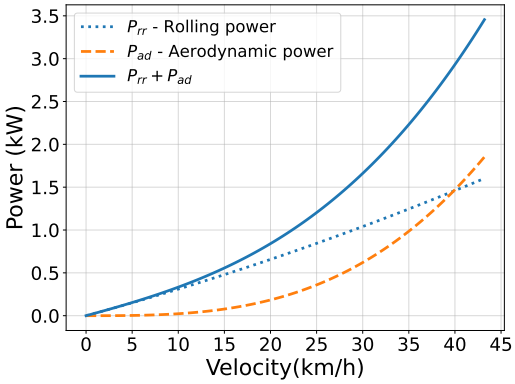

(a) Aerodynamic and rolling friction as a function of the velocity for slope $\alpha = 0$.

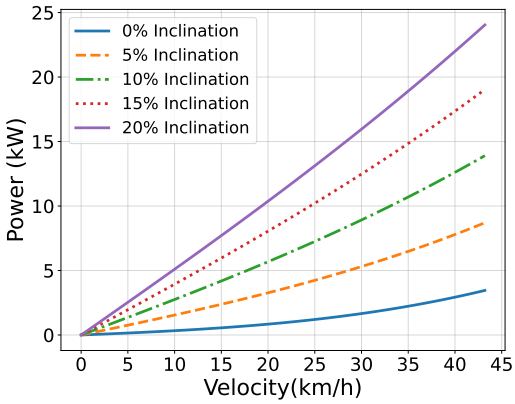

(b) Power required to maintain certain speed for different cases of road slopes.

Figure 3.4: Comparison between the power magnitudes for the E-rickshaw parameters under table 3.1 as a function of velocity.

Chapter 4

The Study of Photovoltaic Solar Resource

The first logical step towards understanding the performance of photovoltaic systems and any other system that converts solar energy into other forms of energy should be the study of solar radiation on the Earth and its characteristics. In the first section, we provide a brief overview of the sun and the amount of solar energy available at the solar panel surface. The several models used to compute solar radiation at any desired panel tilt surface are discussed. In the second section, the topic switches to the notion of solar photovoltaic systems, how they are formed, and how some properties of solar panels can be computed. The chapter ends with an experimental procedure carried out to investigates the environmental factors affecting the performance of the photovoltaic panels working under varying environmental conditions.

4.1 Solar Resource

It is well known that the largest source of energy available on Earth comes from the energy emitted by the Sun. This energy source forms the basis of all terrestrial life and is one of the most *environmentally friendly*. In a good approximation, the Sun behaves like a perfect black body [1] at an effective temperature of 5777 K that radiates outwards in the form of electromagnetic waves in all directions through space at the speed of light and reaches the earth's surface afterward. This never-ending amount of energy arises from the continuous nuclear fusion reaction that occurs deep inside its core, in which atoms of hydrogen are transformed into atoms of helium [31].

As the Sun is about 149.6 million kilometers away from Earth, the intensity of solar radiation emitted by the Sun (right before it enters in the atmosphere) is practically constant and is treated as extraterrestrial radiation but the energy that reaches the Earth's surface is more variable and in a small quantity. From the extraterrestrial standpoint, it is possible to define the solar constant, G_{SC}, as the maximum incident radiation, per unit time, received on a unit area of the surface at the Earth-Sun distance on

[1] In fact the sun is not a perfect back-body radiator.. However, in a good approximation, it can be assumed that it is a black body since its spectral distribution is very similar to that of the black body

the plane perpendicular to the direction of the Sun. Its value has varied over the years with increasing accuracy of instrumentation, but a commonly adopted value by the World Solar Radiation Center (WRC) is $1367 \pm 1\%$ W/m^2. As the Earth changes its distance throughout the year, the actual extraterrestrial radiation is different from G_{SC} and varies in the range of $\pm 3.3\%$. As would be expected, its maximum value occurs at the turn of the year, i.e., when the sun is closest to Earth and the minimum at the beginning of the July when the sun is farthest away from Earth, as it is possible to observe in Figure 4.1. An empirical mathematical expression that quantifies these variations with a reasonable degree of accuracy is given by [31].

$$G_{o,n} = G_{SC}\left[1 + 0.033\cos(\frac{360d_n}{365})\right] \tag{4.1}$$

where d_n is any given day of the year counted from the beginning of the year. The subscript n indicates that the radiation is measured in the plane normal to the Sun.

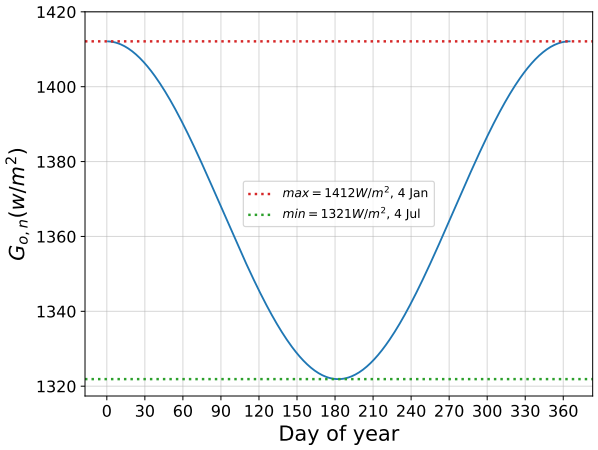

Figure 4.1: Variation of $G_{o,n}$ with the time of the year.

At this point, it is important to define two important variables: the first is the concept of irradiance, which is the incident solar power per unit of area and is commonly measured in W/m^2, and irradiation, on the other hand, is the incident solar energy per unit of area obtained by integrating the irradiance over a period of time and is measured in kWh/m^2 [31, 32].

Figure 4.2(a) shows an illustrative path that solar radiation takes to reach the terrestrial module's surface. As can be seen, the radiation when passing through the atmosphere is subjected to various interactions mainly by scattering, in which the solar radiation interacts with air molecules, aerosols, clouds, etc, and consequently reduces the amount of that energy, and part of the solar radiation is reflected out into space and escapes to the atmosphere [32]. The result of all of these interactions is the decomposition of the solar radiation incident on the Earth's surface into clearly differentiated components. These components are beam and diffuse radiations: beam or direct radiation made up of all the radiation coming directly from the sun's rays towards the earth's surface without it having been scattered or deviated by the mechanisms of the atmosphere mentioned above. *Diffuse radiation*, on the other hand, corresponds to radiation that was scattered by components of the atmosphere. The total solar radiation falling on a surface is the algebraic sum of all these radiation components (Beam + Diffuse).

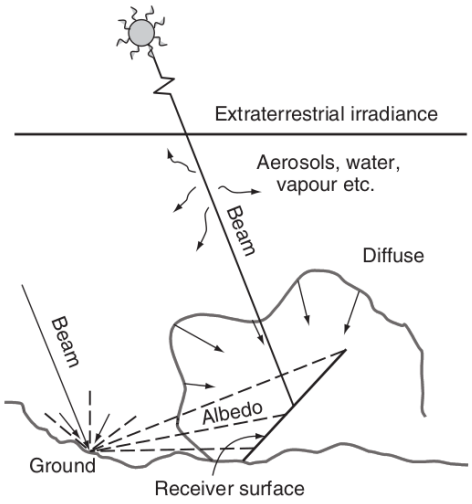

(a) Components of radiation emitted by the sun as it enters the atmosphere taken from [33].

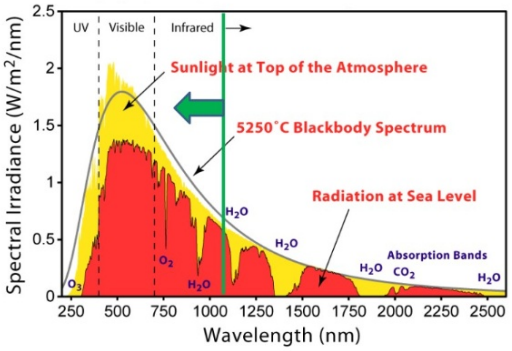

(b) Different solar spectra, adapted from [34].

Figure 4.2: (a) Different components of solar radiation that reach a terrestrial solar module surface. (b) The radiation spectrum for a black body at 5250 K, an AM0 spectrum, and an AM1.5 global spectrum.

4.2 The Effect of Atmosphere on Sunlight

As stated previously, the amount of solar radiation received by a terrestrial surface depends on several factors, such as the tickiness of the ozone layer, the distance it has to travel through the atmosphere to reach the terrestrial surface, the amount of dust particles, etc. [32]. The degree of attenuation that accounts for these effects is described by *relative optical air mass*, ρ_m, which corresponds to the ratio between the distance the beam radiation has to travel through the atmosphere and the distance through which it would travel if it were exactly in the vertical position (at zenith). The air mass is related with the zenith angle, θ_z by $\rho_m := 1/\cos\theta_z$, which is only valid for $0° < \theta_z < 70°$. However, for $70° < \theta_z < 90°$, there is a more detailed equation developed by Kasten and Young (1989) [35], which takes the curvature of the Earth into account.

$$\rho_m = \frac{e^{-0.00011844 \cdot h}}{\cos\theta_z + 0.5057(96.080 - \theta_z)^{-1.634}} \tag{4.2}$$

where h is the site altitude. Nevertheless, one can note that when θ_z, that is, when the sun is directly overhead, $\rho_m = 1$ (air mass one); when $\theta_z = 60°$ corresponds to air mass 2. In the case of radiation outside the atmosphere, the air mass is 1.5, which corresponds as a reference for terrestrial testing adopted by the American Society for Testing and Materials [32] as it corresponds to the zenith angle of $\theta_z \approx 48.2°$ representing the mean global mid-latitude region [34]. In Figure 4.2(b), a comparison between different air mass spectra and the black body distribution at 6000 K is shown.

4.3 Tracking the Sun

4.3.1 Solar Time

In almost all solar system calculations, it is used *solar time* instead of the standard clock time. This is because the apparent movement of the Sun in the sky is not uniform and since the Earth orbit is elliptic and tilted with respect to the orbit, sometimes the Sun appears to be ahead of the standard time and sometimes behind it, up to as much as 16 min. Rather, since most of the solar radiation measurements provide standard time, it is necessary to be able to convert the standard time into true solar time. This can be achieved by making two corrections: The first is to correct the difference in longitude between the observer's meridian and the meridian at which the standard clock time is based, and the second correction is related to the equation of time, which takes into account the disturbance in the Earth's rotation rates. That being said, the local solar time follows the equation 4.3.

$$LST = LT + \frac{4(L_{st} - \lambda) + EoT(d_n)}{60} \tag{4.3}$$

where LT is the local or clock time in hours, L_{st} is the meridian of the local time zones in degrees and λ is the longitude of the location in question. L_{st} can be determined by taking the difference in standard time from Greenwich Mean Time (ΔGMT) multiplied by a factor of $15°$. The equation of time can be calculated using the following equation [31], being $B = 2\pi(d_n - 1)/365$.

$$EoT(d_n) = 2.292(0.0075 + 0.1868\cos B - 3.2077\sin B - 1.4615\cos 2B - 4.089\sin 2B) \tag{4.4}$$

4.3.2 Beam Radiation: Solar Angles

To be able to characterize the position of the sun in the sky, two coordinates are required. In fact, are 3, but since the distance between the sun and earth is considered constant, only 2 coordinates are required. The common choices are (i) the solar altitude angle and (ii) the azimuth angle. These angles are physical parameters of the position of the sun with respect to a given place on Earth and are therefore independent of the inclination and orientation of the surface [36] (see Figure 4.3).

The solar altitude or the elevation angle, α_s, is the angle between the sun axis and the horizontal line. It is defined as $0°$ at sunrise/sunset and $90°$ when the sun is directly overhead. The elevation is the complement of the zenith angle θ_z, that is, the angle between the sun axis and the vertical line ($\theta_z = 90° - \alpha_s$).

The solar azimuth angle, γ_s, describes the position of the Sun in the sky and accounts for the displacement relative to the south (the true south). The sign convention used is positive for the west and negative for the east. The azimuth angle can be calculated using the following formula.

$$\cos\gamma_s = \left|\frac{\cos\theta_z\sin\phi - \sin\delta}{\sin\theta_z\cos\phi}\right| \cdot sign(\omega) \tag{4.5}$$

On the other hand, there are two variables that specify the position of the solar panels: the tilt angle

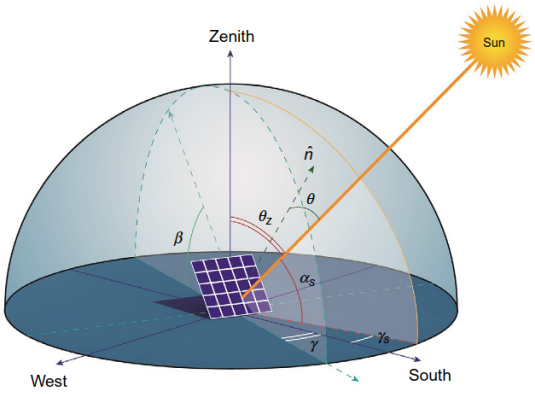

Figure 4.3: Schematic representation of the sun and solar panel characteristic angles [36]. Some relevant angles are: β tilt panel, θ_z zenith angle, α_s altitude angle, γ_s solar azimuth angle, θ incidence angle, δ declination, ω hour angle.

or slope, β, is the angle between the horizontal line and the plane of the surface in question, it varies between $0°$ and $90°$, and the surface azimuth angle, γ, is defined as the deviation on a horizontal plane normal to the surface from the local meridian, it is zero due south and lies between $-180° < \gamma < 180°$.

In Figure 4.3, all the aforementioned angles between the Sun's position with respect to an oriented panel are depicted. For further calculations, it is possible to write the incident angle, θ, between the incoming beam radiation and the normal to the surface of the solar panel. This relationship can be seen in the following equation.

$$\begin{aligned}\cos\theta = \; & \sin\delta\sin\phi\cos\beta - \sin\delta\cos\phi\sin\beta\cos\gamma \\ & + \cos\gamma\cos\phi\cos\beta\cos\omega + \cos\delta\sin\phi\sin\beta\cos\gamma\cos\omega \\ & + \cos\delta\sin\beta\sin\gamma\sin\omega\end{aligned} \tag{4.6}$$

where δ is the solar declination, which is defined as the angle between the sun's rays and the equatorial plane. It ranges between $-23.45° < \delta < 23.45°$ due to the tilt of Earth on its axis and its rotation around the sun. This parameter is considered positive in the northern hemisphere and negative in the southern hemisphere. The solar declination δ, for any day of the year with reasonable precision, can be determined using the following equation [31],

$$\delta = 23.45° \sin[\frac{360 \times (284 + d_n)}{365}] \tag{4.7}$$

the latitude of the surface location ϕ, is defined as either positive (North) or negative (South), ω, is the hour angle, that is, the angular deviation of the sun relative to the local meridian due to the rotation of the earth on its axis at $(360°/24 = 15°)$, being negative in the morning and positive in the afternoon. The equation used to calculate the hour angle is given below.

$$\omega = 15°(LST - 12) \tag{4.8}$$

It should be noted that in equation 4.6, for a horizontal surface, that is, for $\beta = 0$, the incidence angle corresponds to the zenith angle, and equation 4.6 simplifies to

$$\cos\theta_z = \sin\delta\sin\phi + \cos\delta\cos\phi\cos\omega = \sin\alpha_s \tag{4.9}$$

From the equation above one can obtain the sunset an sunrise hours angle, which is the case when the sun is on the horizon ($\cos\theta_z := 1$)

$$\omega_{ss} = \arccos[-\tan(\delta) \times \tan(\phi)] = -\omega_{sr} \tag{4.10}$$

where ω_{sr}, ω_{ss} are the hour angles of sunrise and sunset, respectively.

Solar photovoltaic modules are not installed completely horizontally, but at a certain angle of interest to increase the amount of irradiance intercepted by the solar modules. While fixed solar modules are installed at an angle equal to the latitude of the location, solar modules installed in the vehicles will posses a unique and new challenges that the modules are likely to face in all possible directions. In addition to this, only the irradiance data on the horizontal surfaces are available and, as discussed above, the amount of irradiance that reaches the module surfaces for a given time and location depends on the orientation and the slope of the surface. Because of this, there is a need of converting the measured horizontal irradiance data into effective irradiance data on the tilted surface. For the beam irradiance, this can be achieved using equation 4.11, where R_b is the ratio that correlates the beam irradiance on the tilted surface, $G_{b,t}$, to that on the horizontal surface, G_b. It is a function that depends on the transmittance of the atmosphere, which in turn depends on atmospheric conditions such as the presence of clouds, water vapor, and particle concentration.

$$R_b = \frac{G_{b,T}}{G_b} = \frac{\cos\theta}{\cos\theta_z} \tag{4.11}$$

In order to determine the amount of radiation that enters the atmosphere, it is important to know in advance the amount of extraterrestrial radiation on a horizontal plane that falls on the planet Earth. At each given hour of the day, it is possible to express the amount of extraterrestrial irradiance using the following expression.

$$G_0 = G_{o,n}\cos\theta_z = G_{SC}\left[1 + 0.033\cos(\frac{360d_n}{365})\right](\sin\delta\sin\phi + \cos\delta\cos\phi\cos\omega) \tag{4.12}$$

4.4 Models to Compute Global Irradiance on a Tilted Panel

Up to this point, only the geometry of the beam radiation has been discussed. However, both the beam and the diffused radiation need to be addressed properly. The diffused component is much harder to determine than the beam component, since its distribution is highly dependent on the clearness and cloudiness of the atmosphere, which are highly variable [31]. In addition to this, one has to take into account the reflected component, which is a fraction of radiation that is reflected from the ground surface

or other surrounding objects, such as trees, buildings, or terrain, which is strongly dependent on the reflectivity of the objects, also called albedo. Thus the total solar irradiance on a tilted surface is the sum of the beam, diffused and reflected irradiance. The diffuse radiation can be divided into 3 different types of radiation, as shown in equation 4.4, namely the isotropic radiation, the intensity of diffuse radiation is uniformly distributed over the entire sky dome, that is, independent of the direction of propagation, circumsolar diffuse, described by the radiation emanating from the circumsolar region resulting from the forward scattering of radiation, and the horizon brightening diffuse, which is the radiation that is most pronounced in clear skies and near the horizon [31].

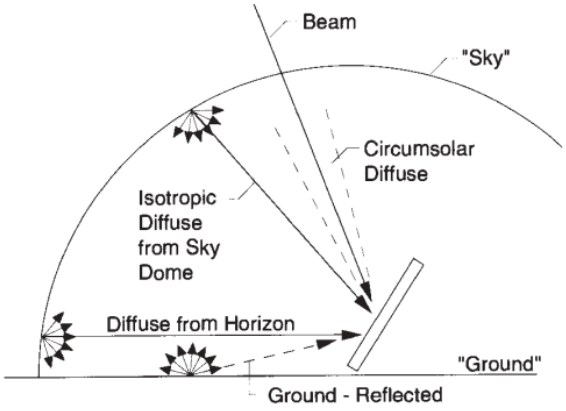

Figure 4.4: Solar radiation components striking the ground and the solar panels [36].

In an attempt of converting the total solar radiation on a horizontal surface to that on a tilted surface, several models have been proposed and used for decades. These models are usually divided into isotropic and anisotropic sky models. The isotropic sky models as the simplest model relies on the assumption that all the diffuse radiation varies uniformly distributed over the entire sky dome and that reflected radiation is also diffuse. Because of this model tends to underestimate the total irradiance values and is not commonly used in the solar photovoltaic modeling. As a result, the model used in this thesis is the anisotropic sky models. Contrary to its isotropic counterparts, these models assume that diffuse radiation is divided into 3 types of radiation as described previously. For this reason, this model is known as improvements for the isotropic models. The most widely used anisotropic models include the Klucher, the Hay and Davies, the Hay-Davis-Klucher-Reindl (HDKR) and the Perez models. Of these models, the Perez model is implemented in this thesis mainly because of its proven accuracy and is used in most engineering applications. The total irradiance on a tilted surface is given by the following equation.

$$G_T = G_{h,b}R_b + G_{h,d}\left[(1-F_1)\left(\frac{1+\cos(\beta)}{2}\right) + F_1\frac{a}{b} + F_2\sin(\beta)\right] + G_h\rho_g\left(\frac{1-\cos(\beta)}{2}\right) \tag{4.13}$$

where, $\mathrm{G_{h,b}}$ is the beam irradiance on a horizontal surface, $\mathrm{G_{h,d}}$ the diffuse horizontal irradiance, $\mathrm{G_h}$ is the global horizontal irradiance, F_1 and F_2 correspond to the circumsolar and horizon brightening coefficients, respectively, a and b are factors that correspond to circumsolar radiation for the angle of

incidence and are given as $a = \max(0, \cos\theta)$, $b = \max(\cos 85°, \cos\theta_z)$ and ρ is the reflectance coefficient of the ground (albedo). The factors F_1 and F_2 are functions of the three parameters that describe the conditions of the sky, which are the clearness index ε, the zenith angle θ_z, and a brightness parameter Δ. The clearness parameter depends on the diffuse irradiance of the hour $G_{h,d}$ and the beam irradiance at normal incidence $G_{bn} = G_{h,b}/\cos\theta_z$ and is given by the following equation.

$$\varepsilon = \frac{\frac{G_{h,d}+G_{bn}}{G_{h,d}} + 5.353 \times 10^{-6}\theta_z^3}{1 + 5.353 \times 10^{-6}\theta_z^3} \tag{4.14}$$

where θ_z is given in degrees. The brightness parameter is a function of the absolute air mass, m_{air} and G_{on}, the extraterrestrial radiation in the direction normal to the radiation computed through equation 4.1, such that

$$\Delta = \rho_m \frac{G_{h,d}}{G_{on}} \tag{4.15}$$

Table 4.1: Perez model coefficients for various values of clearness ε. Adapted from Perez et. 1990 [37].

Range of ε	**f_{11}**	**f_{12}**	**f_{13}**	**f_{21}**	**f_{22}**	**f_{23}**
1.000 - 1.065	-0.008	0.588	-0.062	-0.060	0.072	-0.022
1.065 - 1.230	0.130	0.683	- 0.151	-0.019	0.066	- 0.029
1.230 - 1.500	0.330	0.487	- 0.221	0.055	-0.0644	-0.026
1.500 - 1.950	0.568	0.187	- 0.295	0.109	-0.152	0.014
1.950 - 2.800	0.873	-0.392	0.362	0.226	-0.462	0.001
2.800 - 4.500	1.132	-1.237	- 0.412	0.288	-0.823	0.056
4.500 - 6.200	1.060	-1.600	- 0.359	0.264	-1.127	0.131
6.200 - ∞	0.678	-0.327	-0.250	0.156	-1.377	0.251

Finally, the parameters F_1 and F_2 are functions of the a set of f's coefficients derived based on a statistical analysis of experimental data for range of values of ε from different locations as shown in table 4.1. These coefficients may be calculated accordingly to equations 4.16 and 4.17, respectively.

$$F_1 = \max\left[0, \left(f_{11} + f_{12}\Delta + \frac{\pi\theta_z}{180} f_{13}\right)\right] \tag{4.16}$$

$$F_2 = \left(f_{21} + f_{22}\Delta + \frac{\pi\theta_z}{180} f_{23}\right) \tag{4.17}$$

4.5 Clearness Indexes

In order to make predictions, the distribution of beam and diffused radiation must be known beforehand. Over the past decades, several researchers has been done in an attempt to correlate the fraction of diffused radiation (G_d/G) with the clearness index (k_T) based on the available measured data, which is the ratio between the total incident radiation on the horizontal surface, G, and the extraterrestrial radiation , G_0. The clearness index represents the effect of the atmosphere and is a parameter that varies

depending on the day of the year. It can be determined by $k_T = G/G_0$. In this work, we used the Erbs et al. correlation, where they have derived their data from the US and Australian stations and is given by:

$$\frac{G_d}{G_0} = \begin{cases} 1.0 - 0.09 \times k_T, & \mathrm{k_T} \leq 0.22 \\ 0.9511 - 0.1604 \times k_T + 4.388 \times k_T^2 - 16.638 \times k_T^3 + 12.336 \times k_T^4, & 0.22 < \mathrm{k_T} \geq 0.80 \\ 0.165, & k_T > 0.80 \end{cases} \tag{4.18}$$

4.6 Photovoltaic System

In this section an overview of the physics behind a photovoltaic-based system is presented. First, we describe the working principle of a solar cell and its working characteristics, with a special attention in the solar module used in the present thesis. Then, the effect of the atmospheric variables that commonly affecting the PV modules performance is presented. Finally, an experimental procedure for measuring the PV module performance is presented, and the results obtained are discussed later.

4.6.1 The Photovoltaic Cell: Working Principle

Solar cells are electronic devices made of semiconducting materials that convert incident solar radiation near the visible range spectrum directly into electricity through the photovoltaic effect. The photovoltaic effect was first observed in 1839 by Edmond Becquerel when doing experiments with wet cells, and he discovered that the voltage of cells increased when the cell was exposed to sunlight [38].

Solar cells are composed of two thin semiconductor layers with different concentrations - the p-type material which has an excess of positive charge and an n-type which has an excess of electrons. When these two layers are joined together a p-n junction is formed, which creates an internal electric field near the junction as the electrons migrate from the n region to fill the holes available in the p region. When sunlight in the form of photons reaches the material with an energy greater than the band gap of the semiconductor, the electrons absorb the energy from the photons, which causes them to break their bonds and circulate in the material. The movement of electrons creates two charge carriers as the electron-hole pairs. Because of the presence of the electric field in the p-n region, these charge carriers are swept apart and an electric current is generated which is proportional to the intensity of the solar radiation hitting the cell. A schematic representation of a typical solar cell can be seen in Figure 4.5.

4.6.2 Current-Voltage Characteristic

The representation of the photovoltaic module is typically derived through mathematical models. The most widely adopted model to represent a cell or module is the one-diode model, also known as the 5-parameter model, although in this work all the parameters used were taken directly from the solar module data sheet specification provided by the manufacturer, so interest reader should refer to [39] for deeper understanding.

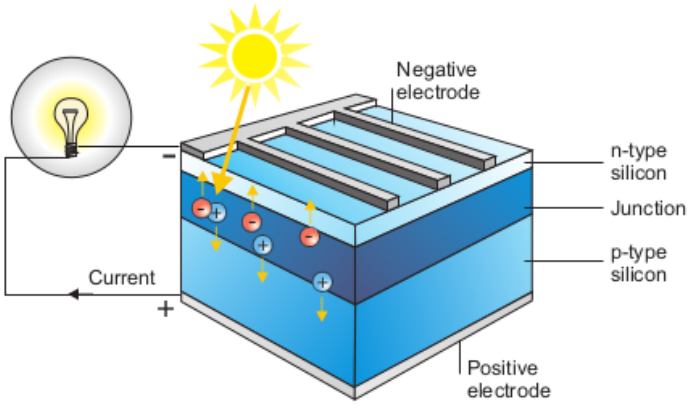

Figure 4.5: Working principle of a typical solar cell. Sunlight hits the solar cell with an energy greater than the silicon band gap ($E_{sun} > E_{gap} = 3.2\ eV$) and an electron-hole pair is created which when a circuit is made an electric current is created proportional to the light intensity [39].

The I - V characteristic curve represents the basic principle of electrical characterization measurement, taking into account the relationship between the current-voltage and the existing conditions of solar irradiance and temperature. To determine the efficiency and the output performance it is necessary to know the I-V curve. An example of the I-V and P-V characteristics curve of a typical silicon solar cell can be seen in Figure 4.6. From it, all possible working points of a solar cell can be derived.

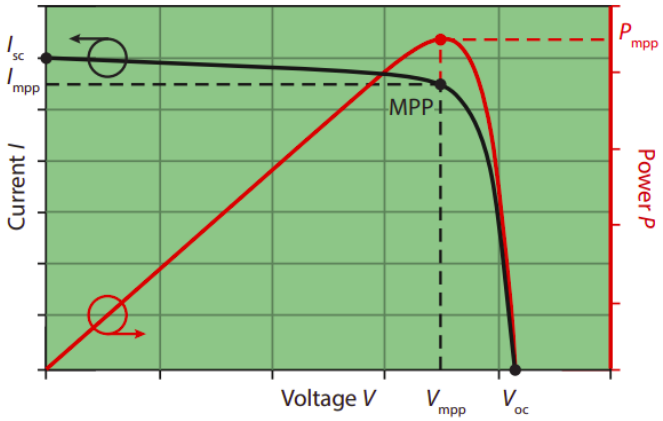

Figure 4.6: A generic I-V characteristic curve in black and the associated P-V curve in red. The maximum power point (MPP) is also indicated [34].

The short circuit current (I_{SC}) and the open circuit voltage (V_{OC}) are obtained. The I_{SC} is the current across the cell when the cell is short-circuited, that is, the largest current drawn by the cell and V_{OC} is the voltage across the cell when the cell is open-circuited, in other words, t is the maximum voltage available on the cell when no current flows through it. Between these points (I_{SC}, V_{OC}), there is a working point when the power produced by the cell is the highest, and this point is called the maximum power point (P_{max}). It corresponds to the ideal operation of the cell. P_{max} is obtained by multiplying the maximum current and voltage of the cell ($P_{max} = I_{mpp} \times V_{mpp}$).

The maximum power conversion of a typical silicon solar cell is around 16% with the maximum efficiency being reached at 20%. Since the maximum power produced is usually between 1 W and 3 W,

it is rare for an application in which a single solar cell is of use. Because of this, solar cells are connected in series or/and in parallel in order to obtain the desired voltage and current levels. When connecting the cells in series, the voltage level is added up, whereas if they are connected in parallel, the current is increased and the final product is called solar modules.

Similarly, when connecting solar modules in series, a string is obtained. When various strings are connected in parallel, a photovoltaic system is obtained. A photovoltaic panel corresponds to a set of formed by one or more modules. For example, in the case of the system implemented in this thesis, three modules rated for 29.8 V and 7.4 A under standard test conditions (STC) were connected in series, so the total voltage of the system system is equal to ($V_{tot} = V_1 + V_2 + V_3 = 89.4V$) while the current remains almost unchanged.

4.6.3 Factors Influence Photovoltaic Production

The performance of photovoltaic (PV) modules is typically tested under Standard Test Conditions (STC), which is an industry-wide standard that defines the nominal or rated power for a given module. STC is defined as being an irradiance of 1000 W/m^2, an ambient temperature of 25° C, and an air mass of 1.5 (AM 1.5) spectrum. However, these conditions generally do not represent the real working conditions of the photovoltaic module because of changes in ambient temperature, solar irradiance, and wind speed [40], which causes the module efficiency to reduce drastically. Therefore, it is necessary to analyze the influence of the external factors in order to make decisions on the system performance.

Temperature Effect on PV Solar Module Performance

The module temperature is a parameter that has a significant influence on the module performance. In fact, a high level of irradiance and/or ambient temperature causes the module temperature to rise well above the ambient temperature, which consequently tends to reduce its efficiency. This is because the voltage of the cell significantly decreases with increasing cell temperature and consequently the output power of the cell decreases at the same magnitude. This effect is best seen by looking at Figure 4.7, where a typical plot of the I-V curve is shown for different temperature levels. It is evident that there is a considerable voltage drop as the temperature of the cell increases but the current undergoes only a very small rise which does not compensate for the losses caused by the voltage drop, which is in line with what has been mentioned previously.

The most commonly used procedure for determining cell temperature consists of using the Nominal Operating Cell Temperature (NOCT) whose parameters are provided by a Standard Reference Environment (SRE) defined as module temperature based on the total irradiance level (G_{NOCT}) of 800 W/m^2, ambient temperature ($T_{a,NOCT}$) of 20°C, external wind velocity of 1 m/s and nil-electrical charge [40]. NOCT is usually given the by solar module manufacturer.

Under these conditions, the module temperature is assumed to be a function of the irradiance level and the ambient temperature. When the ambient temperature is known, the module's temperature can be determined according to equation 4.19.

$$T_{mod} = T_{amb} + \frac{(T_{NOCT} - T_{a,NOCT})}{G_{NOCT}} \cdot G_T := T_{amb} + K_t \cdot G_T \tag{4.19}$$

where T_{mod} is the module temperature, T_{amb} is the ambient temperature and G_T is the total incident irradiance in W/m^2. In the worst-case scenario where NOCT is not provided by the manufacturer, the second equation may be used, where $K_t(°C/W \cdot m^{-2})$ corresponds to the module's thermal coefficient and a constant value of 0.03 is adopted. To have a mean of comparison, the NOCT concerning the module used in this work is 46°, which corresponds to a K_t of 0.0325 $°C/W \cdot m^{-2}$.

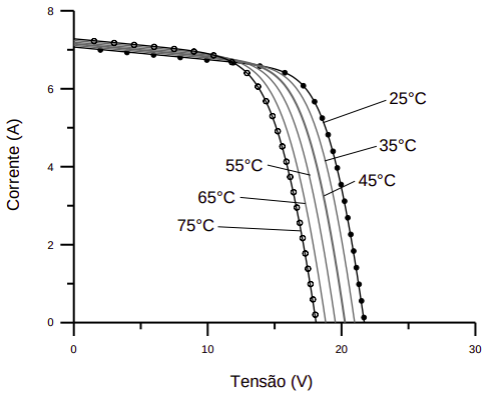

Figure 4.7: Effect caused by cell temperature variation on the characteristic curve I - V for a 36-cell crystalline silicon photovoltaic module under irradiance of 1000 W/m^2 [41].

Shading Effect and Dirt Deposition

Another factor that contributes significantly to the reduction in the efficiency of photovoltaic modules is the shading effect. It is caused by buildings, trees, birds, partial shedding, falling leaves, or any other object.

As mentioned previously, a photovoltaic module consists of several cells in series, so if one of them is shaded, the current of this cell will decrease and affect the current of the remaining cells and thus the output power of the module will drastically lower. As a way to prevent this effect, the modules are normally protected with bypass diodes, which technically allows this effect to be neglected and for the rest of the cell to function accordingly. However, in addition to the fact that the diode itself will need to use power to operate (adding losses to the system), fitting such a diode in each cell is rather expensive, so they are distributed across groups of modules (typically 16-24 cells). Similarly, if a module is shaded, all the module that is connected in series will see their performance decrease. A recent study has shown that at 300 W/m^2 irradiation levels, the output power drops to 6.4, 3.77, and 2.15 W for 25, 50, and 75% shading conditions, respectively, compared to 12.27 W for no shading [42].

The performance of photovoltaic modules is also greatly affected by the deposition of dust particles on them, as it will block part of the radiation received by the module. This deposition is highly dependent on meteorological conditions and the environment, such as the inclination, orientation of the module, wind speed, and also humidity [41].

Efficiency estimation

Given all the factors mentioned above that affect module performance, it is important to estimate module efficiency. The efficiency of a photovoltaic module is a parameter that indicates how efficient the process of converting sunlight into electricity is for the solar cell. It can be determined by the following equation.

$$\eta_{mod} = \frac{P_{max}}{A_{act} \cdot G_T} \tag{4.20}$$

where P_{max} is the maximum power output of the module, A_{act} is the total active area of the module, and G_T is the total irradiance that comes from it. For calculating the maximum electrical power output of PV, the following linear model is given by [43, 44]. Then the module efficiency can be rewritten as follows, where β_T is the temperature coefficient, which is a property of the crystalline silicon module given by the manufacturer.

$$P_{max} = P_{max@NOCT} \cdot [1 - \beta_T(T_{mod} - T_{NOCT})] \ \frac{G_T}{G_{NOCT}} \tag{4.21}$$

$$\eta_{mod} = \eta_{@NOCT} \cdot [1 - \beta_T(T_{mod} - T_{amb})] \tag{4.22}$$

4.6.4 Experimental Set-up

This section aims at analyzing the effect of temperature on the photovoltaic module working under varying environmental conditions. The experimental setup is shown in Figure 4.8. The setup consists of 3 photovoltaic modules connected in series. The modules have the job for converting the sunlight into electrical energy and then feds that energy to the vehicle setup. As the experiment was carried out with the vehicle at rest, the energy harvested by the photovoltaic modules is stored in the batteries.

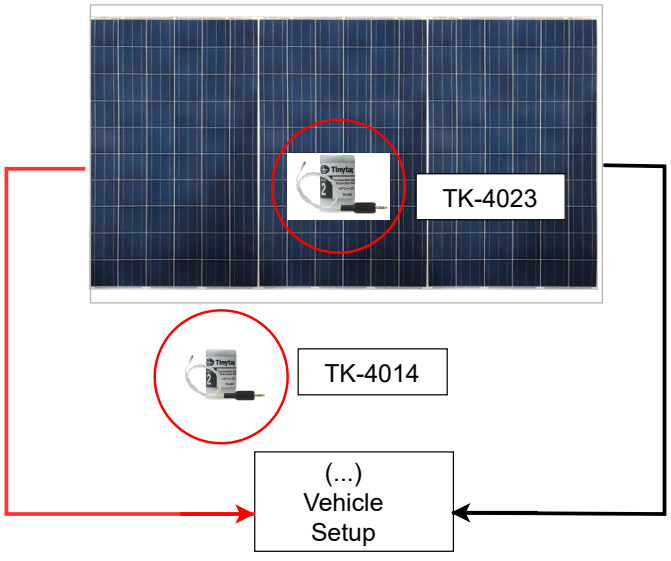

Figure 4.8: Experimental Setup for measuring the modules temperature. TK-4023 sensor measures the temperature of the modules and TK-4014 sensor measures the ambient temperature. The experimental procedure was held with the vehicle at rest at the Instituto Superior Tecnico.

To measure and monitor the module temperature, two temperature sensors were used. The Tinytag TK-4023 temperature logger was used to measure the module temperature and it was fixed to the panel using a thermal glue to avoid air bubbles that isolate the contact between the two surfaces [45]. And another sensor (Tk-4014 [46]) to measure the ambient temperature placed inside the vehicle. Both the sensors come with an internal temperature probe, which allows for fast response monitoring, particularly in hard-to-reach areas. The sensor can record temperatures from -40 to $+85^{\circ}$ C, a range that is more than suitable for typical module temperatures, and has an accuracy of 0.4°C. All data were collected and recorded every 30 seconds during 24 hours of the day. However, only data recorded between sunrise and sunset are used.

The result of the measured data can be seen in Figure 4.9(a). Analyzing the figure, it is possible to conclude that the zones of higher temperature are around 12 h - 14 h, zones where the production of solar panels are the highest. It can also be noted that there are considerable fluctuations in the temperature measurement; this is due to the shadows that are facing the panel. One important note is that the panels shows a significant drop at 16:20h. One possible reason for this to occur is due to the shadows since the vehicle was at rest.

The Performance of this solar module was then analyzed. The efficiency of the module was calculated according to equation 4.22 and is shown in Figure 4.9(b). By observing the graph, one can immediately see the effect of temperature on the performance of the module, i.e., the cell temperature rise well above the ambient temperature, the efficiency of the module tends to decreases due to the low power generated. It was also calculated the relative error relatively to the expected maximum efficiency under STC, as can be seen in the figure (y-3 axis, green curve).

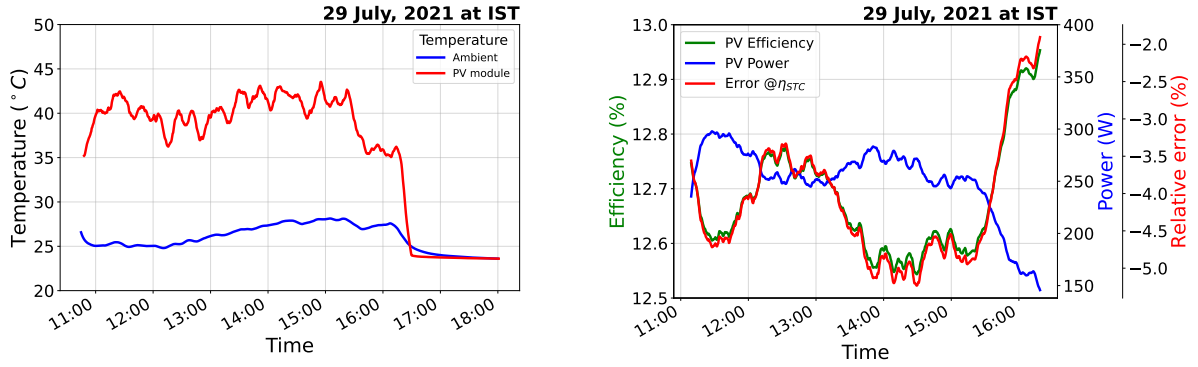

Figure 4.9: (a) PV module and air ambient temperature. (b)PV module efficiency over the day. The data presented in the graph are averaged using a 20 point moving window to create a precise profile at 10 min.

Chapter 5

Solar Powered Hybrid Rickshaw

The goal of this chapter is twofold: first, to explain how the original electric rickshaw (E—rickshaw) was converted into solar-powered hybrid rickshaw (S—rickshaw); second, to describe the on-board setup used to collect the data during the vehicle motion. In order to do that, this chapter is divided into 3 main sections. The first section accesses the benefits of the proposed S—rickshaw, with the objective of determining if the future proposed concept is warranted in terms of economic savings. In the second section there is a general description of all the experimental work done in this Master's Thesis. It starts by providing some general properties concerning the E—rickshaw used (section 5.2).

The third section is focused on the design of the S—rickshaw and describes how the solar panels were mounted onto the vehicle's roof. In this section are also provided the mechanical drawings of the supporting structures used in the vehicle (section 5.3.3). Finally, the last section details the Data Acquisition System developed and describes it from the software built and hardware used standpoint.

5.1 Sizing and Case Study

The first obvious step for the design of a solar vehicle should be the preliminary study of the amount of solar energy available in the region where the vehicle usually operate in order to quantify the system-level benefits of the proposed system. Regarding solar radiation, analyzing the solar radiation map provided by *Atlas software*, which is a free online application that provides information regarding solar resources all over the globe [47], it is possible to verify that Lisbon has an enormous solar potential that makes it suitable for the implementation of solar energy projects. The annual daily average of Global horizontal Irradiation (GHI) is about 4.72 $\mathrm{kWh/m^2/day}$ and the annual daily average of Direct Normal Irradiation (DNI) is 5.22 $\mathrm{kWh/m^2/day}$. To access the potential of solar energy, two different neighborhoods were selected, which represent the two common Lisbon regions that the vehicle will operate. The first district chosen was **Alfama** and the second was **Belém**, whose geographical coordinates can be seen in Table 5.1.

The model was developed by implementing the equations described in chapter 4 through a python script. In order to proceed with the model, high-quality weather data is required. For this purpose, meteorological data from the Joint Research Center's (JRC) online tool PVGIS, the Photovoltaic Geographical

Table 5.1: Surface parameters for the validation of the annual incident solar irradiance estimation at any given tilt surface.

	Alfama	**Belém**
Latitude (ϕ)	38° 42′ N	38° 46′ 05″ N
Longitude (λ)	9° 12′ W	9° 05′ 38″ W
Tilt angle (β)	$[0°, 15°]$	-
Surface azimuth angle (γ)	$0°$	-
Albedo (ρ_g)	0.25	-

Information System is used. PVGIS gets its data coming from a satellite SARAH, the Surface Solar Radiation Dataset-Heliot [48], which has a resolution of 5.6 km and is given in hour-time intervals. Global Horizontal Irradiance (G_h), Normal Horizontal Irradiance (G_{bn}), Diffuse Horizontal Irradiance (G_d), and air ambient Temperature (T_{amb}) are obtained for the years from 2015 to 2020. The model then estimates the annual irradiance on a given tilted surface for the two already described districts and those oriented due to the south. The other parameters used can be seen in Table 5.1. A 660 W_p solar panel array was modeled using 3 modules of *SunModule* rated for 220 W_p referenced for STC. The modules are connected in series making up 471 W_p of total peak power under NOCT conditions (see appendix B).

Figure 5.1 shows the hourly output power of the PV panels system over one-year period estimated using equation 4.21 . By looking at these graphs, it is possible to get that the output power is highly variable over the year as expected; the highest being close to 638.66 W and 640.00 W for Alfama and Belém in summer, respectively, and in winter months being 51.08 W and 52.17 W for the same districts, respectively. However, when we average the annual power over 24 hour period, we obtain the average 24-hour photovoltaic profile for each month of the year as shown in Figure 5.2. Analyzing those graphs, two important observations can be drawn: (i) the average daily power ranges between 593.3 W in July and 205.8 W in December for Belém and 592.6 W in July and 200.0 W in December for Alfama, indicating that the photovoltaic power generates 87% of its rated power in the sunniest month; and (ii) the solar panels generation is restricted to only 9 - 10 of sun hours in the winter months while it is 15 hours in the summer. Monthly photovoltaic panels average temperature is also estimated for each month of the year and is shown in Figure 5.3. The values present in the graphs represent the average daily temperature profile of each respective month.

Simulation Results

Given the small space available in the vehicle for the installation of larger photovoltaic panels, possible potential benefits that this system may offer are the range extension and the reduced charging costs.

The potential value of this system is complex to estimate, given the solar panels' ever-changing exposure to the sun owing to the random nature of the solar radiation, which is time location-specific but also due to the environmental factors such as partial shadings. To estimate the daily range extension over the year, it is considered that the output power generated by the solar panels varies with the varying temperature so that an upper bound of the driving range ($\mathrm{D}_{\mathrm{max}}$) may be obtained. Nevertheless, the general formula to calculate the driving range is shown in equation 5.1, where $\mathrm{E}_{\mathrm{solar}}$ is the total daily solar

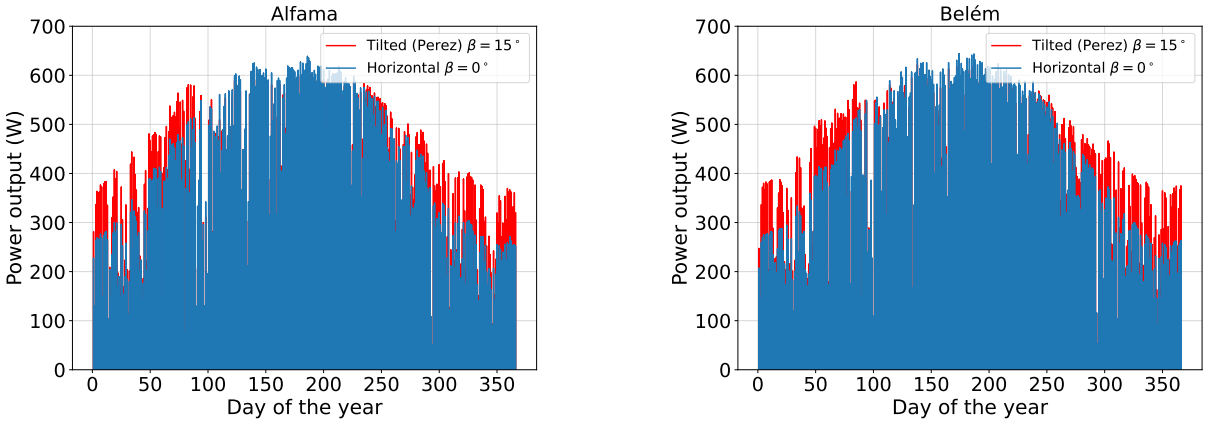

(a) Alfama (b) Belém

Figure 5.1: Annual output power estimate on the horizontal surface, G_h and on the tilt surface, G_T for $\beta = 15°$ of 2020.

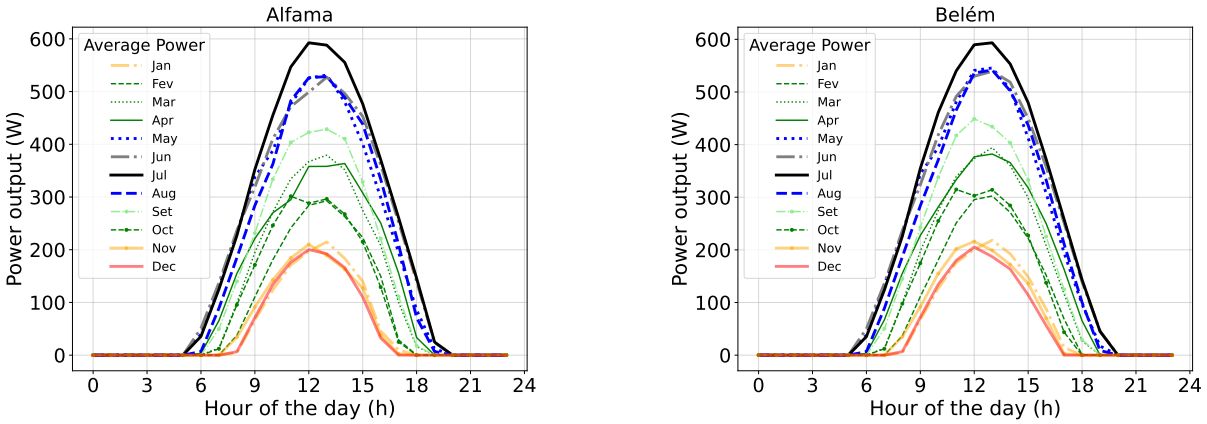

(a) Alfama (b) Belém

Figure 5.2: Average power output of 660 W PV system as a function of time of the day for different months of 2020.

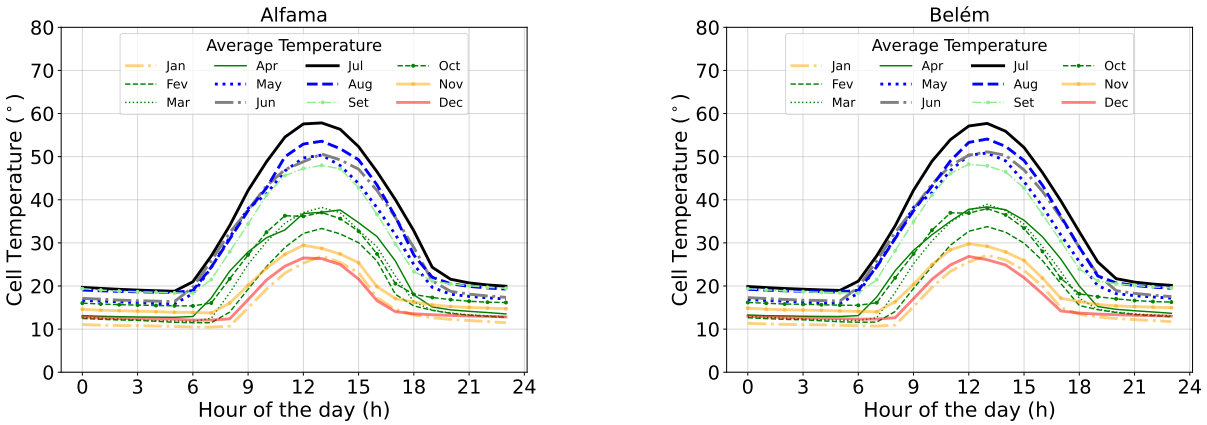

(a) Alfama (b) Belém

Figure 5.3: Estimated photovoltaic panels temperature of 660 W PV system as a function of time of the day for each month of the 2020.

energy available to the electric vehicle battery each day and $\mathrm{E}_{\text{EV,non-solarEV}}$ is the energy consumption of the vehicle if the vehicle has no solar panels installed, expressed in terms of kWh/100 km, which for the case of the rickshaw studied is 13.8 kWh/100 km (as will be seen in table 5.3). Figures 5.4(a) and 5.4(b) present the expected solar range extension over a year and the average one for each month of year, respectively. By looking at the first graph we can immediately observe the seasonal variation in the solar panels' output. The solar range extension has a variation between 36 km/day and 5 km/day for a specific day in July and December in Alfama, respectively, and variation between 33 km/day and 2 km/day in Belem. We can also observe that even in summer, there are cloudy days with a low daily solar range below the 10 km/day mark and in sunny days in winter with a range greater than 15 km/day for both the districts.

$$D_{\text{max}}\ \left[\frac{\text{km}}{\text{day}}\right] = \frac{E_{\text{solar}}\ \left[\frac{\text{kWh}}{\text{day}}\right]}{\mathrm{E}_{\text{EV,non-solarEV}}\ \left[\frac{\text{kWh}}{100\ \text{km}}\right]} \times 100. \tag{5.1}$$

Regarding the second graph, we get that for the case of Alfama: the average daily solar range is highest in May, June, and July owing to a significant amount of solar radiation available in these months. Looking back to the graph of solar radiation presented above (figure 5.2), we recall that more solar radiation is available in August; the solar range is lower owed to the fact that August is hotter than May, which causes the solar panels' efficiency to gets drooped, but the difference is minimal, just 3%. The same situation happens in the case of Belem. It also can be seen that, in winter days, all the months provide solar range extension of at least 8 km for both of the districts. It is worth noting that all the months of year give a range extension of at least 15 km/day, except for January, November and December for both the places. On a annual basis, the average daily solar range extension are 22 km for Alfama and 19 km for Belém with a panel mounted horizontally and 19 km for Belém and 17 km for Alfama with panel mounted on a tilted surface of 15°.

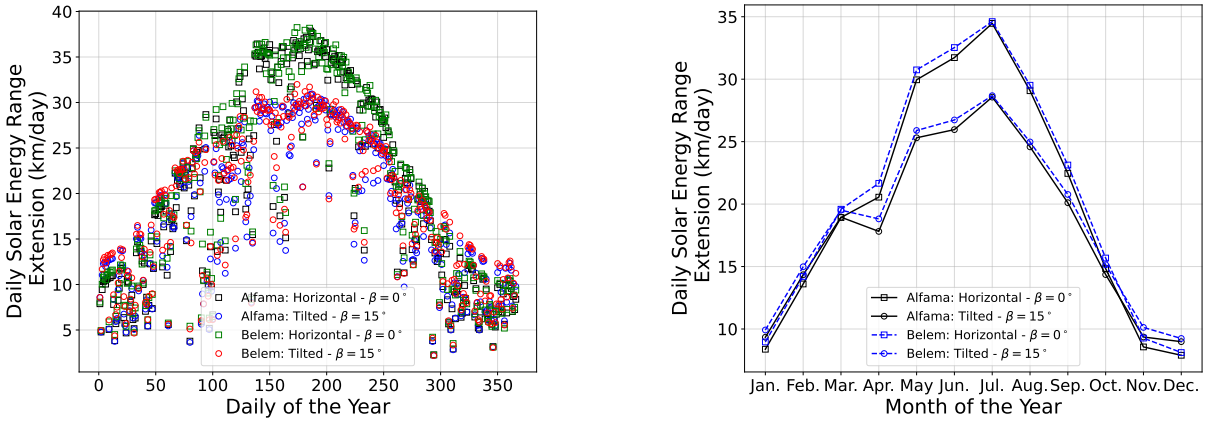

Figure 5.4: (a) Expected daily solar energy range extension provided by the 660 W_p photovoltaic system for different days of 2020 in Alfama and Belem. The vehicle's energy consumption used is $\mathrm{E}_{\text{EV, non-solarEV}}$ =13.8 kWh/100 km. (b) Average daily solar energy range extension for 660 W_p photovoltaic system for each month of 2020 for Alfama and Belém.

The second adding benefit offered by the solar vehicle is the reduction in charging costs. To access

the potential of this benefit, it was determined how much the vehicle owner could have saved since this vehicle started to operate on the road. The revenue (€) for the last 6 years can be calculated according to equation 5.2, where $\mathrm{E}_{\text{solar}}$ is the total average annual energy in kWh generated by the solar panels and C_{ele} is the €/kWh cost of electricity which varies each year. Applying this equation, the corresponding annual revenue due to the reduced dependence on the grid is represented in table 5.2. By observing this table, we can immediately conclude that with this type of technology the accumulated revenues are 1276€ and 1425€ for Belem and Alfama, respectively.

These results indicate that with this technology a significant saving in the capital investment in the vehicle is expected to be achieved. However, as stated at the beginning of this section, this analysis only represents the upper limit of the benefits provided by this system, which does not represent the real benefits in a real vehicle operation mainly due to the various environmental factors already described.

$$\text{Charging Cost} = E_{solar} \cdot C_{ele} \tag{5.2}$$

Table 5.2: Expected annual revenue provided by the 660 W_p photovoltaic system for the last 6 years for the two different district studied.

	$\beta = 0°$			$\beta = 15°$	
	E_{solar} (kWh)	Cost (€/kWh)	Revenue(€)	E_{solar} (kWh)	Revenue(€)
(Belém)					
2015	971.25	0.23	221.35	894.97	203.96
2016	961.27	0.23	216.29	881.50	198.34
2017	993.91	0.22	221.64	914.25	203.88
2018	924.72	0.22	207.70	850.97	191.13
2019	958.30	0.22	206.04	880.62	189.33
2020	961.47	0.21	203.83	882.26	187.04
Total					
	-	-	**1276.84**	-	**1173.68**
(Alfama)					
2015	1076.66	0.23	245.37	989.86	225.59
2016	1076.10	0.23	242.12	987.01	222.08
2017	1103.08	0.22	245.99	1011.89	225.65
2018	1036.78	0.22	232.86	950.15	213.40
2019	1075.03	0.22	231.13	986.57	212.11
2020	1074.24	0.21	227.74	982.76	208.34
Total					
	-	-	**1425.22**	-	**1307.18**

5.2 General Characteristics of E—rickshaw

The present work revolves around an E—rickshaw, mostly known as Tuk-Tuk in Lisbon. In particular, the rickshaw studied is the Limo GT model manufactured by Tuk-Tuk Factory (TTF), which is a Dutch company created in 2008 with the aim of being sustainable and environmentally friendly [49]. A picture of a similar rickshaw used can be seen in Figure 5.5. The technical specification of this vehicle provided by the manufacturer can be seen in Table 5.3. The vehicle has the capacity to transport up to 5 people plus the driver and is expected to have low maintenance costs.

The vehicle is capable of developing a maximum speed of 45 km/h, which makes it a powered

light vehicle as per Portuguese standards categorized as L5e [6]. The battery pack in the E-rickshaw consists of 24 $LiFePO_4$ battery cells connected in series with a capacity of 180 Ah, each cell has a nominal voltage of 3.2V [50], which in ideal condition the nominal voltage of the total battery pack should be of 76.8 V. Furthermore, a Battery Management System (BMS) was integrated on the battery pack of the vehicle in order to keep the batteries protected from the possible deep discharging and overcharging. The BMS is also capable of communicating with a mobile phone via Bluetooth through a mobile application, allowing the driver to access and monitor the battery status in real time. In the appendix A.1.1 it is possible to find all the information concerning the mobile application.

Figure 5.5: Picture of the **E—rickshaw Limo GT** used in this work for testing.

Characteristic	Value
Seat Capacity	6 seats
Measurements(L/W/H)	3.72/1.51/2.07 m
Rear tire size	155/80R13
Front tire size	145/70R12
Charger specification	10 A
Battery voltage	76.8 V
Gross weight (without PV)	829.4 kg
Payload	300 kg (max)
Energy consumption	13.8 kWh/100 km
Maximum velocity	45 km/h
Gear ratio	10:1

Table 5.3: Vehicle data for the **E—rickshaw Limo GT** as specified by the manufacturer [51]. The total mass of vehicle presented in the table is for the vehicle without including the solar panels weight.

The vehicle is equipped with a three-phase induction motor whose characteristics can be seen in Table 5.4. The operating conditions of the motor correspond to a rated power of 7 kW at an electric frequency of 104.5 Hz, the torque of the drive shaft being 21.6 Nm.

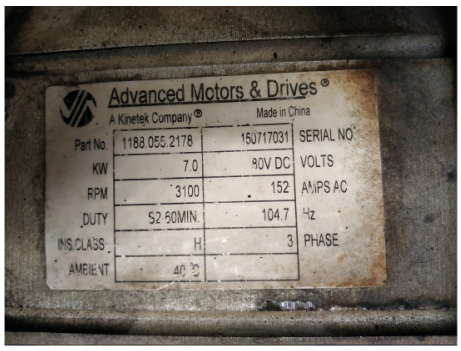

Figure 5.6: **E—rickshaw Limo GT** plate on the motor.

Name	Value
Rated power	7 kW
Phases	3
Rated velocity	3100 RPM
Motor phase	3
Electrical frequency	104.5 Hz
Current	152 A
Ambient temperature	40° C

Table 5.4: Main characteristics of the three phase motor from the **E—rickshaw Limo GT model**.

Mass Estimation

With the adding solar panels to the vehicle, the vehicle mass specification presented above is no longer valid, so a new mass estimation must be made. The solar panels that were put onto the vehicle's roof were *Sunmodule220* poly-weighting 21.2 kg each. As 3 of these were used, this meant around 60 kg extra weight with supporting structures and other related components would add to the vehicle weight. The resultant total mass of the vehicle was found to be around 900 kg without payload. In addition to this, plus 10 kg extra weight was added into the equation to account for the supporting structures used to hold the solar panels onto the vehicle's roof.

$$m = \underbrace{829.4}_{\text{vehicle mass}} + \underbrace{3 \times 21.2}_{\text{panel weight}} + \underbrace{10}_{\text{support structure weight}} = 903\ kg \tag{5.3}$$

5.3 Solar Panels Set-up

One of the major objectives of the present thesis was the construction of the S—rickshaw. Since the rickshaw was already available, this process involved designing supporting equipment to accommodate the solar panels on the existing vehicle.

In the following sections, it is first described the sizing of the system, the solar panels chosen (section 5.3.1); it is then described the supporting structures built, as well as the schematics of the solar panels and the energy meter (PZEM) connections. In the last section it is shown several mechanical drawings, including all the support structures as well as the total PV system.

5.3.1 The PV Panel Selection

The first step towards the realization of any solar car should be the sizing of the PV system, in this case the selection of the photovoltaic panels. The decision on which panel will be used will be discussed on the following paragraphs. In the market there are a lot of variants like flexible, rigid , mono-crystalline or poly-crystalline etc., with different output power and sizes that they are manufactured. The first step correspond to decide between rigid or flexible panels. In this regard it is clear that only the rigid one will fulfill the requirements and objectives of the project. This is because, currently flexible solar panels have lesser efficiencies ($\sim 7\% - 10\%$) compared to the standard rigid ones(up to 23%) [52]. Further reasons for not considering flexible solar panels are the limited space available for the installation and structural needs.

The challenge then, lied in choosing between mono-crystalline or poly-crystalline. For doing so, in the table 5.5 is shown some characteristics between these two panels. As it can be seen, poly-crystalline one have shown lower efficiencies compared to its mono-counterparts. Other factors, are that poly-crystalline are less expensive and last longer. Since the objective was to build a low-cost-based system, it was decided to chose poly-crystalline solar panels.

The solar panel chosen for this project was the *polycrystalline silicon Sunmodule Plus SW 220 poly*. The characteristic parameters under STC given by the manufacturer are tabulated in table 5.6. Given

the size of the roof of the vehicle, it was chosen to have an array of 3 panels connected in series which making up an installed total power of 660 kW_p under STC.

Table 5.5: Comparison between the **mono-crystalline** and the **poly-crystalline** solar panels.

Parameters	**Monocrystalline**	**Polycrystalline**
Cost	High	Low
Efficiency	High	Low
Lifespan	Minimum 25 years	25+ years
Temperature coeff.	High	Low

Table 5.6: Manufacturer datasheet of the chosen photovoltaic panel ($^* =$ Under STC). More information concerning the solar panels used can be found in the appendix B.

Quantity	**Value***
Cell per module	60
Total Active Module Area (A_{ct})	1.675 $\times$ 0.951m^2
Solar cell type	Poly-crystalline silicon
Peak power (P_{max})	220 Wp
Maximum Power Point voltage (V_{mpp})	29.8V
Maximum Power Point current (I_{mpp})	7.4A
Open-Circuit Voltage (V_{oc})	36.6V
Short circuit current (I_{sh})	8.0A
Module Efficiency at mpp (η_m)	13.12$\%$
Temperature Coefficient of Pmax (β_{T})	-0.45$\%$/K
Nominal Operating Cell Temperature (NOCT)	46°C

5.3.2 PV Panels Wiring

In Figure 5.7 it is shown the connections between the solar panels as well as the solar panels and the PZEM sensor. The three solar panels were connected in series so that the voltage of each module was added up, making up a maximum voltage of 89.4 V under STC. The connections between the solar panels were designed in such a way that they could be held in place without significant vibrations, especially when the vehicle is in motion at high speeds, which will be discussed in the following sections. It was also designed so that it could be easily connected to the PZEM located in the rear part of the vehicle. In Figure 5.7 it is also shown that a 10 A fuse was added between the solar panels and the battery pack in order to add safety to the vehicle and to protect the system wiring from over-current.

5.3.3 Mounting the Solar Panels to the Roof of Rickshaw

To setup the solar panels to the roof of the vehicle is a hard task, especially when the vehicle does not have a roof rack. Because of this, several supporting structures were designed in order to safely accommodate the solar panels to the roof of the vehicle.

The mounting process consists of two major steps: the first step was to design a supporting structure in order to attach the three solar panels together. To do this, two iron round tubes were used and then holes were drilled through the eyelets on the sides of the solar panels. After that, the two tubes were placed on the bottom part of the solar panels and holes were drilled that lined up with the corresponding

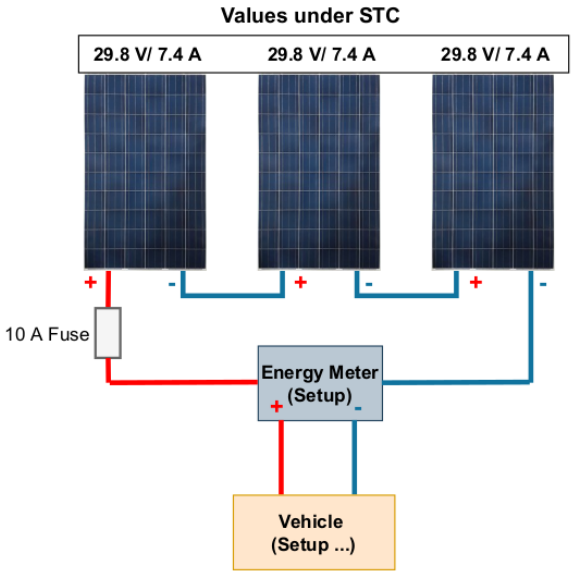

Figure 5.7: Wiring diagram between the solar panels to PZEM to the vehicle.

to those of the solar panels and using 12 bolts and nuts (4 holes per solar panel) it was possible to hold the solar panels on the tubes. The final result of this step is shown in Figure 5.8.

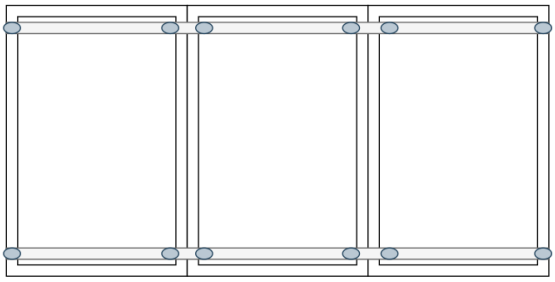

Figure 5.8: Top views of the solar panels held on the tubes. Each blue-grey points represents nuts and bolts.

The second step was to mount the system to the roof of the vehicle. Since the surface of the roof is not completely horizontal and that front part size is different from the rear one, it was added an isophonic clam to make up for this lack. Then, with the use of nuts, we were able to hold the system on the roof. The final result of the whole system can be seen in Figure 5.9.

5.4 Data Acquisition System

The focus of this section is to describe the data acquisition system used for collecting data during vehicle movement. Before going into detail, it is worth mentioning that the data acquisition system used in this work was a continuation of the previous work found in [28]. That being said, only details regarding the system implemented in this work will be provided. However, a general description of the algorithm behind it will be explained later.

Section 5.4.1 describes the set-up used to measure the power output of the solar panels. Sec-

Figure 5.9: Photo of the solar integrated electric rickshaw during data collection in Lisbon (Alameda).

tion 5.4.2 describes the software used in the acquisition, and finally, the algorithm used to access the acquisition data is provided in section 5.4.4.

5.4.1 Energy Meter Set-up

The data concerning the solar panels were collected from the *PEACE-FAIR PZEM-017 DC* Energy module (PZEM)(appendix B). This module is an electrical sensor that is used mainly to measure electrical appliances such as active power, current, DC voltage, energy consumption and is broadly used in IoT applications for controlling and monitoring smart systems because of its low cost and easy-to-use.

The PZEM used is capable of measuring current up to 300 A depending on the shunt used. As can be seen in Figure 5.10, the PZEM sensor came with an external shunt resistance rated for 50 A, which tells us that the maximum current measured should be of 50 A, and given that the photovoltaic module used, with a total maximum power current of 7.4 A, then this current measurement sensor is more than suitable for the system in question.

The PZEM exchanges its information through a built-in RS-485 interface using the Modbus RTU protocol over TTL UART at a baud rate of 9600. The other parameters taken from the data sheet provided by the manufacturer can be seen in the Table 5.7. To have full access to the information read by the sensor, a Raspberry Pi was used.

As said, communication between the PZEM and the RS-485 is achieved through the Modbus RTU protocol. In short, this protocol is based upon master-slave (request/reply) technique, where the Raspberry Pi is set as the master and the PZEM board the slave. The first realization to get data was that the master had to send a request message to the slave. To do this, in figure 5.11 is represented a schematic configuration between the Raspberry Pi and the PZEM. In addition, the connection between the shunt resistance and the PZEM board is presented. Using the configuration from the serial com-

Figure 5.10: Photo of a similar PZEM current sensor to the one used in the vehicle.

Parameter	Value
Baud-rate	9600
Parity	None
Stop Bits	2 bits
Byte size	8 bits

Table 5.7: PEACEFAIR PZEM-017 serial communication parameters taken directly from the datasheet (see appendix B.1).

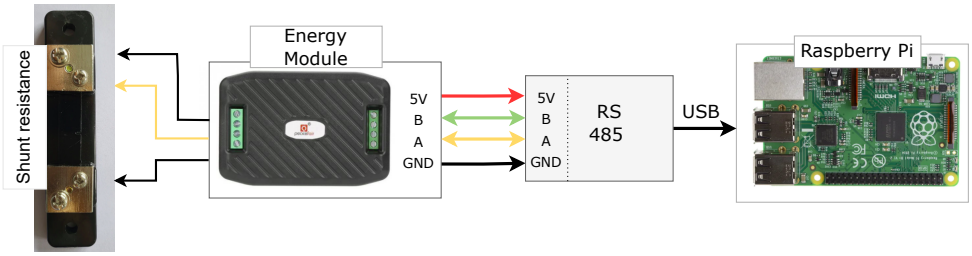

Figure 5.11: Schematic of the connection to the energy meter using for testing.

munication represented in table above it was then possible to receive all the data concerning the solar panels output.

5.4.2 Experimental Set-up

This section looks at a description of the data acquisition used to collect trip data during vehicle movement. The acquisition system shall consist of two main elements: the Raspberry Pi and the sensors (GPS receiver, BMS, and the PZEM).

At the center of the whole system is the Raspberry Pi. This device is a credit card-sized computer developed by *Raspberry Pi Foundation*. Its reduced cost to power low-smart devices makes it a popular choice for developing Internet of Things (IoT) applications, such as home automation, etc. [53]. In this particular work, the model used is the Raspberry Pi 3 Model B, which comes with input/output (IO) pins that are vital to communicating with the sensors, built-in WIFI, and Universal Serial Bus (USB), and Ethernet ports are also available. In this work the connection to the Raspberry Pi was made through the Secure Shell (SSH) client.

As said, the Raspberry Pi was responsible for getting the data from the module sensors and manipulating it into a suitable format and saving them in a folder. Both of the sensors were connected through asynchronous serial communication. However, as the Raspberry Pi used only has one UART (*PIN14 - RX* and *PIN15 - TX*), one needed at least 3 UARTs: one per sensor. Luckily, both the sensors, the GPS receiver and the PZEM communicated through a virtual suited port USB adapter; those were then connected to the USB port of the Raspberry Pi as shown in Figure 5.12. The BMS was connected through a USB adapter, as it was already in place from previous work [28]. Figure 5.12 it is shown the data acquisition system wiring, as can be seen, to provide power to the Raspberry Pi, 12 V supply is connected to the Raspberry Pi's General Purpose Input Output (GPIO), and since the Raspberry Pi withstands only power up to 5V, a DC converter is used for this need. Regarding the location of the

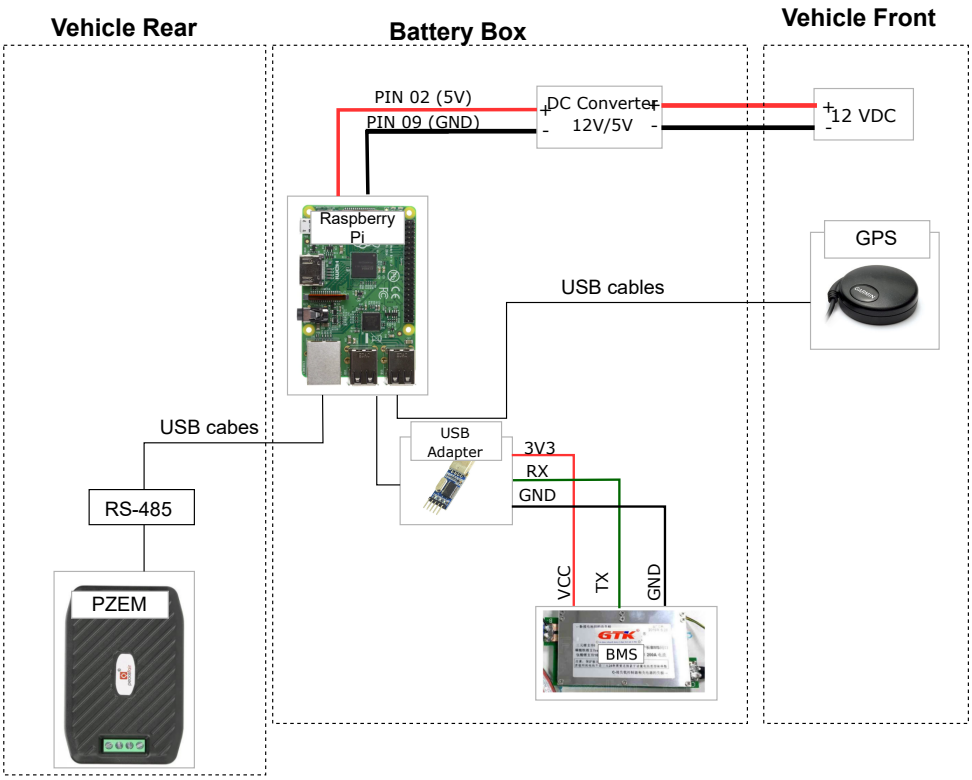

Figure 5.12: Wiring diagram for connecting the GPS receiver, BMS and PZEM sensors to the Raspberry Pi.

sensors inside the vehicle, was that the GPS receiver needed to be in the frontal part of the vehicle to have a clear view of the sky. The Raspberry Pi and BMS were grouped in the battery compartment, and lastly PZEM was placed on the rear part of the vehicle, clearly visible in figure 5.12.

5.4.3 Data Acquisition Software

As stated in section 5.4.2, 3 types of data were acquired from the three sensors mounted in the vehicle. The first corresponds to the data from the GPS receiver, which include all the necessary information regarding the vehicle's position at each instant of its movement, but also its velocity. The second data was collected from the BMS; these data provide information on the battery pack. Namely, battery voltage, power, and State of Charge (SOC). The final are the data concerning the energy generated from the solar panels mounted on the vehicle's roof, described in section 5.3. In appendix A.1, it is possible to find the description of all the information acquired from the sensors. To collect all these information, software was built in Python (version 3) under the paradigm of Object-Oriented Programming (OOP). Figure 5.13 summarizes the inheritance of the classes used, and each of these is explained in the following paragraphs.

- The class **TXThread** is responsible to send a request message to the BMS board and to read and save the information about the battery pack seen previously;
- The class **GPSThread**- this class is responsible for reading the data coming from the GPS receiver

and saving its information. For making the GPS readings, it used the GPS package. This package collects data from a GPS receiver coming from a monitor daemon GPSD. This deamon monitors and reads data constantly from the GPS receiver in a server-client fashion and is initiated at the Raspberry Pi startup that works as the transparent task of the server, i.e., without the interference of the user [54];

- The class **PZEMThread** - was built to connect to the PZEM board and read its contents. To make the PZEM readings, it uses the Modbus RTU Python package, which is based on the master-slave architecture described previously.

Figure 5.13 shows a general class called **SensorThread**. This class is responsible for the regular acquisition of the data from the three classes and saves them in a file at a constant time interval using the Multitimer package from the class threadingThread.

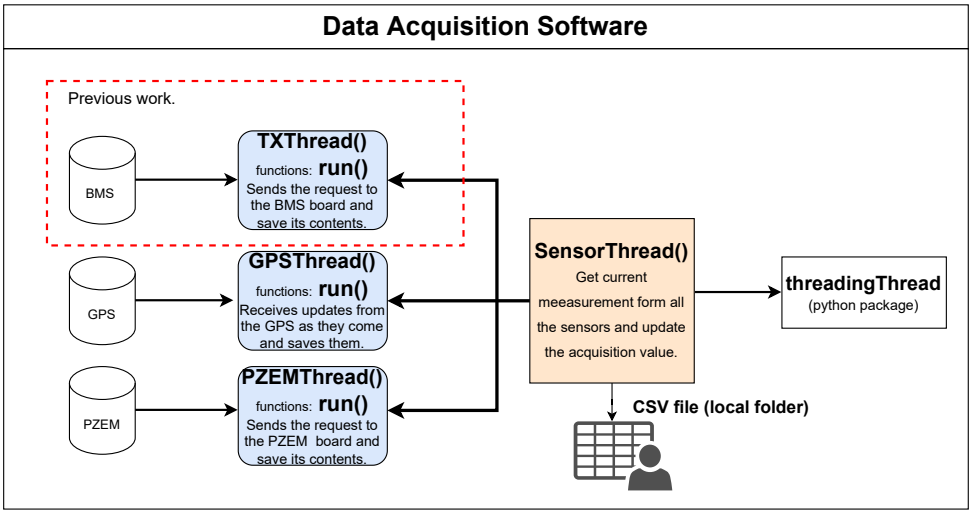

Figure 5.13: Diagram of the python classes implemented for acquiring data from the three different sensors.

5.4.4 Data Upload

As seen in the previous section, there was no other way to connect to the Raspberry Pi but connecting through SSH to have access to the data collected by each module and sensor used in the mounted system. To make up for this, the Raspberry Pi was configured to automatically upload the data to a remote server so that anyone can immediately access those data from any device and anywhere in the world. Additionally, this approach will facilitate data collection without compromising the business that owns the vehicle that will be in operation during the summer. In the following paragraph, the methodology used to tackle this problem is explained.

The selected approach for treating this problem consists of two steps: The first one corresponds to the WIFI network configuration inside the Raspberry Pi. This was simply done by creating a wireless USB connection between the Raspberry Pi and the router location. The second consists of creating an algorithm that constantly checks for the new files stored on the Raspberry Pi. Once a file has been

found, the Raspberry Pi connects to a remote server using an SFTP protocol, which stands for SSH File Transfer Protocol. The use of SFTP makes it possible to authenticate and establish connections in a secure way, ensuring the data being transmitted is encrypted all the way through the destination [55]. The algorithm is shown in figure 5.14.

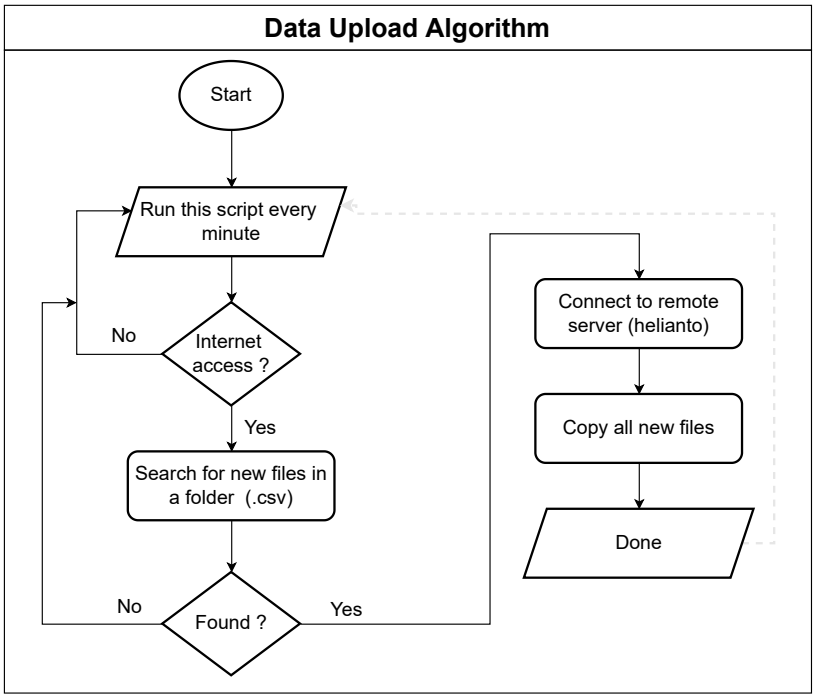

Figure 5.14: Algorithm used for uploading the trip data to the helianto server. The script ran every minute.

5.4.5 Testing Results

Once the data acquisition has been developed, the next step is to test it. To that end, an acquisition test was made at Lisbon city center on 18 August 2021.

(a) Full vehicle trajectory.

(b) Zoomed-in segment.

Figure 5.15: Vehicle positions measured of a round trip. The total distance traveled by the vehicle was approximately 46 km.

Figure 5.15(a) shows the positions of the vehicle measured. As can be seen, the recorded points

have a significant amount of errors because they do not match the road maps. This is probably due to low signal quality, mainly in urban areas, when a vehicle losses GPS coverage. This is best perceived by zooming in on the position data, as shown in the second graph (figure 5.15(b)).

In Figure 5.16 (above), it is possible to see the velocity profile as a function of the driving distance measured from the GPS receiver; it can be observed that the measured velocities are within what would be expected provided that the maximum velocity of the vehicle was 45 km/h.

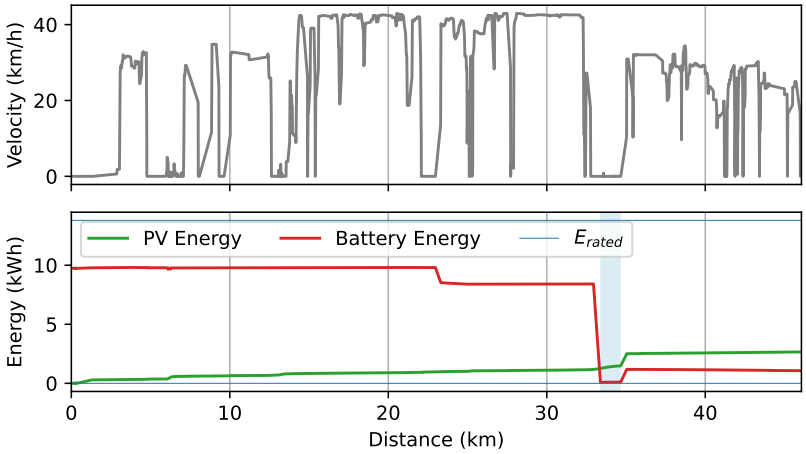

Figure 5.16: Velocity data measured during the first test of data acquisition (above) and variations of energy consumption measured by the BMS and the Energy Meter. Light blue-filled area displays parking time, which was about 3 hours (below).

In Figure 5.16(below) the variation of energy consumption in the battery (solid red line) and the energy produced by the photovoltaic array (solid green line) are plotted as a function of the distance the vehicle travels on a typical sunny day. This figure reveals how the addition of solar photovoltaic technology can actually help reduce the energy usage of the battery. In fact that day was the first day of vehicle operation since last summer, some parameters, especially on the BMS were ill-configured that resulted on the battery SOC falling to zero after driving 38 km approximately, as can be seen in the figure. Because of this, the driver has had to park the vehicle and charge the batteries and wait until a minimum battery charge of $\sim$ 1 kWh was achieved instead of towing it with the energy generated by the solar panels. After 3 hours of solar charge, the driver was able to return home due to solar energy. That is to say, here we can see the benefits of photovoltaic integrated into vehicles.

Chapter 6

Analysis of the Data Collected

The purpose of the present chapter is to analyze the quality of the raw data collected during vehicle motion. This step is important in misleading possible errors and biases that data may have; since we are working with experimental data, some inaccuracies are to be expected. For example, when the Raspberry pi was not able to read the data from the BMS/PZEM or when the GPS signal was lost because of low-quality signal mainly in urban areas.

In order to do that, section 6.1 presents an overview of some features of the data collected by means of histograms, named the velocity of vehicle, power generated out of the solar panels and stored in the batteries. The spatial distributions of the same features are presented afterward. Secondly, section 6.3 addresses the problem of poor data quality and a way of solving this problem are there presented.

Lastly, this chapter details some features derived from the data collected but that were not directly measured from it, which is important in vehicle modeling. Some of these features include road slope and total distance traveled by the vehicle.

6.1 Basic Statistics of the Data Collected

The data analyzed within this chapter and in the rest of this work was collected from **20/08/2021** to **21/02/2022**, resulting in approximately **528 km** of vehicle movement, which corresponds to an observation period of about 53 hours of vehicle usage.

This is a very limited dataset, as it corresponds only to a small portion of vehicle operating conditions. Annual data on vehicle operation should have been acquired, however, due to the time horizon of this project and the seasonal characteristics of the vehicle, such data collection was no longer possible. Our plan lied then to get the vehicle on the road as soon as possible to record data in a summer time. Therefore, in this regard, it is worth mentioning that the performance of the models implemented in this thesis have been affected owing to the insufficiency of the data collected. As a result, the author of this work would like to encourage the acquisition of much more data in future work.

Table 6.1 summarizes the basic statistics of the main features collected during the data acquisition. It shows the range of values for each feature (its minimum and maximum values) as well as its average and standard deviations values.

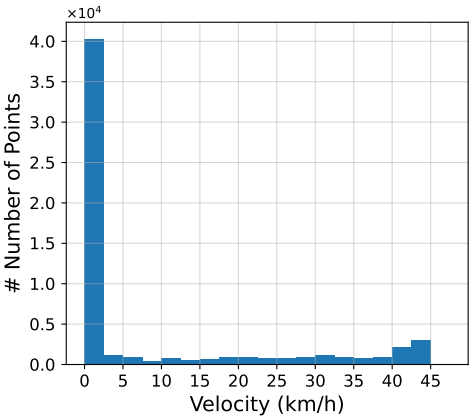

(a) Histogram of observed vehicle velocity values.

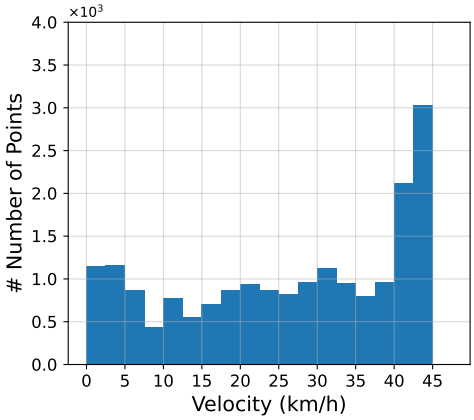

(b) Histogram of observed instantaneous vehicle velocity values. The values presented in the graph were filtered out the histogram with a threshold of 1.08 km/h.

Figure 6.1: Distribution of the measurement of the vehicle velocity for the data collected in the vehicle. Each column represents a 0.5% bin.

Table 6.1: Descriptive statistics of key features measured during data acquisition: vehicle velocity, solar panels power and voltage, battery current, voltage, power and SOC.

Features	Mean	std	Min	Max
Vehicle velocity (km/h)	9.91	15	0.0	46.85
Photovoltaic array power (W)	184	202	0.0	609.7
Photovoltaic array voltage (V)	78.88	1.45	42.96	83.03
Battery current (A)	10.81	40.13	-149	244.1
Battery voltage (V)	78.93	1.18	70	81.80
Battery power (W)	830.86	3130.94	-12121.83	19381.54
SOC (Wh)	9947.56	2114.98	0.0	12288

6.1.1 Feature Distributions

This section analyzes some of the features presented in table 6.1. As said previously, this is an important step in understanding the trend of the data. Because of this, this first part of the data analysis is done without making any data transformation other than any data pre-processing to detect some outliers or biases in the datasets.

In Figure 6.1(a) it is possible to see the histogram of the velocity data at which the vehicle is traveling. The first thing that comes to mind is that there are hundreds of points that correspond to the points where the velocity is zero or very close to zero. Because of this, a clear trend can not be seen. To better visualize the velocity pattern, points with low velocities were filtered out of the histogram, resulting in the distribution that can be seen in figure 6.1(b). Now looking at this graph we can observe that as the velocity increases there are more points to be acquired and a well-defined peak can be seen at the maximum vehicle's velocity measured ($\sim$ 45 km/h), suggesting that this is the average velocity at which the vehicle drove most of the time, indicating that, the driver always prefers to go at maximum speed available whenever the road conditions permitted.

Figure 6.2(a) it is shown the distribution of solar power produced as the vehicle travels. As we can

observe, the photovoltaic power generated is very variable because it depends on several environmental factors such as trees, buildings, shadows, etc., which significantly reduce the performance of solar panels as seen in chapter 3. This assumption can also explain why the average power has such a very low value (see Table 6.1). Another interesting feature that we can observe is a second peak at around 500 W. Most probably corresponds to the data acquired on sunny days, in which the expected generated power is much higher.

Figure 6.2(b) shows the distribution of solar voltage. As can be seen, the voltage remains almost constant, as expected.

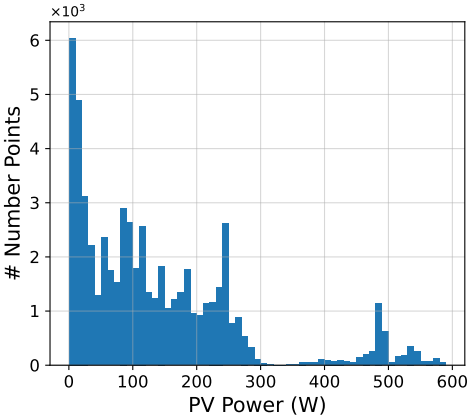

(a) Distribution of the measured photovoltaic array power.

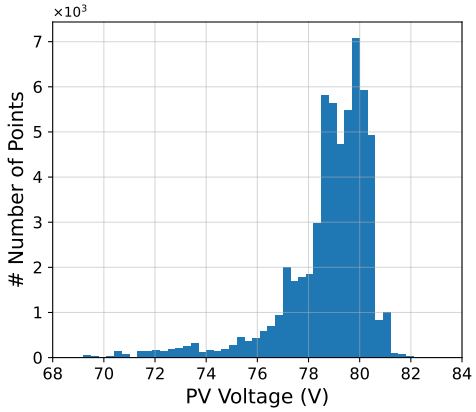

(b) Distribution of the measured photovoltaic array voltage.

Figure 6.2: Photovoltaic array power and voltage distributions measured for the vehicle movement.

6.1.2 Geographical Feature Distribution

This section intends to explore the geographical distribution of some of the main features measured during vehicle movement. That is, vehicle velocity, altitude profile, photovoltaic power production, and battery power consumption. To do so, a discrete map was built for Lisbon city with a resolution of 200 m^2, which can be translated into a measurement every 15 meters. To build these maps, the features were divided into two-dimensional bins as a function of their latitude and longitude values using *mapbox*, which is a powerful tool used for building interactive customizable maps. The values of each feature were obtained by averaging the coordinates falling inside each square of area.

However, despite having access to the altitude values measured by the GPS receiver, these values were not accurate enough to be used in the modeling. Due to this, the static altitude data was downloaded from the high-resolution digital elevation models (DEMs). How these values were obtained will be discussed further in section 6.3. Figure 6.3(a) shows the expected average values of the predicted **altitude** along the route as the vehicle travels. This corresponds to a more realistic altitude value compared to the ones measured by the GPS receiver, having been used in previous studies and revealed to be accurate enough for vehicle modeling [28].

Figure 6.3(b) shows the average measured velocity along the route that the vehicle travels at, and it can be seen that the vehicle experiences lower velocities when it travels in urban areas, which is to be

expected because there are more movements and the traffic are more intense, thus more hazards to prevent.

In Figure 6.4(a), it is possible to see the average photovoltaic power array generated for the different coordinate pairs while the vehicle is traveling. One may immediately conclude that the power generated is lower when the vehicle travels in urban areas than when traveling in rural ones. This is mainly because of the shading on the panels due to nearby buildings and/or other surrounding objects; lastly, Figure 6.4(b) shows the average battery power spent as the vehicle travels. Looking at that graph, it is possible to observe that there are a considerable number of points where the power consumption is very low. This corresponds to the regions where the altitude values are more variable as seen in figure 6.3(a) (showing a considerable amount of point with a light blue color), which is not compatible with the real vehicle power consumption. This happens because the way this map was built it does not take into consideration the direction in which the vehicle is traveling in, causing the average power to decrease drastically.

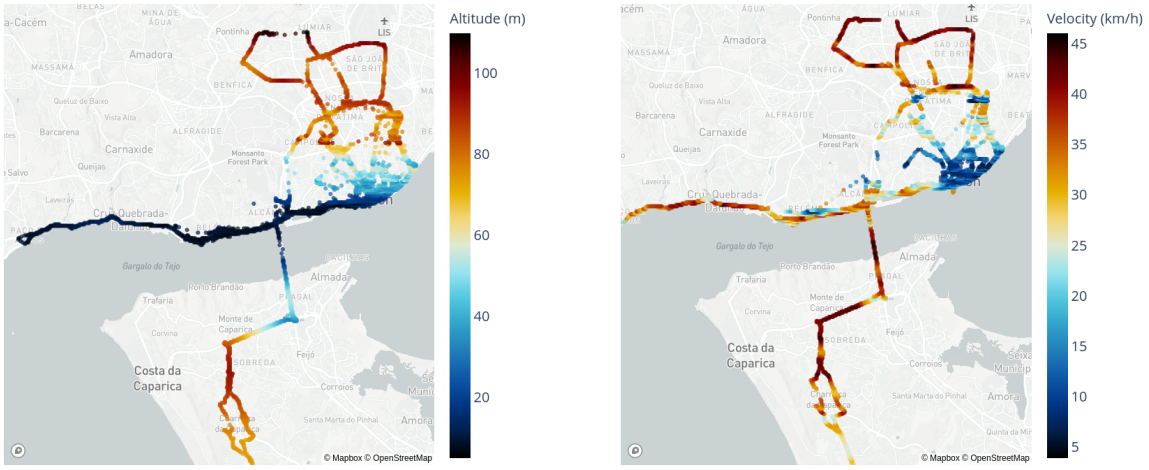

(a) Estimated altitude as a function of the coordinates measured.

(b) Average velocity measured for the different point coordinates measured.

Figure 6.3: Altitude estimated and velocity measured for different point coordinates.

6.2 Solar Range Estimation

As seen in Chapter 5.2, the autonomy of the vehicle studied provided by the manufacturer is 100 km; however, with the integration of solar panels, it is expected that the autonomy of the vehicle will slightly increase several kilometers depending on the amount of solar energy generated and provided to the vehicle. Therefore, it is necessary to estimate the new autonomy of the vehicle to provide the driver with how many kilometers the vehicle would be able to drive on a fully charged. The new expected average vehicle range can be estimated using a simple linear regression. This was made by computing the total distance traveled (Δs), during each day of the data acquisition and the corresponding energy consumed in the trip, which is the sum of energy in the batteries and the solar panels produced ($\Delta E =$

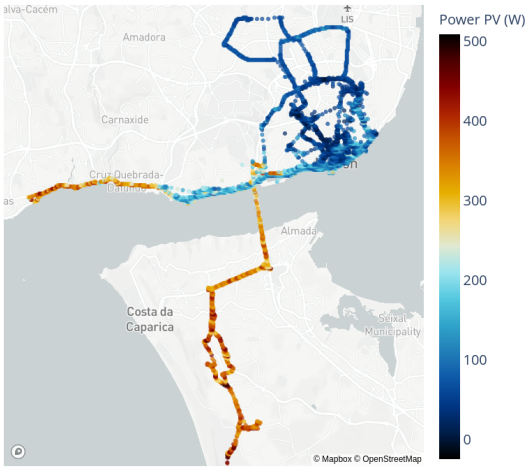

(a) Average measured PV power for the different point coordinates measured.

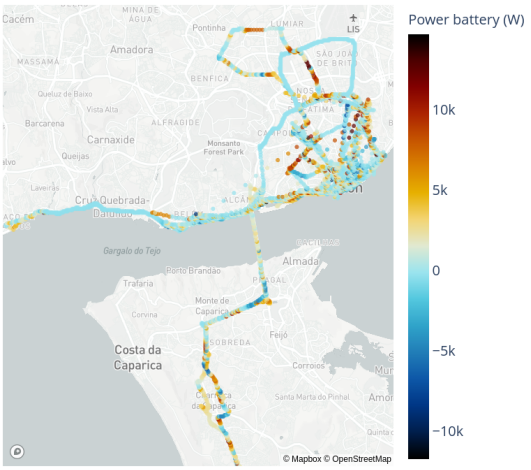

(b) Average measured battery power for different point coordinates measured.

Figure 6.4: PV array and battery power measured for different point coordinates.

$E_{batt} + E_{solar}$). The task of linear regression is to find a line that best fits the data points, i.e., that minimizes the error between the data points to the line. In this case, the model predicts the target variable (ΔE) based on a given predictor variable (Δs) by determining the coefficient that explain such relationship. The equation that explain such relationship is of the form shown in equation 6.1, where A is the slope of the line determined by the model.

$$\Delta E = A \cdot \Delta s \tag{6.1}$$

The result of the linear regression is represented in figure 6.5. The slope of the line obtained was $A = 0.090 \pm 0.011\ kWh/km$, with a R^2 value of 0.73. The average distance that the vehicle is expected to traveled for a complete battery discharge of 13.8 kWh is around 153 km, that is, with the incorporation of solar panels the vehicle range increases by 53 km relatively to the range that can be achieved without the solar panels. Nevertheless, it should be keep in mind that this is a very simplistic approach to determine the new range of the vehicle, as it only considers the amount of energy used and thus independent of the season of the year. In order to have better estimations, the data dataset needed to be much bigger than the one used in this work.

6.2.1 Battery Characterization

As stated in the objectives of this work, the major goal is to propose a suitable battery pack technology that minimizes the battery capacity in the solar rickshaw. It is essential to characterize battery usage [1] using experimental data from vehicle operation, the battery may be overcharged or undercharged by exceeding the designed threshold current during charging or discharging. In order to do that, the battery

[1] In all the graphics appearing in the current histogram, positive current is discharging current, while negative current corresponds to the charging process.

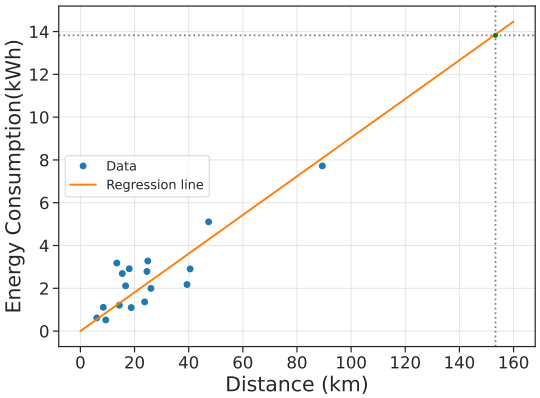

Figure 6.5: Energy consumption versus distance traveled for all the days of data acquired and the corresponding linear regression. The linear model obtained had ($A = 0.090 \pm 0.011$ kWh/km), $R^2 = 0.73$.

current values I_{batt}(A) were normalized with respect to its nominal capacity, according to equation 6.2 where $C_{rate}(h^{-1})$ is the battery C-rating, (I_{batt}) is the measure of the current that the battery is charged or discharged at, E_{rated} refers to the nominal capacity of the battery, that is, the total amount of energy that a battery can hold, here defined in Ah.

$$C_{rate}(t) = \frac{I_{batt}(t)}{E_{rated}} \tag{6.2}$$

Figure 6.6 shows a small example of the battery current profile expressed in terms of the C rate. The result shows that the current measured remains within a range of -1C to 1.5C, which corresponds to -70 A to 270 A. To build the histogram, the current values was discretized into 0.5C length bin, which is shown in table 6.2. The number of bins was chosen to be small as possible but at the same time to capture the finner details during the process of charge/discharge of the battery. The results of the histogram for each current range can be seen in figures 6.7 and 6.8. Looking at the first figure, which shows the number of events of current values during discharging/traction process and as described in section 6.1.1, there are a significant amount of points when the vehicle was at rest but still consuming some energy. Because of this, the points were filtered out of the histograms in order to better visualize a trend. The results show that as the current increases there are few points to be acquired, as well as the time duration increases, as expected. In addition very few points exist when the current duration exceeds 30s, which is the peak charging current duration selected by the manufacturers of the battery. For the second graph, which shows the current histograms during regeneration, the same trend occur and none points exists for the time duration greater than 30s, which indicates that the battery is in good conditions. and there is no need for selecting other type of battery technology.

Table 6.2: Battery C-Rating.

C-rate	Current (A)	Time (min)
0C - C/2	0 - 70	120
C/2 - C	70 - 135	60
C - 1.5C	270	30
$<$ 1.5C	-	

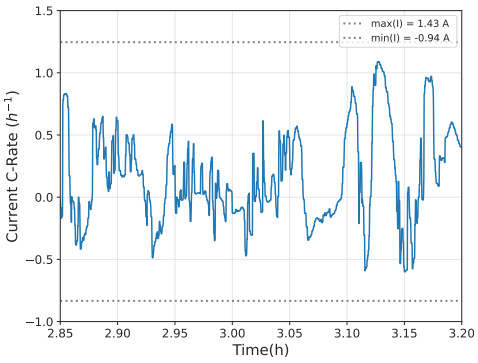

Figure 6.6: Current profile for rickshaw during an actual driving range expressed in terms of C-rate. The value seen in the graph corresponds to only a small part of the charge/discharge process.

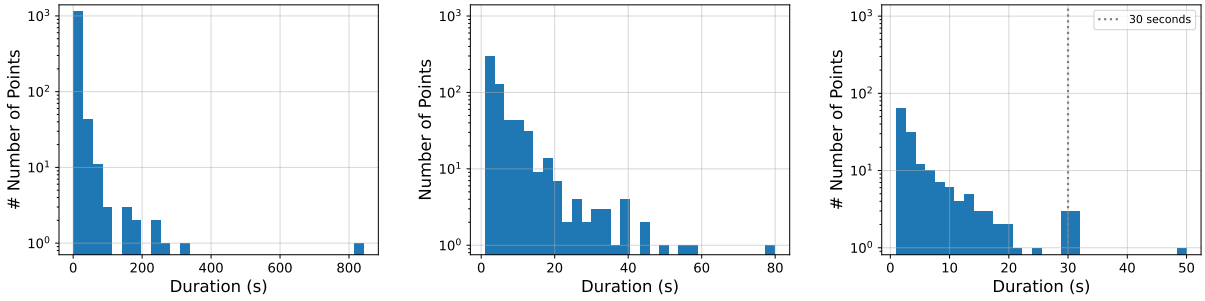

(a) (0C ; C/2) (b) (C/2 ; C) (c) (C ; 1.5C)

Figure 6.7: Histogram of battery current values during traction.

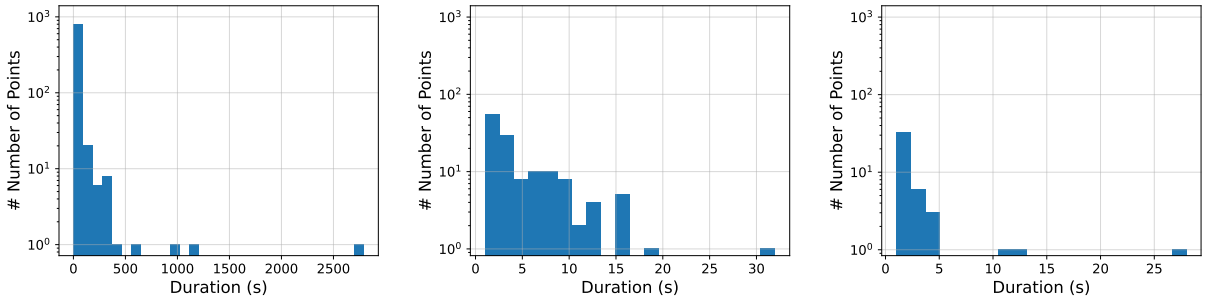

(a) (-C/2 ; 0C) (b) (-C ; -C/2) (c) (-1.5C ; -C)

Figure 6.8: Histogram of battery current values during regeneration.

6.2.2 Remaining Driving Range

In this section, the energy consumption profile is derived as a function of the velocity. For that data collected during vehicle operation was used to explore the relationship between energy consumption and velocity. In order to do that, data only on discharge processes were considered in this analysis, since the idea was to estimate how much energy the vehicle would spend on average. For doing so, the velocity values were discretized into bins length equally spaced and then computed the energy consumption for the points with velocities falling inside those bins.

In figure 6.9(a) the consumption curve estimated for the different velocities is shown. As can be seen, the power consumption is highly variable and changes when the velocity changes. With the

consumption values, another estimation that can be done is the expected Remaining Driving Range (RDR) that the vehicles travels at. This was achieved using the formula found in equation 6.3, where E_{batt} is the total energy in the batteries when fully charged in kWh, P_i is the estimated power consumption seen previously, and v_i is the vehicle's velocity. The estimated RDR curve as a function of velocity is shown in figure 6.9(b). It can be seen that there exists an approximate quadratic relationship between the two. However, it is worth noting that for larger velocities the range is more variable; this is due to the fact that, despite the larger losses forces, there is also a larger motor efficiency. This has a direct consequence on the remaining driving range, resulting in a more efficient use of energy.

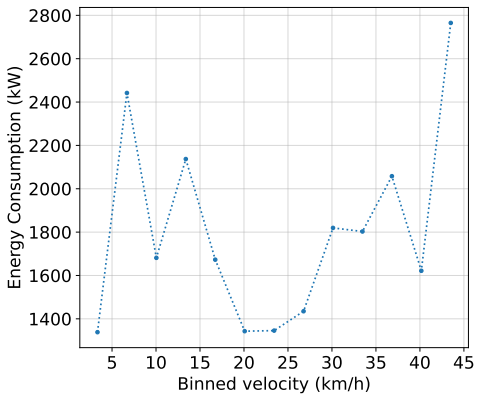

(a) Average energy consumption as a function of the velocity of the vehicle for the **solar rickshaw Limo GT** vehicle.

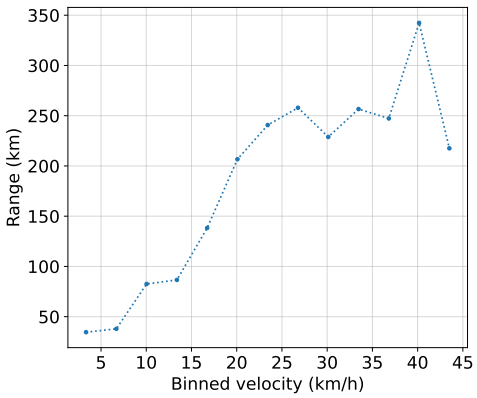

(b) Average expected remaining driving (RDR) as a function of the velocity of the vehicle for the **solar rickshaw Limo GT** vehicle.

Figure 6.9: Remaining Driving Range (RDR) as a function of vehicle velocity. The standard deviations was not presented in the graph because of its very large value.

$$RDR = \frac{E_{batt}}{P_i} v_i \tag{6.3}$$

6.3 Derived Features

As stated in the introductory part of this chapter, some of the relevant features were not directly measured, which is the case of the **road slope** and **distance** traveled. The purpose of this section is to explain how such features were estimated.

6.3.1 Altitude Data

As has been said, the altitude data collected using the on-board GPS device were not accurate enough to be used in the modeling. Otherwise, it would have a large effect on the prediction of gravitational energy and consequently causing the model to gets worsen, mainly in irregular terrain. To confirm this assumption, a trip was selected and shown in figure 6.11. For comparison purposes, in figure 6.11(b) it is shown two plots; the plot above displays the raw altitude data measured using the GPS receiver, and the plot below shows the predicted altitude data using the digital map for the same route. By observing these two plots, one may immediately conclude that the altitude data measured by

GPS were so inconsistent that, even though, using techniques of interpolation or filtering will be useless compared to the altitude data estimated using the digital map. Because of this, the alternative of deriving the altitude data from the topographical map will be used throughout this work and how it was obtained will be explained in the following paragraphs.

To correct the GPS recorded altitude data, a digital map of Lisbon city was built with the help of *Mapbox* in Python3 using their *Mapbox Terrain-RGB API*, which contains elevation data encoded in a simple png image format as RGB values. The API provides one height measurement increment of 0.1 meter for each square area of 17.5 m^2, which can be understood into every measurement of 5 meter. It is an easy-to-use API, so obtaining the altitudes data is as straightforward as simply passing the pair of coordinate of points (latitude, longitude). Nevertheless, *Mapbox* obtains the raw elevation data thanks to the realization of the Copernicus EU program, which is an international research effort with the objective of providing a Digital Elevation Model (DEM) almost on the Earth's land surface (from 56°S to 60°N. These data are generated from the weighted average of *Shuttle Radar Topography Mission (STRM) and Advanced Space-borne Thermal Emission and Reflection Radiometer (ASTERM)* [56]. Both datasets provide one elevation measurement for every square area of 900 m^2, which translates into one measurement for every 30 meter. Figure 6.10 shows an example of an elevation map for the Lisbon area considered.

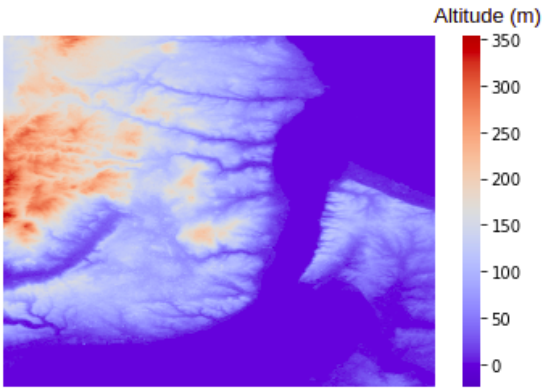

Figure 6.10: Elevation map for the Lisbon area considered in the Copernicus program dataset [57].

Road Slope Estimation

The slope of the road is defined as the angle the vehicle makes with respect to the horizon seen in chapter 3 (see figure 3.3). Using the obtained altitude profile from the digital map dataset and the distance traveled between each pair of coordinates, the road slope can be derived. Although, since the road slope is derived as the gradient of the altitude divided by the distance, some unreal peaks should be expected that would originate with the higher frequency data. For example, when the vehicle drives at low velocities, small altitude gain should result in an unrealistic peaks. In order to avoid those peaks, the road slope was calculated using a linear regression model. A general model can be seen in equation 6.4.

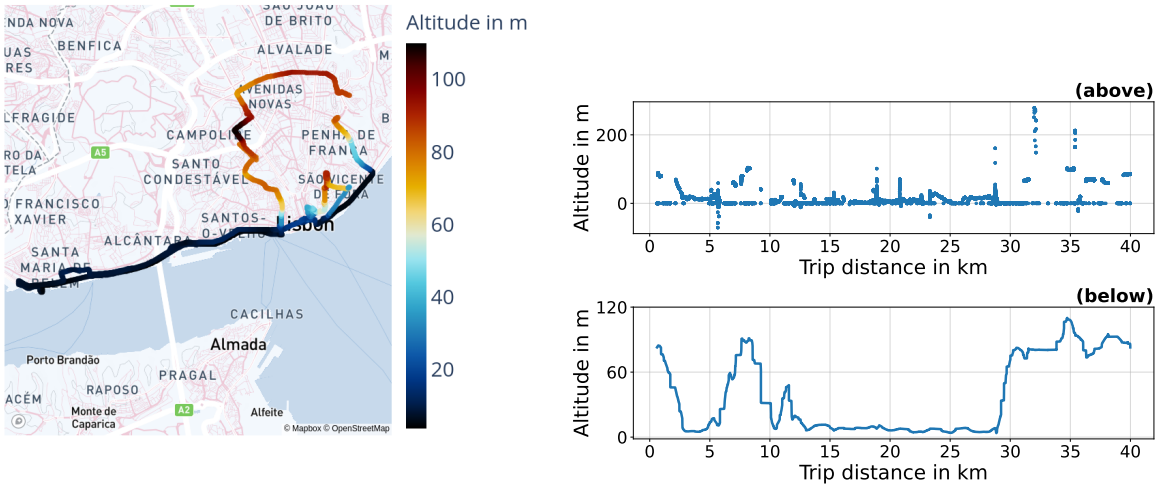

(a) Geographical distribution of the height values.

(b) Altitude profiles.

Figure 6.11: Altitude values measured using the GPS receiver (above), and the new altitude values predicted using the cartographic information dataset (below) of a round trip.

$$\Delta s_{xy_i} = \hat{\beta}_0 + \hat{\beta}_1 \cdot h_i \tag{6.4}$$

$$\hat{\beta}_1 = \frac{\left(\sum_{i=1}^{n} \Delta s_{xy_i} h_i\right) - \frac{\left(\sum_{i=1}^{n} \Delta s_{xy_i}\right)\left(\sum_{i=1}^{n} h_i\right)}{n}}{\sum_{i=1}^{n} \Delta s_{xy_i}^2 - \frac{\left(\sum_{i=1}^{n} \Delta s_{xy_i}\right)^2}{n}} = \tan\alpha \tag{6.5}$$

To estimate the slope of the road, an algorithm looks at previous n estimates of altitude (h_i) and distance (Δs) and estimates the slope of the road, as shown in equation 6.5.

The procedure for estimating road slope is shown on a particular trip to show its functionality. Figure 6.12(a) shows the estimation of the road slope as an example for the first 4500 seconds of vehicle motion. As can be seen, most of the trip, the road slope is almost zero and varies between -2 and 2 degrees.

6.3.2 Distance Estimation

One feature of the vehicle trip that can be calculated is the total distance traveled by the vehicle. It is possible to calculate the distance from the beginning to the end of the trip using trigonometric geometries represented in equation 6.6, where R_{earth} is the Earth radius considered equal to 6371 km on average, ϕ_m represents the average latitude of the points, $\Delta\phi$ and $\Delta\lambda$ are the differences in latitude and longitude of the two points, respectively. It is of relevance to mention that the equation below is only valid when the points are very close together, which is the case in this work.

$$\Delta s_{xy} = R_{earth}\sqrt{x^2 + y^2} = R_{earth}\sqrt{\Delta\phi^2 + (\cos\phi_m \cdot \Delta\lambda)^2} \tag{6.6}$$

As we can note, the above equation only considers variation on the plane, as shown in figure 6.13. To have the total distance traveled by the vehicle if the positions have a different altitude can be calculated

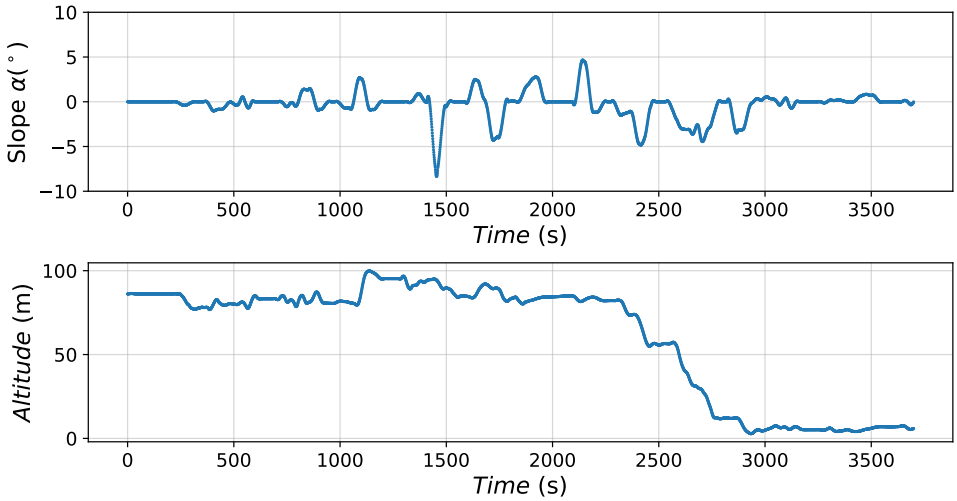

Figure 6.12: Road slope estimation (curve above) for the vehicle trajectory considered and the altitude profile (below). To determine the road slope, 30 past data points was considered, which translates into each 9 seconds of data samples.

using the Euclidean distance, as shown in the equation 6.7 below.

$$\Delta s_{tot} = \sqrt{(\Delta s_{xy})^2 + (\Delta h)^2} \tag{6.7}$$

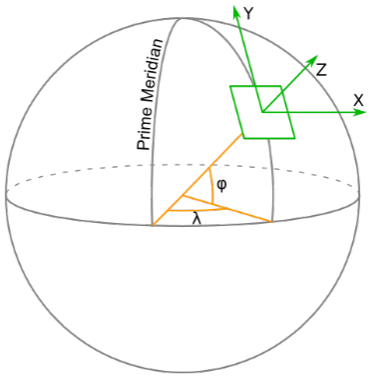

Figure 6.13: Representation of the X, Y and Z axis. Adapted from [28].

Chapter 7

Results and Discussion

The present chapter is divided into 4 sections covering various aspect of the work done in this thesis. The first section presents the results of the longitudinal dynamics model used to predict the energy consumption of the proposed low-cost solar electric rickshaw, with a particular emphasis on the real contribution of the solar photovoltaic power during vehicle trips for several environmental conditions using real-world data. In this section there is also the implementation of the Remaining Driving Range (RDR) of the vehicle. The second sections examines in detail the real benefits that the solar-powered electric rickshaw can really offer to the costumer; this includes estimating the economic return investment on ROI value of adding solar panels directly to the rickshaw's roof as well as the payback period of this project. In the last section, anew battery pack technology that best balances the energy produced by the solar panels and the vehicle load was selected.

7.1 Vehicle Performance Model

To accurately predict the energy consumption of the vehicle, an accurate vehicle model is needed. The purpose of this section is to specifically address two important questions: (i) Can the model accurately estimate the instantaneous power of the vehicle and (ii) Can the model accurately estimate the total energy consumption of the vehicle for a given trip? For that, we will make use of several models with different levels of complexity which are based on longitudinal vehicle dynamics that were introduced in chapter 3. Before that, a short description of the input received by the model is given.

7.1.1 A Priori Physical Model

The very first model that can be implemented is what is called a **priori model**, as its name suggests, this model uses no data collected from the vehicle to base its calculation. The a priori model is based on the underlying physical model that describes the forces acting on a vehicle's motion as described in section 3.1.1. It relies only on vehicle-specific parameters and characteristics such as the velocity traveled in a trip [1], acceleration and the road slope. Because of this, this model is commonly used

[1] Here the definition of a trip is a velocity profile describing the movement of a vehicle from a origin to a destination.

in vehicle simulations where experimental data is not a concern, and with a fair estimate of vehicle parameters, good results are expected to be achieved. The general equation that governs this model can be seen in equation 7.1, where F_{te} is the traction force seen at the wheel and v is the vehicle velocity.

$$P_{wheel}(t) = F_{te} \cdot v(t) \tag{7.1}$$

$$F_{te}(t) = m(1+\epsilon_i) \cdot \frac{dv(t)}{dt} + f_{r0} \cdot m \cdot g \cdot \cos\alpha \left(1 + \frac{v(t)}{44.4}\right) + \frac{1}{2}\rho \cdot C_d \cdot A_f \cdot v(t)^2 + m \cdot (g \cdot \sin\alpha) \tag{7.2}$$

In order to determine the vehicle mechanical power, we first need to know the values of the parameters presented in equation 7.2. It should be noted that some of these parameters including vehicle mass and frontal area are features of vehicle so they can directly be measured from the vehicle itself. Moreover, the total mass of the vehicle that was derived previously did not consider any payload, which is unrealistic for the real operation of the vehicle. However, it is not possible to concretely determine the payload because the vehicle constantly changes its number of passengers. Because of this, in all the models presented here in this work, the worst case approach including a maximum payload has been considered so that the model will overestimate the measurement data. Other parameters that are difficult to measure such as rolling resistance coefficient and aerodynamic drag coefficient were obtained based on the previous study on a similar type of vehicle [29]. For further models, other parameters are required, such as the gear ratio of the drive shaft and the radius of the tire. The gear ratio was estimated from the previous study for the same type of vehicle [28] and the tire radius was calculated using the wheel information found in table 3.1. Table 7.1 summarizes all the aforementioned vehicle parameters used in the model. In addition to the vehicle parameters, there are two unknown variables to estimate, including linear acceleration and slope of the road but these can be easily derived from the external measured data. Acceleration was derived from velocity variation and extracting its rate of change and slope of the road was estimated using a linear regression model for the previous 30 acquisition points, which corresponds to one measurement every 9 seconds. And lastly the velocity data used were the ones measured by the GPS device.

Finally, the a priori model was implemented for real trips to show its functionality. In figure 7.1 the instantaneous power profile, as well as the road slope of a trip are shown as an example. First looking at the road slope, it can be seen that for the majority of the trips, the road slope is almost negligible and varies between -5 to 5°, except in some cases where there are some high peaks around 20°. Now, looking at the estimated power consumption, we can see that the estimated power is not consistent with the measured power, which seems to indicate that the model underestimates the measurement data. This can be explained due to the unreliability in estimating the road slope from the official height map. For comparison purposes, the total energy consumption for a full trip was also determined by summing up the energy consumption at each time step. The average error relative to the measured data obtained was -52%, which confirms that the model also underestimated the energy consumption. One of the downsides of this model is that it ignores any losses in the power train, in other words, it always

considers the efficiencies of the components in the vehicle drive-train to always be 100%.

Table 7.1: Suggested values for the parameters in equation 7.1 for the **rickshaw Limo GT** vehicle.

Parameter	**Symbol**	**Expected Value**
Vehicle Mass	m	903 kg
Maximum Payload	-	300 kg
Gear Ratio	g_{ratio}	10:1
Radius of Tire	r_{tire}	0.2895 m
Rolling Coefficient	f_{r0}	0.012
Drag Area	$C_d . A_f$	1.75 m^2

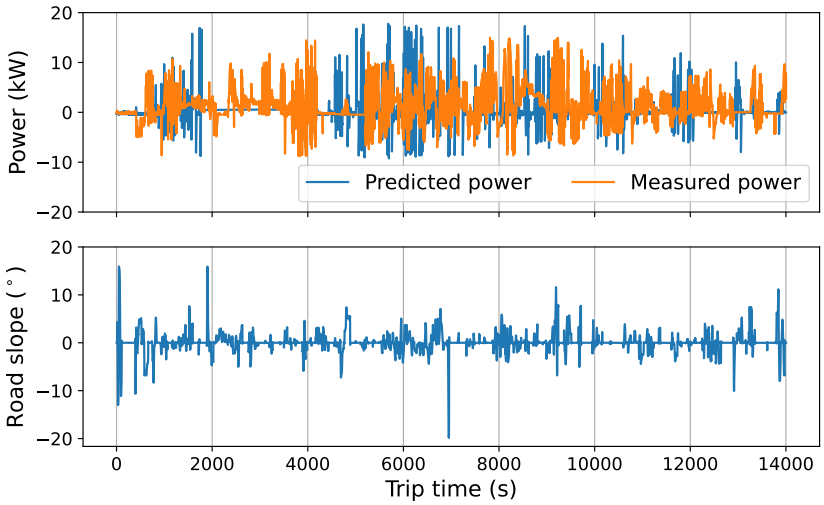

Figure 7.1: Power consumption estimation using the longitudinal dynamic model for a specific route. The relative error for the full trip was -50%.

7.1.2 A Priori Physical and Electrical Model

One way of improving upon the a priori model is to describe the losses that occur inside the **power-trains**. One of the components that affect the vehicle's energy consumption the most is the motor. The electric motor is expected to change its values significantly depending on torque and angular velocity. The motor efficiency is a parameter that can be calculated experimentally by performing tests in the vehicle, or the efficiency curve is sometimes reported on the datasheet. Unfortunately, the manufacturer did not provide any information on the motor of the vehicle studied in order to base the calculation. Nevertheless, using the instantaneous power obtained from the a priori model it is possible to estimate the efficiency of the motor. This efficiency represents the joint efficiency of all the components of the drive-train that sends the power from one component to another, i.e., electric motor, power converter, motor controller, and differential [58] as described in section 3.1.

The efficiency of the power train can be determined using the power measured flowing in the batteries as given by equation 7.3. The efficiency was then expressed as a function of torque and angular velocity of the motor. The torque $T_l(Nm)$ was calculated according to equation 7.4, where $r_{tire}(m)$ represents the radius of the tire and g_{ratio} is the gear ratio of the drive shaft. The angular velocity was also determined using the equation 7.5. All these parameters can be seen in the table above.

$$\eta_{tot}(\omega, T_l) = \frac{P_{wheel}}{P_{meas}} \tag{7.3}$$

$$T_l = \frac{r_{tire} \cdot P_{wheel}}{v \cdot g_{ratio}} \tag{7.4}$$

$$\omega = \frac{v}{r_{tire}} \tag{7.5}$$

7.1.3 Instantaneous Total Power Estimation

The estimation of the previously calculated efficiency map of the motor allows the estimation of total instantaneous power at each point on the vehicle trajectory using equation 7.6, where P_{wheel} represents the traction power calculated previously. We then intend to compare the **predicted power** with the instantaneous **measured power** directly by the BMS.

$$P_{batt} = \eta_{tot}(\omega, T_l) \cdot P_{wheel} \tag{7.6}$$

Figure 7.2 shows an example of the power consumption estimation on a trip on August 20, 2021. Figure 7.2(a) and 7.2(c) are taken from areas near Lisbon city center, where the road slope is more variable, whilst figure 7.2(b) is taken in the areas where the road slope is almost zero or very close to it. The estimation of the road slope is presented in both graphs as a background for the figure. Looking at the second graph, we can clearly see that the blue curve, which corresponds the predicted power consumption, is far from following the orange curve, which represents the measured power consumption. However, the same trend does not actually occur for the first and third plots. In addition to this, it is relevant to note that the predicted power starts to fail when the measured power is constant, which was speculated to be due to the unreliable estimation of the slope of the road.

In order to better understand the influence of the road slope on energy consumption, the power consumption was also determined without including the gravity term in the model in the equation 7.2 and the results are shown in figure 7.3. Now looking at this detail, it is possible to get that for the first and third examples, the predicted power more follows the measured power, whilst for the second examples the same trend was not possible to achieve. Therefore, we can immediately conclude that the estimated road slope was not as reliable as possible for the model to be accurate enough; this is due to the unreliable estimation of the altitude values from the pair of coordinates measured by the GPS device. As the instantaneous power of the vehicle could not be accurately estimated, this model could not be further applied in the estimation of the total energy consumption on a trip.

7.1.4 Trip Vehicles' Energy Consumption Estimation

As it was discussed previously, the total instantaneous estimated power by the model was not sufficiently accurate enough to be used to determine the total energy consumption of a trip. This is mainly due to the difficulty in calculating the slope of the road from the external map derived in section 6.3. The

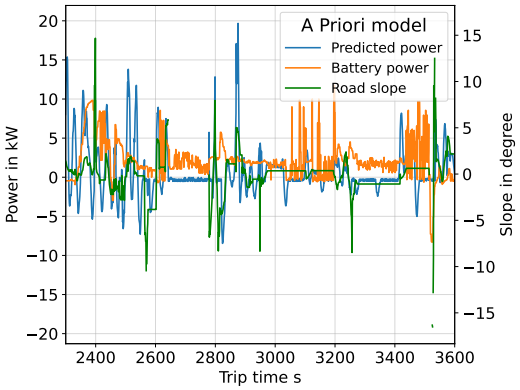

(a) Example 1: Slope variable

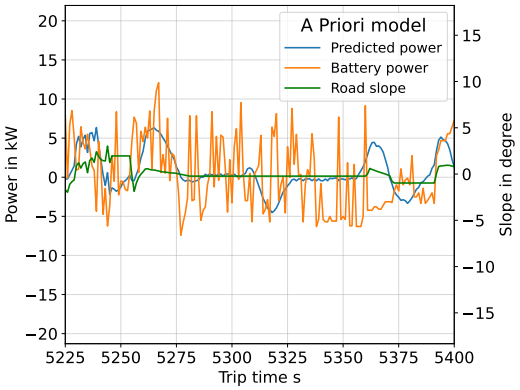

(b) Example 2: No slope

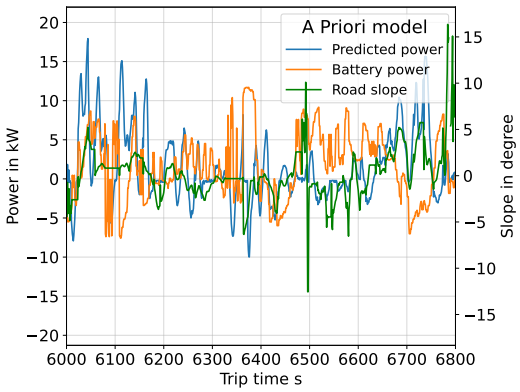

(c) Example 3: Slope variable

Figure 7.2: Examples of the power consumption values estimated for the longitudinal dynamics model for different cases of road slopes: Example (a) and (c) for higher slope and example (b) low slope.

goal of this section, on the other hand is then to find a way of estimating the overall energy consumption in a trips, but using a different approach from that used previously in section 7.1.2. The total energy consumption of the vehicle trip were described in chapter 3 and takes the form of equation 7.7.

To be able to estimate the energy consumption of the vehicle for a given trajectory, we have derived a set of features out of the data collected that contribute to the energy consumption. All the features considered for the model are shown in table 7.2. The first term considered was the variation of the velocity squared, which is related to the variation of the kinetic energy of the vehicle. The second and third features represent the total distance traveled and the integral in the distance, which are associated to the energy dissipated by the rolling resistance force of the tires and the integral in the distance. The fourth feature considered was the integral of square of the velocity, which corresponds to the energy dissipated by the aerodynamic drag force. And then, the last feature was the total variation in the altitude, which is related to the variation of potential energy due to local gravity.

As seen, some features are function of the integral in the distance that have to be estimated. Those were then determined using a trapezoidal rule of the integral, as stated in equation 7.7, where Δs_i represents the distance variation between the acquisition point i and the previous point $i-1$. Looking at that equation, it is of relevance to note that it only represents the energy spent in the batteries provided to the motor. So to find the total energy consumption, we need to subtract it from the energy produced

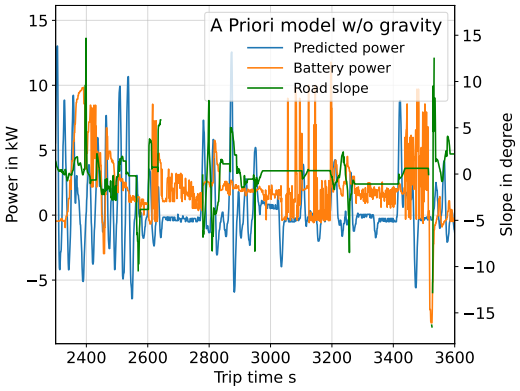

(a) Example 1: Slope variable

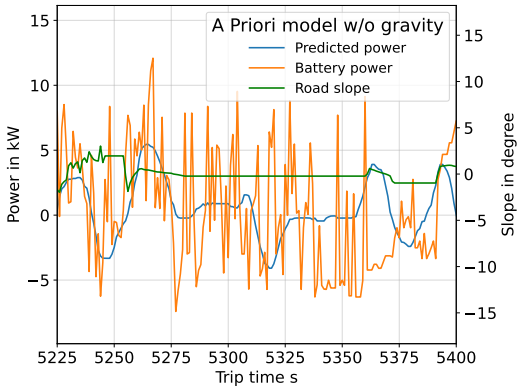

(b) Example 2: No slope

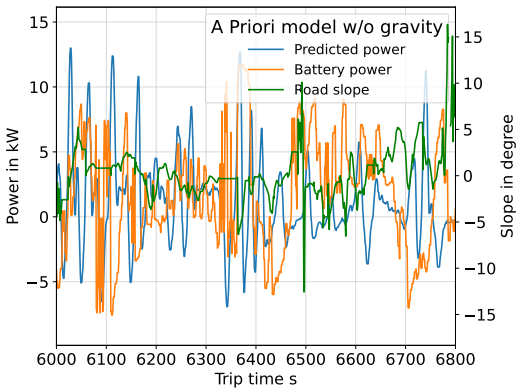

(c) Example 3: Slope variable

Figure 7.3: Examples of the power consumption values estimated for the longitudinal dynamics model without the gravity term for different cases of road slopes: Example (a) and (c) for higher slope and example (b) low slope.

by the photovoltaic panels array. In addition to this, we have assumed that the company that owns the vehicle recharges the vehicle's battery overnight using energy from the electrical grid.

$$E_{wheel} = \frac{1}{2}m(1+\epsilon_i)\cdot(v_f^2 - v_i^2) + f_{r0}\cdot m\cdot g\cdot\left(\Delta s_{xy} + \frac{1}{44.4}\sum_i v_i\cdot\Delta s_i\right) + \frac{1}{2}\rho\cdot C_d\cdot A_f\cdot\sum_i v_i^2\cdot\Delta s_i + mg\cdot\Delta h \tag{7.7}$$

$$E_{batt} = \begin{cases} E_{wheel} - E_{solar}, & \text{During the day} \\ E_{grid}, & \text{Overnight} \end{cases} \tag{7.8}$$

In figure 7.4, it can be seen the balance of energy consumption for one day of vehicle trip, both with and without using on-board solar energy. Figure 7.4(a) shows the total accumulated energy consumption as a function of the distance traveled on a typical sunny August day. The results reveal how solar energy can actually contribute to increasing the capacity of the battery pack as the rickshaw drive during the day. With the assumption that both rickshaws starts at the same level of SOC, the solar rickshaw SOC

Table 7.2: Main features derived from the collected data for computing the total energy consumption of the vehicle on the trip and their respective expressions.

Term	Expression
Variation of the velocity squared	$(v_f^2 - v_i^2)$
Total distance traveled	Δs_{xy}
Altitude variation	Δh
Integral of the velocity in the distance	$\sum_i v_i \cdot \Delta s_i$
Integral of the velocity squared in the distance	$\sum_i v_i^2 \cdot \Delta s_i$

ended at 56%, while the non-solar rickshaw SOC at 33%. Therefore, at the end of the day, the solar rickshaw would need about 5.93 kWh of additional energy from the grid and the non-solar rickshaw 9.22 kWh. This means that about 3.26 kWh was supplemented by the solar panels, which corresponds to a reduction of 35% of the energy consumed by the solar rickshaw compared to the non-solar rickshaw, thus demonstrating a significant improvement.

On the other hand, in figure 7.4(b) it is possible to see the same energy consumption, but now for a typical February cloudy day. The result shows that the rickshaw cannot suddenly store some energy on the batteries due to the fact of the lower solar radiation available in the regions where the rickshaw was driven in. We can conclude that the contribution of solar panels to this day is such that it only contributes 14% or 0.25 kWh of energy into the battery pack. The solar range extension was just 12 km. Furthermore, the overall predicted energy was also estimated for all days of data collection and compared with the energy measured by the BMS. The results can be seen in figure 7.5, as it can be observed, the energy predicted follows quite well the energy measured by the BMS. To access the performance of the model relative to the measurement data, the metric used was the root mean square error (RMSE). This is a common metric used to evaluate regression models. Abstractly speaking, it is a measure that tells how far the predicted values are from the measurement values. Mathematically, it is formulated according to equation 7.9, where E_{meas} and E_{pred} are the measured and predicted values, respectively. The RMSE obtained was 24%, indicating that the model correlates fairly well the measurement data.

$$RMSE = \sqrt{\frac{1}{n}\sum_{i=1}^{n}(E_{meas} - E_{pred})^2} \tag{7.9}$$

7.2 Solar-Powered Rickshaw Benefits

As seen in the previous section, the performance analysis gives an overall picture of the benefits of the proposed solar rickshaw compared to the nonsolar rickshaw. Some of these benefits are often categorized into driver, and economical benefits being all these benefits derived from the reduced energy consumed during the trips. Therefore, this sections' goal is to present a detailed analysis of the aforementioned benefits of the solar rickshaw compared to the nonsolar one [2].

[2]nonsolar rickshaw is defined as if the rickshaw had no solar panels installed and assumed the rickshaw performed the same tasks as the solar rickshaw.

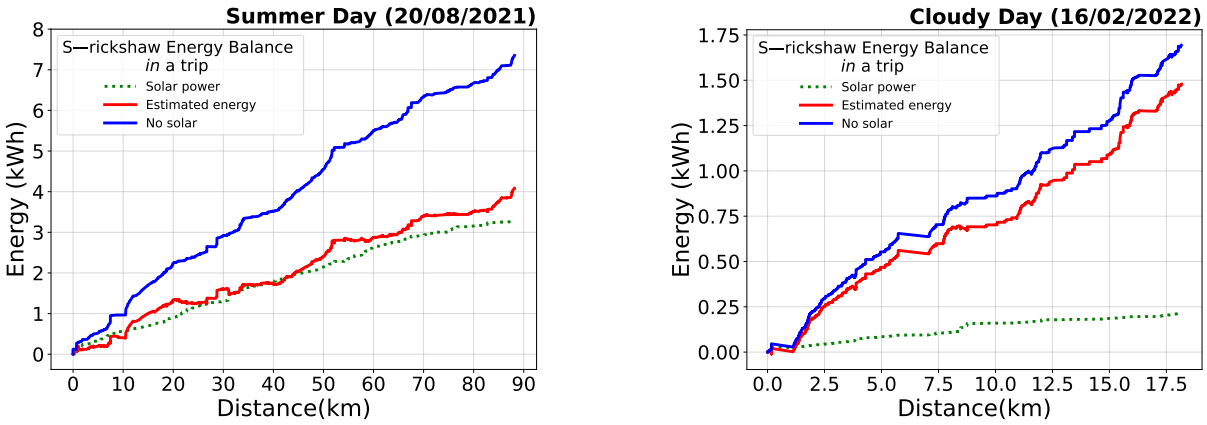

(a) Sunny day.

(b) Cloudy day.

Figure 7.4: Energy consumption balance over one example sunny day (a) and over a cloudy day (b), both for a rickshaw without onboard solar, and the proposed solar rickshaw.

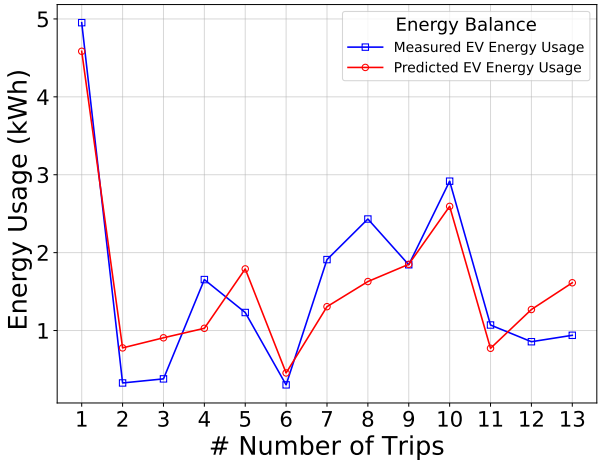

Figure 7.5: Measured and predicted energy consumption for all the 13 days of data acquisition for the longitudinal dynamics model. The model resulted in an average relative error of -7% and a standard deviation of 1.06.

7.2.1 Driver Benefits

As discussed in section 5.1, the two driver benefits of adding solar panels to the roof of the vehicle are the potential to increase the range of the vehicle and the reduced charging costs. These estimations are made considering the data collected during vehicle trips being split in different months of the year the data were acquired. In figure 7.6(a) shows the average daily solar range extension. The results show that the maximum range was obtained on a clear sunny day in mid August, as expected. This indicates that more than 50% of the total daily distance traveled by the vehicle was provided by solar energy. However, the minimum range was reached in mid-October where the shading factors are more evident. In addition, it has also shown that average daily solar energy range extension is fairly 16 km, this is to be expected because as was said in previous sections the solar energy is highly variable throughout the day.

The second benefit is the charging cost reduction as can be see in figure 7.6(b) where is shown the relative reduced costs for a complete battery charging. These improvements are in the same magnitude

of solar range extension described above, which is to be expected because the price of buying electricity from the grid was considered to be constant and equal to 0.23 €/kWh.

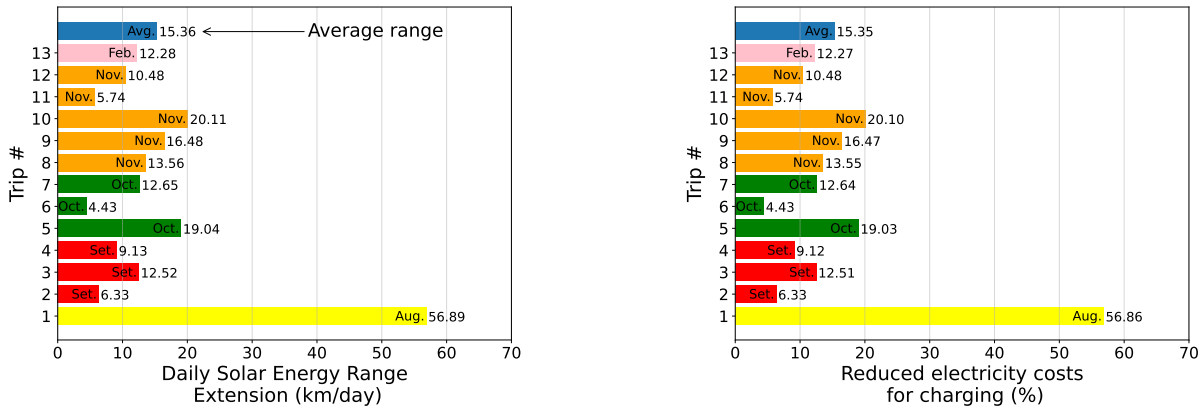

(a) Daily solar range extension

(b) Relative reduction in electricity costs.

Figure 7.6: (a) Daily solar range extension for different days of data acquisition. (b) Solar rickshaw effect on daily rickshaw charging. For comparison purposes, the total electricity cost for charging the nonsolar rickshaw is approximately $C_{ns} = 3.174$ €.

7.2.2 Economic Analysis

The success of any technology is quantified by its economic prospects. In order to economically access the feasibility of the proposed system, we will make use of two economic indicators. Return on investment (ROI) and payback time. Each one is described below.

Return on Investment (ROI)

Return On Investment or simply ROI is a performance measure that is used to evaluate the amount of additional profit generated due to a certain investment or a project and is extensively used across finance to compare different scenarios for an investment to see which would generate the greatest profit. In the context of the present work, it is used to determine the real benefits of the proposed low-cost solar electric rickshaw concept in terms of the return on money (cost of adding on-board photovoltaic system) throughout its lifecycle as done in [12]. The Return On Investment can be determined according to equation 7.10, where the values in the numerator correspond to the total net benefit (return) of an investment, which is quantified as the difference between the total gains (G_{total}) and the initial investment of the system (C_{inv}), and the denominator represents the initial cost of investment. Its value is commonly expressed as percentage.

$$ROI\ (\%) = \frac{G_{total} - C_{inv}}{C_{inv}} \times 100. \tag{7.10}$$

The total cost of investment consists of the operating costs, buying costs expressed in today's price in €/kWh, maintenance costs, and replacement costs. For the system implemented in this work, the investment cost of the system can be determined by applying a simple linear cost function, as repre-

sented in equation 7.11, where the first term corresponds to the price due to the photovoltaic module power; c_p is the cost of the photovoltaic panel (€) and P_{PVp} is the total nominal photovoltaic panel installed capacity (kW), and the remaining terms corresponds to the price owed to mounting, installation and maintenance costs, respectively.

The investment cost was determined considering two different scenarios of the prices of photovoltaic panels (a high- and low-price scenario). The high cost of photovoltaic modules was estimated based on current commercial prices for silicon silicon solar modules, which is 0.33€/W without tax [59]. Since the total installed modules is rated at 660 W_p, the cost of photovoltaic modules was found to be approximately 230€ with an additional tax of 7%. Although the low price of photovoltaic modules was found to be around 141€ based on the energy cost of 0.2€/W [59]. The mounting cost (c_{mount}) with the fuses and wires are estimated as 80€. The installation cost (c_{inst}) was assumed to be 12% of the total cost of the system, found equal to 37.2€ and 26.54€, respectively.

$$C_{inv}\ (€) = c_p P_{PVp} + c_{mount} + c_{inst} + c_{main} \tag{7.11}$$

The total maintenance cost of the entire life of the system can be determined according to equation 7.12. It determines all future cash flows throughout the lifetime of the investment discounted to the present. Following equation 7.12 [12], M_y is the yearly maintenance cost and taken at around 2% of the initial cost of the project [12], i_r is the inflation rate, which is a measure of the decline in the value of money. For example, if the inflation rate is 2% per year, then an item will cost 2% more next year. For the case of Portugal, the inflation rate was found to be at around 5.3% [60] and d_r is the discount rate, which was taken as 6% for [61].

In general, photovoltaic modules have a lifetime of about 25 years or more. However, this vehicle has a warranted life of 6 years, which corresponds to the lifetime of the batteries [28]. A total of 15 years (T_{life}) was chosen here as a conservative average value for the solar panels lifetime. Thus, it is expected that at the end of the life cycle of the vehicle, this application can be transferred to another vehicle. The total maintenance costs per year were then determined and found to be 98.23€ and 70.45€, respectively, for the two different scenarios of the price of electricity. Finally, the total cost of the investment was calculated as defined in equation 7.11 and is listed in table 7.3. For further calculations, the system's total cost was considered the average of the two already defined scenarios.

$$c_{main}\ (€) = M_y \times \left(\frac{1+i_r}{1+d_r}\right)\left(\frac{1-\left(\frac{1+i_r}{1+d_r}\right)^{T_{life}}}{1-\left(\frac{1+i_r}{1+d_r}\right)}\right) \tag{7.12}$$

Lastly, with regard to the gain on investment, it can be determined from the following formula presented in equation 7.13. It takes into account the possible range extension and the energy price of the grid paid for charging the vehicle. However, the price of electricity (C_{ele}) is known to vary from location to location, but in this work it is assumed that the vehicle is recharged at home, so that the price paid for electricity remains practically constant and was assumed to be around 0.23€/kWh, which is a typical value of the average price of electricity for most of the zones in Portugal according to [62]. The daily solar

Table 7.3: Cost of investment per components considered in the calculation of the economics indicators

Component	High price	Low price	Note/Reference
PV Price c_p(€)	230.0	141.2	High and low estimation costs based on 0.33€/W and 0.2€/W [59]. Adding a tax rate of 7%.
Mounting cost c_{mount}(€)	80	80	
Subcomponents cost (€)	310	221.2	Summation of previous components
Installation cost c_{inst}(€)	37.2	26.54	12% of sub-components cost
Maintenance cost c_{main}	98.23	70.45	Equation (7.12)
Total cost C_{inv} (€)	407.8	281.3	Resulting in a mean total cost value equal 382€

range extension was estimated according to the equations defined previously and the vehicle lifetime is 6 years.

$$G_{total}(€) = E_{EV,non-solarEV}(kWh/km) \times D_{max}(km/day) \times C_{ele}(€/kWh) \times 365.25/4 \times T_{life}(years) \tag{7.13}$$

In figure 7.7(a) there can be seen the result of the estimated Return on Investment for each day of the collected data. It is possible to see that when the vehicle was driven in the low solar radiation areas, i.e., from Autumn to Winter, ROI presented a very low value and even negative ($\sim -21\%$), as one should expected. However, when the vehicle was driven in the high solar radiation area (typical sunny days), ROI presented a positive value and was found to be around 615% over the lifetime of the system, which corresponds to a gain of approximately 7.15 times the initial investment cost. This is to be expected because as said previously the more solar radiation available the more solar energy range extension is expected to be achieved. In the figure 7.7(a) it can also be seen the average ROI for all the day of the data collection, showing a positive value and 92% over the lifetime of the system, which is translated into a gain of 1.93 times the investment cost.

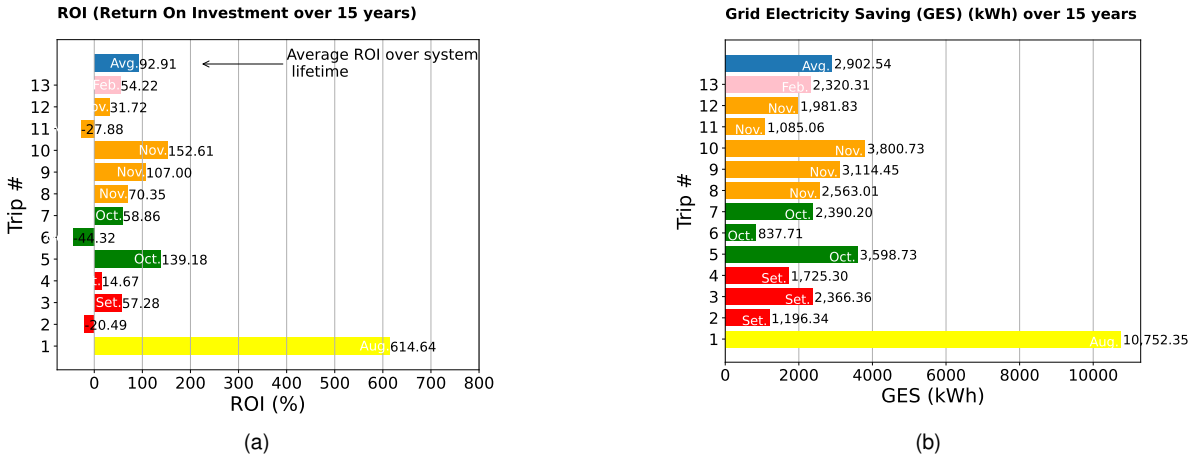

Figure 7.7: Return On Investment and (b) the amount of the saving of grid electricity over the lifetime of the solar panels.

Another benefit that can be estimated is the amount of grid electricity saved as shown in figure 7.7(b). The results reveal that a total of 10750 kWh of electricity is expected to be saved from the grid on typical sunny days, which represents fairly 164 € each year. This value is consistent with the average revenue found in section 5.1.

Payback Period

Another indicator worth determining is the payback period of investment. The payback period refers to the time in which the initial of investment can be effectively paid back, in order words, it is the length of time it takes to completely recover the cost of investment in a certain project. It is used to evaluate the risk inherent in a project taking the initial cash inflows into consideration and ignores the cash flows when the initial investment is recovered. To be able to calculate the payback period, one needs to calculate the cumulative cash flow for each year. It can be calculated using equation 7.14 [63], where t is the last year with negative cumulative cash flow, C_t is the cumulative cash flow at year t and C_{t+1} is the cumulative cash flow at year $t+1$.

$$\text{Payback period} = t + \frac{C_t}{C_{t+1}} \tag{7.14}$$

Based on the input parameters from table 7.3, the payback period of the proposed solar rickshaw was found out to be 5 years and the resultant trend can be seen in figure 7.8. The plot starts with a negative cash flow resulting from the capital investment of constructing the solar rickshaw. Over the years, the payback adds up and progress towards the positive side of cash flow. This means that after 5 years of implementation of this system, the driver practically gets some amount of energy for free.

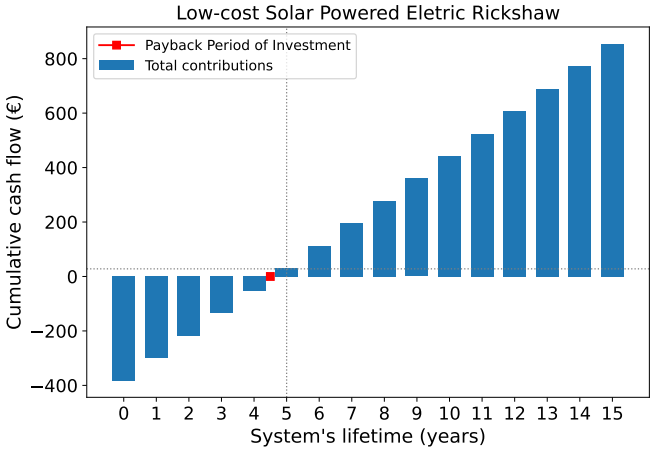

Figure 7.8: Representation of the net cash flow during the proposed system's lifetime, which demonstrates a 11 years of recovery time after its installation.

7.3 Battery Selection

The objective of this section is to propose a new battery pack technology for the built solar electric rickshaw. Considering the results found in previous sections that for a typical sunny day, the set of three

solar panels technology put on the vehicle's roof can cover up to 35% of the total net energy consumption of the vehicle, which results in an average vehicle energy consumption per kilometer of 0.087 kWh/km, which corresponds to 8.7 kWh/100 km. To have a mean of comparison, this value is consistent with the average energy consumption of A = 0.097 kWh/km = 9.7 kWh/100 km derived in section 6.2. This represents 30% increase in the range of the vehicle, relatively to the range provided by the vehicle manufacturer. Considering the seasonal nature of the vehicle, the new battery pack estimation can be taken practically to the limit of a similar reduction in the energy capacity of the batteries. Table 8.1 shows the comparison of the main characteristics between the actual battery pack equipped in the vehicle and the new one proposed in this work. Looking at the table we can conclude that the new proposed battery pack can decrease the vehicle weight in approximately 8%, which on the other hand will make the vehicle more lighter and thus would allow it to drive even more rapid.

Table 7.4: Comparison between the actual battery pack in the vehicle [50] and the new battery pack proposed [64].

Parameter	$LiFePO_4$	Battery reduction	New battery pack
Nominal Voltage	76.8 V	76.8 V	76.8 V
Capacity	180 Ah	117 Ah	135 Ah
Mass	135 kg	-	63.12 kg
Energy density	102 Wh/kg	-	164 Wh/kg
Cost per pack	186 €	-	132 €

Figure 7.9: New suggested battery pack [64].

Chapter 8

Conclusions

With this chapter we complete the work done on behalf of this Master's Thesis project, summarizing its main results and achievements (**section 8.1**) as well as some ideas that could be taken to improve and several ways to further extend this project (**section 8.2**).

8.1 Achievements

The present Master's Thesis project had the objective of optimizing the process of charging electric rickshaw batteries with onboard solar systems with the intent of demonstrating its usability based on a daily history of journeys. To that end, the present work was divided into 3 main parts: In the early stage of this work, the solar rickshaw was successfully constructed. That involved the integration of the photovoltaic panels into the vehicle's roof. To do so, a set of supporting structures were constructed in order to accommodate the solar panels on the vehicle's roof (as described in section 5.3.3).

The second part of this work consisted on building a data acquisition system to record and collect data from multiple sensors located inside the vehicle. In general, the information regarding the solar panels was collected by the PZEM sensor; these data contained information about the solar power output, such as instantaneous, current, voltage, and power, but also accumulate energy production. The information concerning the battery pack was collected by the BMS; the information provided by the BMS was the battery pack voltage, current, power, SOC, etc.. And finally, the information regarding the vehicle's position was collected from the GPS receiver, which contained the latitude, longitude, and the altitude of the vehicle as well as its velocity throughout the trip (described in section 5.4.2). To acquire all this information and save it in a file, a Raspberry Pi was used. The communication was made through serial communication using Python 3. It was also successfully developed an algorithm that uploaded those files into a remote server for more immediate access to the data without having to connect to the Raspberry Pi via SSH to obtain the data (section 5.4.4). The algorithm was developed in GNU Bash and was run on the Raspberry Pi every 1 minute.

In the third and last part of the work, the data collected for several environmental conditions were used to evaluate whether the proposed system yields real improvements in the vehicle's performance. Our results have shown that for a typical sunny day in the mid-season, three solar panels of 220 W each

with a conversion efficiency of 13.2%, the solar power can cover up to 35% of the energy consumed in the vehicle. With this proposed system, an increase in autonomy of 56 km was achieved, relatively to the range provided by the manufacturer. On the other hand, for a typical winter day, an autonomy of 12 km is possible to be achieved, which indicates that this increment in the autonomy is sufficient to justify its use.

Furthermore, the return on investment of adding photovoltaic panels onboard with the electric vehicle over its lifetime shows only a negative value (-21$\%$) in mid-October when the vehicle is driven in areas of low solar radiation. However, when the vehicle is driven on a typical sunny day the ROI is positive (615$\%$), indicating that after 5 years of the implementation of this project, the driver practically gets some amount of energy for free. Based on this result, a new battery pack was selected as shown in table 8.1. It should be noted that, owing to the seasonal nature of the vehicle, where greater consumption is expected on sunny days due to its tourist characteristics, these savings can be taken practically to the limited of a similar reduction in the energy capacity of the batteries. This reduction in battery capacity leads to the reduction of 8% in vehicle weight.

Table 8.1: Comparison between the actual battery pack in the vehicle [50] and the new battery pack proposed [64].

Parameter	**Actual battery pack $LiFePO_4$**	**New battery pack**
Nominal Voltage	76.8 V	76.8 V
Capacity	180 Ah	120 Ah
Mass	135 kg	63.12 kg
Energy density	102 Wh/kg	164 Wh/kg

As a final remark, it is worth mentioning that all the datasets collected during vehicle movement and the models implemented in this work are openly available on the Helianto Project official website at **Helianto Project** [14].

8.2 Recommendations for Future Work

During the development of the present work, several topics came up that need to be concluded and/or could be further improved/explored in future works.

Firstly, starting with the electric vehicle, the built S-rickshaw can be improved by adding the possibility to replace the solar panels with a new type of solar panels of greater efficiency. Among the various types of solar panels that already exist on the market, there has been recent industry interest in flexible, thin-film solar panels, and these panels are expected to play a crucial role in the solar industry shortly [65]. This addition will, in principle, affect the prediction of the vehicle range, which would have to be updated not only on the energy consumption of the vehicle but also on the energy harvested by the solar panels, as done in this work. Second, it will be necessary to incorporate an MPPT controller (Maximum Power Point Tracking) into the system in order to optimize the power extracted out of the solar photovoltaic panels' array for charging the battery pack. The MPPT will ensure that the solar panels will always operate at maximum efficiency, regardless of weather conditions.

From a data acquisition point of view, there are numerous issues that could be addressed to improve the quality of the collected data. First, one improvement would be the change of the GPS receiver used with a new type of GPS capable of accurately measuring the altitude of the vehicle. This would allow for a better estimate of the slope of the road, which in turn will improve the energy consumption of the vehicle. Another logical step towards this improvement would be to install an inclinometer in the vehicle, allowing a direct measure of the road slope. The second wise step is to add GSM internet connection to the system. The internet connection would allow access to state of the vehicle at all times of its motion. On the other hand, since this vehicle is mostly used for transporting tourists, it will be interesting to create an interactive **dashboard** oriented for tourists in the solar rickshaw that it can display key performance indicators in such a way it will keep the tourists well informed about the trips. Some indicators can include: General characteristics of the trip, such as the total distance traveled, amount of energy produced by the solar panels, extension of the range due to the solar panels, parameters that provide information related to the contribution of the mounting system to the economic return and the environment, such as the estimated cost reduction on the grid and CO_2 emissions, respectively.

Lastly, in the models implemented to estimate the energy consumption in vehicle trips, there are some ways of improving them. To extend the benefits of the proposed system for a whole year, it will be necessary to acquire much more data. In this dataset, the data collected from solar panels can be used to forecast the performance of the photovoltaic system to allow the driver to make the decision on what the range extension could be for the next trip day, for example. To improve the performance of the physical model implemented, it is possible to perform experimental tests on the vehicle in order to better estimate its parameters. It is also possible to improve the estimate of motor efficiency by performing tests in the vehicle instead of estimating the efficiency map using look-up tables. Apart from the physical models implemented, other models including neural networks can also be implemented.

Bibliography

[1] European Comission. Roadmap to a single europoean transport area - towards a competitive and resource efficient system. Technical report, 2011. URL https://transport.ec.europa.eu/index_en.

[2] United Nations. Adoption of the Paris Agreement. https://unfccc.int/resource/docs/2015/cop21/eng/l09r01.pdf, 2015. [Online; accessed 29-Jun-2022].

[3] M. Muratori, M. Alexander, D. Arent, M. Bazilian, P. Cazzola, E. M. Dede, J. Farrell, C. Gearhart, D. Greene, A. Jenn, M. Keyser, T. Lipman, S. Narumanchi, A. Pesaran, R. Sioshansi, E. Suomalainen, G. Tal, K. Walkowicz, and J. Ward. The rise of electric vehicles—2020 status and future expectations. *Progress in Energy*, 3(2):022002, mar 2021. doi: 10.1088/2516-1083/abe0ad. URL https://doi.org/10.1088/2516-1083/abe0ad.

[4] I. E. Agency. *Global EV Outlook 2021*, 2021.

[5] L. C. Orellana. *Carregador de Baterias Monofásico paraAplicação em Veículos Eléctricos - Programa de Pós-graduação em Engenharia Eléctrica*. PhD thesis, Centro de Tecnologia, Universidade Federal do Ceará, Fortaleza, 2011.

[6] Instituto da Mobilidade e Trasportes I.P. Homologação de Veículos . https://www.imt-ip.pt/sites/IMTT/Portugues/Veiculos/Aprovacoes/HomologacoesVeiculos/Paginas/HomologacaoVeiculos.aspx, 2019. [Online; accessed 23-May-2022].

[7] Fraunhofer. Net-zero-carbon Transport in Europe until 2050. https://www.isi.fraunhofer.de/content/dam/isi/dokumente/cce/2021/EU_Transport_policybrief_long.pdf, 2021. [Online; accessed 28-May-2022].

[8] Dr. Bryn Walton, Dr. Jamie Hamilton, G. Alberts, S. Fullerton-Smith, Edward Day, James Ringrow. Electric vehicles: Setting a course for 2030. Technical report, 2020. URL https://www2.deloitte.com/uk/en/insights/focus/future-of-mobility/electric-vehicle-trends-2030.html.

[9] Deloitte. 2018 Deloitte Global Automotive Consumer Study. pages 1–47, 2018.

[10] Hannah Ritchie, Max Roser and Pablo Rosado. Energy. *Our World in Data*, 2020. https://ourworldindata.org/energy.

[11] Our World In Data. Solar PV module prices. https://ourworldindata.org/grapher/solar-pv-prices?time=2010..2019, 2021. [Online; accessed 28-May-2022].

[12] M. Abdelhamid, S. Pilla, R. Singh, I. Haque, and Z. Filipi. A comprehensive optimized model for on-board solar photovoltaic system for plug-in electric vehicles: energy and economic impacts: On-board solar photovoltaic system for plug-in electric vehicles. *International Journal of Energy Research*, 40, 09 2016. doi: 10.1002/er.3534.

[13] C. Thiel, A. Gracia Amillo, A. Tansini, A. Tsakalidis, G. Fontaras, E. Dunlop, N. Taylor, A. Jäger-Waldau, K. Araki, K. Nishioka, Y. Ota, and M. Yamaguchi. Impact of climatic conditions on prospects for integrated photovoltaics in electric vehicles. *Renewable and Sustainable Energy Reviews*, 158: 112109, 2022. ISSN 1364-0321. doi: https://doi.org/10.1016/j.rser.2022.112109. URL https://www.sciencedirect.com/science/article/pii/S1364032122000387.

[14] Helianto project. Instituto Superior Tecnico, TU Lisbon. http://helianto.ist.utl.pt/. [Online; accessed 29-Ago-2022].

[15] K. Das. Bi Facial Solar Photovoltaic Panel Based E Rickshaw with Prismatic Lithium Ferro Phosphate Baterry . ttps://ec.europa.eu/transport/sites/default/files/themes/strategies/doc/2011_white_paper, 2021. Accessed: 2021-05-29.

[16] M. Rahman, G. D'Este, and J. Bunker. Non-motorized public transport development : present scenario and future approach in developing cities. 10 2009.

[17] M. Sameeullah and S. Chandel. Design and analysis of solar electric rickshaw: A green transport model. In *2016 International Conference on Energy Efficient Technologies for Sustainability (ICEETS)*, pages 206–211, 2016. doi: 10.1109/ICEETS.2016.7582927.

[18] M. Ines. Análise daintegridade estrutural datransmissão de potênciade um tuk tuk. Master's thesis, Instituto Superior Tecnico, 2020.

[19] Local Tuk Tuk. O que é um Tuk Tuk? https://localtuktuk.com/pt-pt/o-que-e-um-tuk-tuk/, 2017. Accessed:2021-05-01.

[20] Maximize Market Research. Global E-Rickshaw Market: Industry Analysis and forecast 2020 – 2027: By Product Type, Application and Region. https://www.alliedmarketresearch.com/press-release/three-wheeler-market.html, 2019. Accessed: 2022-06-26.

[21] C. Cochrane, T. Muneer, and B. Fraser. Design of an electrically powered rickshaw, for use in india. *Energies*, 12(17), 2019. ISSN 1996-1073. doi: 10.3390/en12173346. URL https://www.mdpi.com/1996-1073/12/17/3346.

[22] Fortune Business Insights. Electric three wheeler Marker Size, Share Covid-19 impact Analysis, By Battery type (Lithium-ion and Lead Acid), By Power type (Up to 1000 W, 1000 W to 1500 W, and above 1500 W), By End Use Type (Passenger Carrier and Good

Carrier), and Regional Forecasts, 2021-2028. https://www.fortunebusinessinsights.com/electric-three-wheeler-market-105028, 2020. Accessed: 2022-06-28.

[23] A. Mahmoudzadeh Andwari, A. Pesiridis, S. Rajoo, R. Martinez-Botas, and V. Esfahanian. A review of battery electric vehicle technology and readiness levels. *Renewable and Sustainable Energy Reviews*, 78:414–430, 2017. ISSN 1364-0321. doi: https://doi.org/10.1016/j.rser.2017.03.138. URL https://www.sciencedirect.com/science/article/pii/S1364032117306251.

[24] T. Selten. Stella lux: The energy-positive family car. *Europhysics News*, 48:13–16, 05 2017. doi: 10.1051/epn/2017301.

[25] Lightyear. Always charging in the sun. Longest range. Most sustainable. The electric car that charges itself with sunlight. https://lightyear.one/company. [Online; accessed 28-May-2022].

[26] Sono Motors. Sion electric car. https://sonomotors.com/en/sion/, 2020. [Online; accessed 28-May-2022].

[27] K. S. Reddy, S. Aravindhan, and T. K. Mallick. Techno-economic investigation of solar powered electric auto-rickshaw for a sustainable transport system. *Energies*, 10(6), 2017. ISSN 1996-1073. doi: 10.3390/en10060754. URL https://www.mdpi.com/1996-1073/10/6/754.

[28] D. Neto. Trip and history-based range prediction for a light powered vehicle based on real-world data. Master's thesis, Instituto Superior Tecnico, 2020.

[29] A. S. C. Chaiyamanon and N. Noomwongs. Dynamic modeling of electric tuk-tuk for predicting energy consumption in bangkok driving condition. *SAE Technical Papers*, 2013. ISSN 26883627. doi: 10.4271/2013-01-0113.

[30] L. Guzella and A. Sciarretta. *Vehicle Propulsion Systems: Introduction to Modeling and Optimization*. Springer Berlin Heidelberg New York, 3 edition, 2013. ISBN 9783540251958.

[31] J. A. Duffie and W. A. Beckman. *Solar Engineering of Thermal Processes*. John Willey Sons, new york edition, 1991.

[32] S. Kalogirou. *Solar energy engineering: processes and systems*. 1st edition edition, 2009.

[33] E. Lorenzo. *Energy Collected and Delivered by PV Modules*, chapter 20, pages 905–970. John Wiley Sons, Ltd, 2003. ISBN 9780470014004. doi: https://doi.org/10.1002/0470014008.ch20. URL https://onlinelibrary.wiley.com/doi/abs/10.1002/0470014008.ch20.

[34] A. H. S. R. A. v. S. M. Z. Klaus Jäger, Olindo Isabella. *Solar Energy: Fundamentals, Technology, and Systems*. 2014.

[35] F. Kasten and A. T. Young. Revised optical air mass tables and approximation formula. *Applied optics*, 28 22:4735–8, 1989.

[36] G. M. Tina. *Submerged and Floating Photovoltaic systems*. Academic Press, 2018.

[37] R. Perez, P. Ineichen, R. Seals, J. Michalsky, and R. Stewart. Modeling daylight availability and irradiance components from direct and global irradiance. *Solar Energy*, 44:271–289, 1990. doi.org/10.1016/0038-092X(90)90055-H.

[38] Energy Education. Photovoltaic effect. https://energyeducation.ca/encyclopedia/Photovoltaic_effect, 2022. [Online; accessed 10-Jun-2022].

[39] andré NOTH. *Design of Solar Powered Airplanes for Continuous Flight*. PhD thesis, Ecole Polytechnique Fédérale de Lausanne, Suisse, October 2008.

[40] M. Alonso García and J. Balenzategui. Estimation of photovoltaic module yearly temperature and performance based on nominal operation cell temperature calculations. *Renewable Energy*, 29 (12):1997–2010, 2004. URL https://EconPapers.repec.org/RePEc:eee:renene:v:29:y:2004:i:12:p:1997-2010.

[41] João Tavares Pinho, Marco Antonio Goldino. Manual de Engenharia para Sistemas Fotovoltaicos. https://www.portal-energia.com/downloads/livro-manual-de-engenharia-sistemas-fotovoltaicos-2014.pdf, 2014. [Online; accessed 10-Jun-2022].

[42] M. A. A. Mamun, M. Hasanuzzaman, and J. Selvaraj. Experimental investigation of the effect of partial shading on photovoltaic performance. *IET Renewable Power Generation*, 11(7): 912–921, 2017. doi: https://doi.org/10.1049/iet-rpg.2016.0902. URL https://ietresearch.onlinelibrary.wiley.com/doi/abs/10.1049/iet-rpg.2016.0902.

[43] V. Sun, A. Asanakham, and T. T Deethayat. Increase of power generation from solar cell module by controlling its module temperature with phase change material. *Journal of Mechanical Science and Technology*, 34:2609–2618, 2020. doi.org/10.1007/s12206-020-0336-8.

[44] A. G. Vaskov, N. Y. Mozder, and A. F. Narynbaev. Modelling of solar-diesel hybrid power plant. *IOP Conference Series: Materials Science and Engineering*, 1211(1):012011, jan 2022. doi: 10.1088/1757-899x/1211/1/012011. URL https://doi.org/10.1088/1757-899x/1211/1/012011.

[45] Tinytag Talk 2. Cost-effective temperature data logger with probe. https://www.geminidataloggers.com/data-loggers/tinytag-talk-2/tk-4023, .

[46] Tinytag Talk 2. Cost-effective indoor temperature data logger with built-in sensor. https://www.geminidataloggers.com/data-loggers/tinytag-talk-2/tk-4014, .

[47] SolarGIS. Solar resource maps of Portugal). https://solargis.com/maps-and-gis-data/download/portugal. Online; accessed: 2022-05-16.

[48] European Comission. PVGIS Photovoltaic Geographical Information System. https://re.jrc.ec.europa.eu/pvg_tools/en/, 2005. [Online; accessed 10-Jun-2022].

[49] Tuk Tuk Factory. ABOUT. https://etukfactory.com/. Online; accessed: 2022-06-15.

[50] GWL. CALB 180AH LiFePO4 Battery Datasheet. https://shop.gwl.eu/index.php?cur=1{&}cl=details{_}disc{&}anid=2946{#}tab3, . Online; accessed: 2022-03-11.

[51] E-Tuk Factory. e-Tuk Limo GT Brochure. https://www.etukfactory.com/limo, 2020. [Online; accessed 17-December-2021].

[52] Energy Education. Different Types of Solar Panels. https://www.treehugger.com/flexible-solar-panels-5206311#citation-2, 2021.

[53] T. L. Scott and A. Eleyan. Coap based iot data transfer from a raspberry pi to cloud. In *2019 International Symposium on Networks, Computers and Communications (ISNCC)*, pages 1–6, 2019. doi: 10.1109/ISNCC.2019.8909150.

[54] Eric S. Raymond. GPSD Client HOWTO. https://gpsd.gitlab.io/gpsd/client-howto.html. Online; accessed: 2022-05-18.

[55] Hostinger Tutorials. Como Usar SFTP (SSH File Transfer Protocol). https://www.hostinger.com.br/tutoriais/como-usar-sftp-ssh-file-transfer-protocol. Online; accessed: 2022-05-16.

[56] OpenTopography. Shuttle radar topography mission (srtm) global. https://portal.opentopography.org/datasetMetadata?otCollectionID=OT.042013.4326.1, 2013. Online; accessed 10 March 2022.

[57] Mapbox. Access elevation data. https://docs.mapbox.com/data/tilesets/guides/access-elevation-data/.

[58] Z. Yi and P. H. Bauer. Adaptive multiresolution energy consumption prediction for electric vehicles. *IEEE Transactions on Vehicular Technology*, 66(11):10515–10525, 2017. doi: 10.1109/TVT.2017.2720587.

[59] PV insitights. Grid the World. http://pvinsights.com/index.php/, 2017. Accessed: 2022-05-27.

[60] Trading Economics. Portugal Inflation Rate. https://tradingeconomics.com/portugal/inflation-cpi, 2022. [Online; accessed 5-Jun-2022].

[61] Y Charts. Portugal Long Term Interest Rate. https://ycharts.com/indicators/portugal_long_term_interest_rates, 2022. [Online; accessed 5-Jun-2022].

[62] Global Petrol Prices. Portugal preços da electricidade. https://pt.globalpetrolprices.com/Portugal/electricity_prices/, 2022. [Online; accessed 5-Jun-2022].

[63] C. G. B. Ventura. Techno-economic analysis of charging posts to be installed in a hub for electric vehicles. Master's thesis, Instituto Superior Tecnico, 2019.

[64] GWL. CALB 135AH LiFePO4 Battery Datasheet. https://shop.gwl.eu/LiFePO4-cells-3-2-V/ELERIX-Lithium-Cell-LiFePO4-Prismatic-3-2V-135Ah.html#tab2, . Online; accessed: 2022-06-14.

[65] M. H. Mobarak, R. N. Kleiman, and J. Bauman. Solar-charged electric vehicles: A comprehensive analysis of grid, driver, and environmental benefits. *IEEE Transactions on Transportation Electrification*, 7(2):579–603, 2021. doi: 10.1109/TTE.2020.2996363.

Appendix A

Notes about the Data Acquisition System

A.1 Data Table

Each data files contains variables that characterize the trajectory, the solar power production and the battery pack for a constant sampling frequency. The variables collected from the three different sensors can be seen in table A.1.

GPS Data	Solar Power Data	Battery pack information
LAT - latitude	VOLTAGE_PV - PV voltage (V)	V_TOT - Total voltage
LON - longitude	CURRENT_PV - PV current (A)	V_CELL_01 - Cell nr 01 voltage
TIME - time	POWER_PV - PV power (W)	(...)
ALT - altitude values (m)	ENERGY_PV - PV energy (Wh)	V_CELL_24 - Cell nr 24 voltage
EPV		I_TOT - Total current of the battery pack
EPT		SOC_% - Percentage of remaining capacity
SPEED - vehicle speed in m/s		SOC_(AH) - SOC in AH
climb -		(AH) - Cycle capacity of battery pack
		T1 - MOS temperature
		T2 - Temperature sensor 2
		T3 - Temperature sensor 3
		T4 - Temperature sensor 4
		T5 - Temperature sensor 5
		T6 - Temperature sensor 6
		POWER - Instantaneous power consumption
		N_CELL_MAX - Number of the cell with the maximum voltage
		V_CELL_MAX - Voltage of the cell with the maximum voltage
		N_CELL_MIN - Number of the cell with the minimum voltage
		V_VELL_MIN - Voltage of the cell with the minimum voltage
		V_VELL_AVG - Average voltage of the cells
		N_CELLS - Total number of the cells in the pack

Table A.1: Table containing several features collected from the three different sensors during data collection.

A.1.1 BMS - Data Format

Table A.2: Conversion unit between the apk and the data acquisition built.

Label App	Label algorithm	Unit/Conversion	Description
Volt	V_TOT	$V/10^1$	Total voltage of the battery pack
[01]	V_CELL_01		Cell nr 1 Voltage
[02]	V_CELL_02		Cell nr 02 Voltage
[03]	V_CELL_03		Cell nr 03 Voltage
[04]	V_CELL_04		Cell nr 04 Voltage
[05]	V_CELL_05		Cell nr 05 Voltage
[06]	V_CELL_06		Cell nr 06 Voltage
[07]	V_CELL_07		Cell nr 07 Voltage
[08]	V_CELL_08		Cell nr 08 Voltage
[09]	V_CELL_09		Cell nr 09 Voltage
[10]	V_CELL_10		Cell nr 10 Voltage
[11]	V_CELL_11	$V/10^3$	Cell nr 11 Voltage
[12]	V_CELL_12		Cell nr 12 Voltage
[13]	V_CELL_13		Cell nr 13 Voltage
[14]	V_CELL_14		Cell nr 14 Voltage
[15]	V_CELL_15		Cell nr 15 Voltage
[16]	V_CELL_16		Cell nr 16 Voltage
[17]	V_CELL_17		Cell nr 17 Voltage
[18]	V_CELL_18		Cell nr 18 Voltage
[19]	V_CELL_19		Cell nr 19 Voltage
[20]	V_CELL_20		Cell nr 20 Voltage
[21]	V_CELL_21		Cell nr 21 Voltage
[22]	V_CELL_22		Cell nr 22 Voltage
[23]	V_CELL_23		Cell nr 23 Voltage
[24]	V_CELL_24		Cell nr 24 Voltage
Current	I_TOT	$A/10^1$	Total current of the battery pack
SOC	SOC_%	%	Percentage of remaining capacity
Capacity	SOC(AH)	$AH/10^6$	Remaining capacity of battery pack (in AH)
CycleAH	(AH)	$AH/10^3$	Cycle capacity of battery pack
MOS	T1		MOS Temperature
Balanced	T2		Temperature sensor 2
T1	T3	$°C/-$	Temperature sensor 3
T2	T4		Temperature sensor 4
T3	T5		Temperature sensor 5
T4	T6		Temperature sensor 6
Power	POWER	W/-	Instantaneous Power Consumption
-	N_CELL_MAX		Number of the cell with the maximum voltage
CellHigh	V_CELL_MAX	$V/10^3$	Voltage values of the cell with the maximum voltage
-	N_CELL_MIN		Number of the cell with the minimum voltage
CellLow	V_CELL_MIN	$V/10^3$	Voltage values of the cell with the minimum voltage
CellAvg	V_CELL_AVG	$V/10^3$	Average Voltage of the cells
-	N_CELLS	-	Total number of the cells in the pack

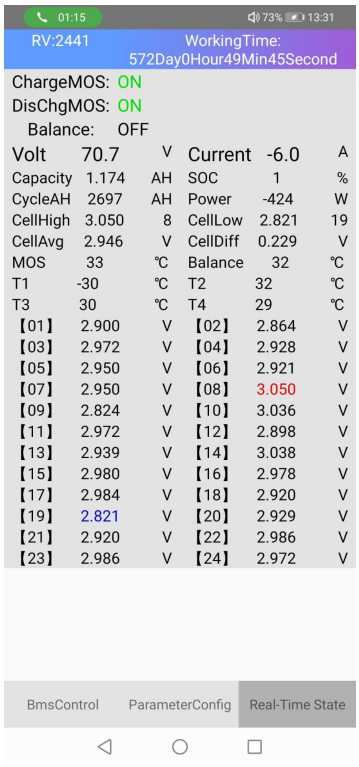

Figure A.1: Screen-shot of the Mobile application measurements.

Appendix B

PV Panel Specification

Sunmodule™

SW 220 poly / Version 2.0 and 2.5 Frame

World-class quality
Fully-automated production lines and seamless monitoring of the process and material ensure the quality that the company sets as its benchmark for its sites worldwide.

SolarWorld Plus-Sorting
Plus-Sorting guarantees highest system efficiency. SolarWorld only delivers modules that have greater than or equal to the nameplate rated power.

25 years linear performance guarantee and extension of product warranty to 10 years
SolarWorld guarantees a maximum performance degression of 0.7% p.a. in the course of 25 years, a significant added value compared to the two-phase warranties common in the industry. In addition, SolarWorld is offering a product warranty, which has been extended to 10 years.*

*in accordance with the applicable SolarWorld Limited Warranty at purchase.
www.solarworld.com/warranty

· Qualified, IEC 61215
· Safety tested, IEC 61730
· Periodic Inspection

1)

ISO 9001
ISO 14001
Certified

Intertek

c UL us LISTED
1058
Photovoltaic Module / Panel

Made in USA

SOLARWORLD

We turn sunlight into power.

www.solarworld.com

Sunmodule™

SW 220 poly / Version 2.0 and 2.5 Frame

PERFORMANCE UNDER STANDARD TEST CONDITIONS (STC)*

		SW 220
Maximum power	P_{max}	220 Wp
Open circuit voltage	V_{oc}	36.6 V
Maximum power point voltage	V_{mpp}	29.2 V
Short circuit current	I_{sc}	8.08 A
Maximum power point current	I_{mpp}	7.54 A

*STC: 1000W/m², 25°C, AM 1.5

THERMAL CHARACTERISTICS

NOCT	46 °C
TC I_{sc}	0.081 %/K
TC V_{oc}	-0.37 %/K
TC P_{mpp}	-0.45 %/K
Operating temperature	-40°C to 85°C

IV-curves for SolarWorld Sunmodule Plus SW 220 poly at 25°C cell temperature

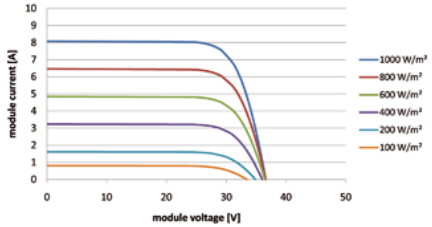

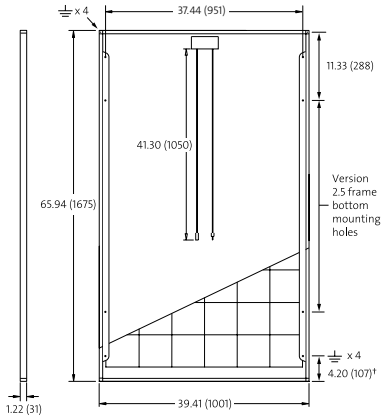

PERFORMANCE AT 800 W/m², NOCT, AM 1.5

		SW 220
Maximum power	P_{max}	157.3 Wp
Open circuit voltage	V_{oc}	33.1 V
Maximum power point voltage	V_{mpp}	26.2 V
Short circuit current	I_{sc}	6.68 A
Maximum power point current	I_{mpp}	6.01 A

Minor reduction in efficiency under partial load conditions at 25°C: at 200W/m², 95% (+/-3%) of the STC efficiency (1000 W/m²) is achieved.

COMPONENT MATERIALS

Cells per module	60
Cell type	Poly crystalline
Cell dimensions	6.14 in x 6.14 in (156 mm x 156 mm)
Front	tempered glass (EN 12150)
Frame	Clear anodized aluminum
Weight	46.7 lbs (21.2 kg)

SYSTEM INTEGRATION PARAMETERS

Maximum system voltage SC II	1000 V
Max. system voltage USA NEC	600 V
Maximum reverse current	16 A
Number of bypass diodes	3
UL Maximum Test Load**	45 psf (2.1 kN/m²)
IEC Maximum Snow Test Load**	113 psf (5.4kN/m²)

**Please apply the appropriate factors of safety according to the test standard and local building code requirements when designing a PV system.

ADDITIONAL DATA

Power tolerance2)	-0 Wp / +5 Wp
J-Box	IP65
Connector	MC4
Module efficiency	13.12 %
Fire rating (UL 790)	Class C

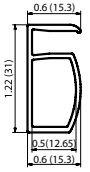

VERSION 2.0 FRAME
- Compatible with "Top-Down" mounting methods
- ⏚ Grounding Locations: 4 corners of the frame

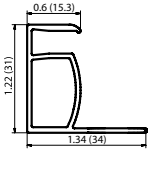

VERSION 2.5 FRAME
- Compatible with both "Top-Down" and "Bottom" mounting methods
- ⏚ Grounding Locations:
  - 4 corners of the frame
  - 4 locations along the length of the module in the extended flange†

1) Sunmodules dedicated for the United States and Canada are tested to UL 1703 Standard and listed by a third party laboratory. The laboratory may vary by product and region. Check with your SolarWorld representative to confirm which laboratory has a listing for the product.
2) Measuring tolerance traceable to TUV Rheinland: +/- 2% (TUV Power Controlled).
3) All units provided are imperial. SI units provided in parentheses.

SolarWorld AG reserves the right to make specification changes without notice.

B.1 PV Panel Datasheept Specification

PZEM-003/017 DC communication module

Overview

This document describes the specification of the PZEM-003/017 DC communication module, the module is mainly used for measuring DC voltage, current, active power, frequency and energy consumption, the module is without display function, the data is read through the RS485 interface.

PZEM-003: Measuring Range 10A (Built-in Shunt)

PZEM-017: Measuring Range 50A、100A、200A、300A (the current range is depend on the external shunt specification)

1. Function description

1.1 **Voltage**

1.1.1 Measuring range:0.05-300V. (when the test voltage is ＜7V, please use the independent power supply mode)

1.1.2 Resolution:0.01V.

1.1.3 Measurement accuracy:1%.

1.2 **Current**

1.2.1 Measuring range:0.01-10A(PZEM-003);0.02-300A(PZEM-017;can be matched with 50、100、200、300A four kinds of shunt).

1.2.2 Resolution:0.01A

1.2.3 Measurement accuracy:1%

1.3 **Power**

1.3.1 Measuring range:0.1-3kW(PZEM-003);0.2-90kW(PZEM-017)

1.3.2 Resolution: 0.1W

1.3.3 Measurement accuracy:1%

1.4 **Energy Consumption**

1.4.1 Measuring range: 0-9999kWh

1.4.2 Resolution: 1Wh

1.4.3 Measurement accuracy:1%

1.4.4 Reset energy: use software to reset.

1.5 **Over Voltage alarm**

Voltage threshold can be set, divide into high voltage and low voltage threshold, when the measured voltage exceeds the threshold, it can alarm

The default high voltage threshold is 300V, the default low voltage threshold is 7V.

1.6 **Communication interface**

RS485 interface.

2. Communication protocol

2.1 **Physical layer protocol**

Physical layer use UART to RS485 communication interface.

Baud rate is 9600, 8 data bits, 2 stop bit, no parity.

2.2 **Application layer protocol**

The application layer use the Modbus-RTU protocol to communicate. At present, it only supports function codes such as 0x03 (Read Holding Register), 0x04 (Read Input Register), 0x06 (Write Single Register), 0x41 (Calibration), 0x42 (Reset energy).etc.

0x41 function code is only for internal use (address can be only 0xF8), used for factory calibration and return to factory maintenance occasions, after the function code to increase 16-bit password, the default password is 0x3721.

The address range of the slave is 0x01 ~ 0xF7. The address 0x00 is used as the broadcast address, the slave does not need to reply the master. The address 0xF8 is used as the general address, this address can be only used in single-slave environment and can be used for calibration etc.operation.

2.3 **Read the measurement result**

The command format of the master reads the measurement result is(total of 8 bytes):

Slave Address + 0x04 + Register Address High Byte + Register Address Low Byte + Number of Registers High Byte + Number of Registers Low Byte + CRC Check High Byte + CRC Check Low Byte.

The command format of the reply from the slave is divided into two kinds:

Correct Reply: Slave Address + 0x04 + Number of Bytes + Register 1 Data High Byte + Register 1 Data Low Byte + ... + CRC Check High Byte + CRC Check Low Byte

Error Reply: Slave address + 0x84 + Abnormal code + CRC check high byte + CRC check low byte

Abnormal code analyzed as following (the same below)

- 0x01,Illegal function;
- 0x02,Illegal address;
- 0x03,Illegal data;
- 0x04,Slave error.

The register of the measurement results is arranged as the following table

Register address	Description	Resolution
0x0000	Voltage value	1LSB correspond to 0.01V
0x0001	Current value	1LSB correspond to 0.01A
0x0002	Power value low 16 bits	1LSB correspond to 0.1W
0x0003	Power value high 16 bits	
0x0004	Energy value low 16 bits	1LSB correspond to 1Wh
0x0005	Energy value high 16 bits	
0x0006	High voltage alarm status	0xFFFF is alarm, 0x0000 is not alarm
0x0007	Low voltage alarm status	0xFFFF is alarm, 0x0000 is not alarm

For example, the master sends the following command (CRC check code is replaced by 0xHH and 0xLL, the same below):

0x01 + 0x04 + 0x00 + 0x00 + 0x00 + 0x08 + 0xHH + 0xLL

Indicates that the master needs to read 8 registers with slave address 0x01 and the start address of the register is 0x0000.

The correct reply from the slave is as following:

0x01 + 0x04 + 0x10 + 0x27 + 0x10 + 0x00 + 0x64 + 0x03 + 0xE8 + 0x00 + 0x00 + 0x00 + 0x00 + 0x00 + 0x00 + 0x00 + 0x00 + 0x00 + 0x00 + 0x00 + 0xHH + 0xLL

The above data shows

- Voltage is 0x2710，converted to decimal is 10000,display 100.00V；
- Current is 0x0064，converted to decimal is 100,display 1.00A；
- Power is 0x000003E8，converted to decimal is 1000,display 100.0W；
- Energy is 0x00000000，converted to decimal is 0,display 0Wh；
- High voltage alarm status 0x0000,indicates the current voltage is lower than the high voltage threshold.
- Low voltage alarm status 0x0000,indicates the current voltage is higher than the low voltage threshold.

2.4 **Read and modify the slave parameters**

At present,it only supports reading and modifying slave address and power alarm threshold

The register is arranged as the following table

Register address	Description	Resolution
0x0000	High voltage alarm threshold(5~350V), default is 300V	1LSB correspond to 0.01V
0x0001	Low voltage alarm threshold （1~350V）, default is 7V	1LSB correspond to 0.01V
0x0002	Modbus-RTU address	The range is 0x0001~0x00F7
0x0003	The current range(only for PZEM-017)	0x0000：100A 0x0001：50A 0x0002：200A 0x0003：300A

The command format of the master to read the slave parameters and read the measurement results are same(described in details in Section 2.3), only need to change the function code from 0x04 to 0x03.

The command format of the master to modify the slave parameters is (total of 8 bytes):

Slave Address + 0x06 + Register Address High Byte + Register Address Low Byte + Register Value High Byte + Register Value Low Byte + CRC Check High Byte + CRC Check Low Byte.

The command format of the reply from the slave is divided into two kinds:

Correct Response: Slave Address + 0x06 + Number of Bytes + Register Address Low Byte + Register Value High Byte + Register Value Low Byte + CRC Check High Byte + CRC Check Low Byte.

Error Reply: Slave address + 0x86 + Abnormal code + CRC check high byte + CRC check low byte.

For example, the master sets the slave's high voltage alarm threshold:

0x01 + 0x06 + 0x00 + 0x00 + 0x4E + 0x20 + 0xHH + 0xLL

Indicates that the master needs to set the 0x0000 register (high voltage alarm threshold) to 0x4E20（200.00V）.

Set up correctly, the slave return to the data which is sent from the master.

For example, the master sets the low voltage alarm threshold of the slave

0x01 + 0x06 + 0x00 + 0x01 + 0x03 + 0xE8 + 0xHH + 0xLL

Indicates that the master needs to set the 0x0001 register (low voltage alarm threshold) to 0x03E8(10.00V).

Set up correctly, the slave return to the data which is sent from the master.

For example, the master sets the address of the slave

0x01 + 0x06 + 0x00 + 0x02 + 0x00 + 0x05 + 0xHH + 0xLL

Indicates that the master needs to set the 0x0002 register (Modbus-RTU address) to 0x0005

Set up correctly, the slave return to the data which is sent from the master.

2.5 **Reset energy**

The command format of the master to reset the slave's energy is (total 4 bytes):

Slave address + 0x42 + CRC check high byte + CRC check low byte.

Correct reply: slave address + 0x42 + CRC check high byte + CRC check low byte.

Error Reply: Slave address + 0xC2 + Abnormal code + CRC check high byte + CRC check low byte

2.6 **Calibration**

The command format of the master to calibrate the slave is (total 6 bytes):

0xF8 + 0x41 + 0x37 + 0x21 + CRC check high byte + CRC check low byte.

Correct reply: 0xF8 + 0x41 + 0x37 + 0x21 + CRC check high byte + CRC check low byte.

Error Reply: 0xF8 + 0xC1 + Abnormal code + CRC check high byte + CRC check low byte.

It should be noted that the calibration takes 3 to 4 seconds, after the master sends the command, if the calibration is successful, it will take 3 ~ 4 seconds to receive the response from the slave.

2.7 **CRC check**

CRC check use 16bits format, occupy two bytes, the generator polynomial is X16 + X15 + X2 +1, the polynomial value used for calculation is 0xA001.

The value of the CRC check is all results of a frame data checking divide CRC

3. Functional block diagram

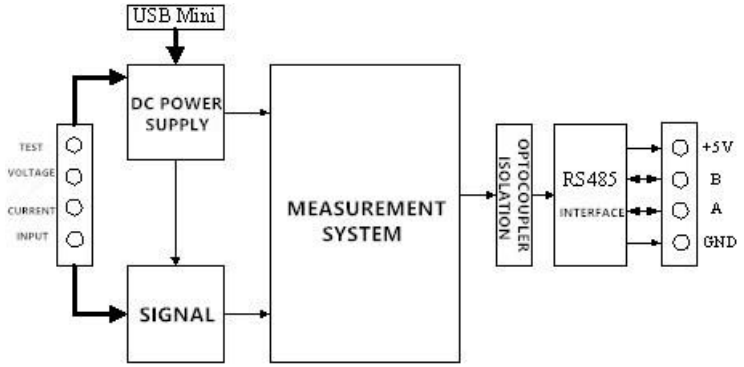

Picture 3 Functional block diagram

4. Wiring diagram

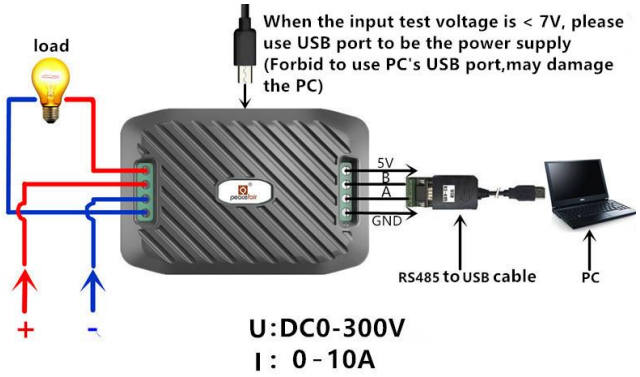

Picture 4.1 PZEM-003Wiring diagram

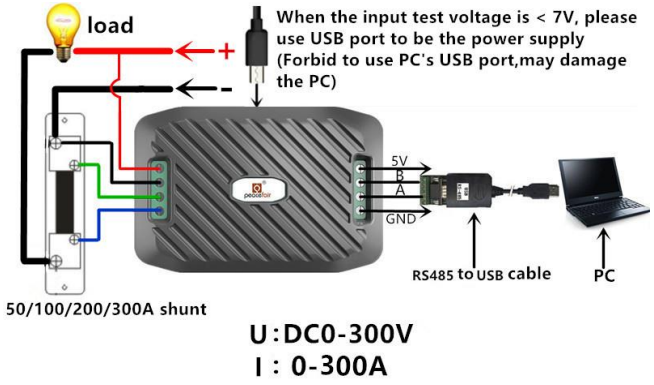

Picture 4.2 PZEM-017 Wiring diagram

5. Other instructions

5.1 RS485 interface is passive output, need external connect 5V power supply and the the external power supply should ＞100mA.

5.2 When the input test voltage is less than 7V, it must supply 5V independent work voltage through MICRO USB port;

Note: Do not use the USB port bring by your PC to be the independent power supply, otherwise it may damage your PC !

5.3 **Working temperature**

-20’C ~ +60’C。